High Power Superluminescent Light-Emitting Diodes

Rory Cahill
BSc
112311256

NATIONAL UNIVERSITY OF IRELAND, CORK

SCHOOL OF SCIENCE

DEPARTMENT OF PHYSICS

Thesis submitted for the degree of Doctor of Philosophy

March 2021

Head of Department: Professor John McInerney

Supervisors: Pleun Maaskant
Brian Corbett

Contents

List of Figures

List of Tables

List of Symbols

A.....	Shockley-Read-Hall coefficient
A_0.....	Vector potential
a.....	Linear gain coefficient
B.....	Bimolecular recombination coefficient
C.....	Auger recombination coefficient
c.....	Speed of light in a vacuum
D_{mod}.....	Modulation depth
d.....	Active region thickness
E_C.....	Conduction band energy
E_V.....	Valence band energy
E_g.....	Bandgap energy
f_c.....	Fermi function for electrons in conduction band
f_v.....	Fermi function for electrons in valence band
G.....	Rate of carrier generation by absorption
G_s.....	Single pass gain
g.....	Material gain
g_{mod}.....	Modal gain
H_{eh}.....	Hamiltonian for electrons and holes in a semiconductor
$\hbar$.....	Reduced Planck constant
I.....	Current
J.....	Current density
k.....	Boltzmann constant
L.....	Device length
L_C.....	Coherence length
L_T.....	Transfer length
l.....	Mode number
M.....	Number of possible modes
M_T.....	Transfer matrix
m.....	Effective mass
N.....	Carrier density
N_{tr}.....	Transparency carrier density
n.....	Electron density
n_{eff}.....	Effective refractive index
P.....	Power
P_{ideal}.....	Optical power output from an ideal SLED
P_{out}.....	Optical power output from a SLED

P_{sp}.....	Optical power from spontaneous emission
p.....	Hole density
q.....	Electron charge
R.....	Carrier recombination rate
R_{Aug}.....	Auger recombination rate
R_{nonrad}.....	Non radiative recombination rate
R_{sh}.....	Sheet resistance
R_{spon}.....	Spontaneous emission rate
R_{SRH}.....	Shockley-Read-Hall recombination rate
R_{stim}.....	Stimulated emission rate
R_F.....	Front facet reflectivity
R_B.....	Back facet reflectivity
S.....	Photon density
s.....	C-TLM gap spacing
T.....	Temperature
t.....	Time
V_a.....	Active region volume
V_{mode}.....	Volume of optical mode
W_{Abs}.....	Upward transition rate for carriers
W_{asl}.....	Wetting parameter
W_{Em}.....	Downward transition rate for carriers
w.....	Ridge width
z.....	Position
α.....	Total loss
α_i.....	Internal loss
α_m.....	Mirror loss
β.....	Spontaneous emission coupled to waveguide
η_i.....	Internal quantum efficiency
η_p.....	Power conversion efficiency
Γ.....	Optical confinement factor
γ.....	Surface tension
λ.....	Wavelength
μ.....	Spatial coherence
ν.....	Frequency
ρ.....	Density of states
ρ_C.....	Contact resistivity
σ_{ij}.....	Interfacial surface energy between i and j

τ.....	Carrier lifetime
τ_S.....	Photon lifetime

List of Acronyms

AR.....	Anti-reflection
ASE.....	Amplified Spontaneous Emission
CRI.....	Colour Rendering Index
EBL.....	Electron Blocking Layer
EQE.....	External Quantum Efficiency
FOG.....	Fibre-Optic Gyroscope
FP.....	Fabry-Perot
HVPE.....	Hydride Vapour Phase Epitaxy
ICP.....	Inductively Coupled Plasma
IQE.....	Internal Quantum Efficiency
LED.....	Light-Emitting Diode
LiDAR.....	Light Detection and Ranging
MOVPE.....	Metal Organic Vapour Phase Epitaxy
OCT.....	Optical Coherence Tomography
QCSE.....	Quantum Confined Stark Effect
QD.....	Quantum Dot
QW.....	Quantum Well
RGB.....	Red-Green-Blue
SLED.....	Superluminescent LED
SOA.....	Semiconductor Optical Amplifier
SRH.....	Shockley-Read-Hall
SSL.....	Solid State Lighting

List of Publications

First Author Publications

R. Cahill, P.P Maaskant, M.A Ahkter, B. Corbett, "High power surface emitting InGaN superluminescent light-emitting diodes", Applied Physics Letters, 115, 171102 (2019).

Conference Talks

R. Cahill, P.P Maaskant, M.A Ahkter, B. Corbett, "High power blue surface emitting InGaN superluminescent LEDs", presented at the International Conference on Nitride Semiconductors, Bellevue WA, U.S.A, session A05, 7th-12th July 2019.

R. Cahill, J.S.D Morales, B. Corbett, "High power surface emitting superluminescent LEDs", presented at the European Semiconductor Laser Workshop , Cork, Ireland, session 6, 27th-29th September 2019.

Conference Posters

R. Cahill, P.P Maaskant, M.A Ahkter, B. Corbett, "High power blue surface emitting InGaN superluminescent LEDs", presented at the Photonics Ireland, Galway, Ireland, 13th-15th September 2017.

R. Cahill, B. Corbett, "High power blue surface emitting superluminescent LEDs", presented at the International Symposium on the Science and Technology of Lighting, Sheffield, United Kingdom, 17th-22nd June 2018.

Other publications

J.S.D Morales, **R. Cahill**, B. Corbett, "High power horizontal cavity surface-emitting InGaN superluminescent diode" 2019 IEEE High Power Diode Lasers and Systems Conference, 49-50.

I, Rory Cahill, certify that this thesis is my own work and I have not obtained a degree in this university or elsewhere on the basis of the work submitted in this thesis.

Rory Cahill

Abstract

Superluminescent light-emitting diodes (SLEDs) are optoelectronic devices which combine different aspects of laser diode and LED performance. The device utilises a ridge waveguide structure to amplify spontaneously emitted light. Steps are taken to suppress feedback by minimising facet reflectivity. The result is a high-power, directional light source with a broad, smooth emission spectrum.

The combination of high-power, high spatial coherence and low temporal coherence initially saw SLEDs used in specialist applications such as sources for fibre-optic gyroscopes, optical coherence tomography and optical memory readout. The emergence of GaN based SLEDs in recent years has seen SLEDs mooted as potential sources for a range of emerging applications such as LiDAR, high resolution OCT and machine vision as well as for everyday applications like displays and car headlamps.

This work focusses on the development of GaN based surface emitting SLEDs. The devices use an integrated turning mirror at either end of the ridge waveguide to divert light downward through the transparent substrate. The turning mirror in combination with an antireflection coating applied to the back side of the chip are effective in suppressing the formation of Fabry-Perot modes in the device. This allows for high optical powers to be attained without sacrificing spectral quality. The device provides 2.2 W of optical peak power under pulsed operation, a record for a SLED device. At this maximum output power, the emission spectrum has a FWHM of 6 nm. The far field characteristic indicates a divergence of 7°x15° from a single output.

A model is presented which assists in the optimisation of SLEDs. Simulated L-I curves and spectra allow for the behaviour of devices to be predicted prior to fabrication. This enables the user to estimate the optimum device characteristics such as length, epitaxial structure, and facet reflectivity without going through the costly and time-consuming process of device fabrication.

The optimisation of several key process steps are described. The development of an ohmic Pd p-contact allowed for the demonstration of simultaneously driven SLED arrays. An inductively coupled plasma etch was developed to provide smooth, angled sidewalls for the integrated GaN turning mirror.

Further work should be done to develop a suitable package for the device to dissipate the heat generated and allow for higher duty cycles and CW operation. The integration of optics such as micro-lenses or colour converting phosphors onto the back of the chip should also be investigated.

Acknowledgements

First and foremost I would like to thank my supervisors, Brian Corbett and Pleun Maaskant. Brian, thank you for giving me the opportunity to study and work in the III-V device group for the last few years. I have immensely enjoyed working with you and learned so much, both technically and personally from the experience. Your patience, guidance and encouragement allowed me to work at things that interested me, while always keeping my PhD on track. I am very grateful for all the support you have provided throughout my PhD.

To Pleun, thank you for helping me through the early stages of my time at Tyndall. Your advice and kindness made it a fantastic place to work and to learn. I'm sure you are enjoying a well earned retirement.

Many thanks also to my monitor Prof. Stefan Andersson-Engels and my advisor Dr. Bryan Kelleher for the useful advice and feedback along the way.

To Laura, my best friend, thank you for always being there for me. Thank you for putting up with me when I was cranky or stressed and for always cheering me up. You bring so much fun and joy into my life. I can't wait to start our next chapter!

To my family, thank you for the constant love and support. Mam, you have always given me every chance to be the best person I can be. The happy home you made gave us the best possible start in life. I will always be grateful for everything you have done for us. Lara, thanks for always always caring, listening and making me laugh. Tom, thank you for the advice along the way and the craic both at home and in Thomond Park! James and Jack, the fun you guys provide around the house was always a welcome relief in stressful times. Thank you all for helping me deal with whatever problems came my way.

To my team mates and colleagues who have helped me so much over the course of my PhD. Mahbub, Juan, John, Brendan, James, Carlos, Tanmay, Zhi, Zeinab, Jack, Yan, Muhammet, Tommy, Pietro, Karim, Krimo, and Farzan - you have all helped me at some point along the way. Without you I could not have completed my PhD. I am very grateful to have been part of such a strong team full of friendly, interesting people.

To the lads, Darragh, Eoin, Michael, thanks for the craic, the games of pool, the relentless slagging and for being unbelievable mates. There's a booth in Costigan's waiting for us when this pandemic is over!

Finally I would like to thank Enterprise Ireland and the European Structural and Investment Funds 2014–2020 program for funding this research.

Chapter 1

Introduction

The increasing complexity of applications for which photonic devices are used requires a variety of different light sources. While laser diodes and light-emitting diodes (LEDs) are now ubiquitous, some specialist applications require a light source which can combine the high-power and directionality of a laser diode with the broad emission spectrum of an LED. Superluminescent LEDs (SLEDs), can meet these requirements. The goal of this chapter is to introduce the SLED device and to explain the motivation behind its development.

SLEDs are devices with a structure similar to that of a laser diode. A ridge waveguide is used to guide and amplify light. Steps are taken to prevent reflections at the facets ensuring that light is only amplified in a single pass along the waveguide. This amplified spontaneous emission (ASE) process provides a smooth emission spectrum free from the oscillations caused by the formation of Fabry-Perot (FP) modes. Figure 1.1 shows a schematic of LED, SLED and laser diode spectra on the same wavelength scale.

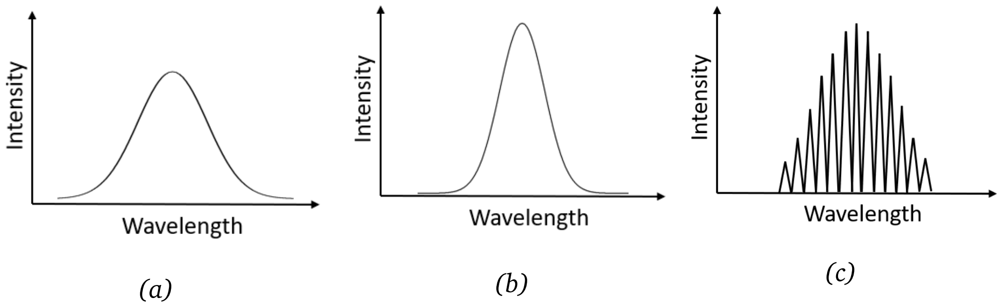

Figure 1.1: Example spectra of (a) an LED, (b) a SLED and (c) a laser diode on the same wavelength scale. The SLED exhibits a broad, smooth emission spectrum.

The first SLEDs developed emitted in the infra-red part of the spectrum in the 800 - 1500 nm range. The small emitting area and high directionality provided by SLEDs allows for efficient coupling of light into fibre-based systems. This along with the low temporal coherence provided by a broadband light source makes them optimal sources for fibre-optic gyroscopes (FOGs) where the low coherence reduces the amount of interference providing more accurate detection of the rotation speed. This reduction of noise in the signal due to reduced interference also made the SLED a useful light source for optical memory readout and the evaluation of waveguides for silicon photonics applications. The low levels of interference also made SLEDs suitable for assessing optical fibres. Optical coherence tomography (OCT) is another application in which SLEDs are widely used as light sources as their broadband emission spectrum allows for high axial resolution. The hybrid nature of SLEDs makes them a potential solution to numerous other applications such as LiDAR, encoders and machine vision. The introduction of GaN SLEDs brought the devices into the blue spectral range, bringing the possibility of SLEDs as sources for displays, higher resolution OCT and solid state lighting (SSL). This potential has led to increasing interest in SLED research with a significant rise in the number of papers published on the topic in recent years. This is illustrated in Figure 1.2 which shows that the number of SLED based papers has more than doubled since the turn of the century.

This introductory chapter discusses the history of the SLED since its introduction in the 1970s. The evolution of SLED fabrication techniques and the specialist applications for which they have been used over the past few decades are discussed. The development of GaN as an efficient material for the electrical generation of light is also discussed. The recent developments of SLEDs in the GaN material system are analysed and parasitic lasing is

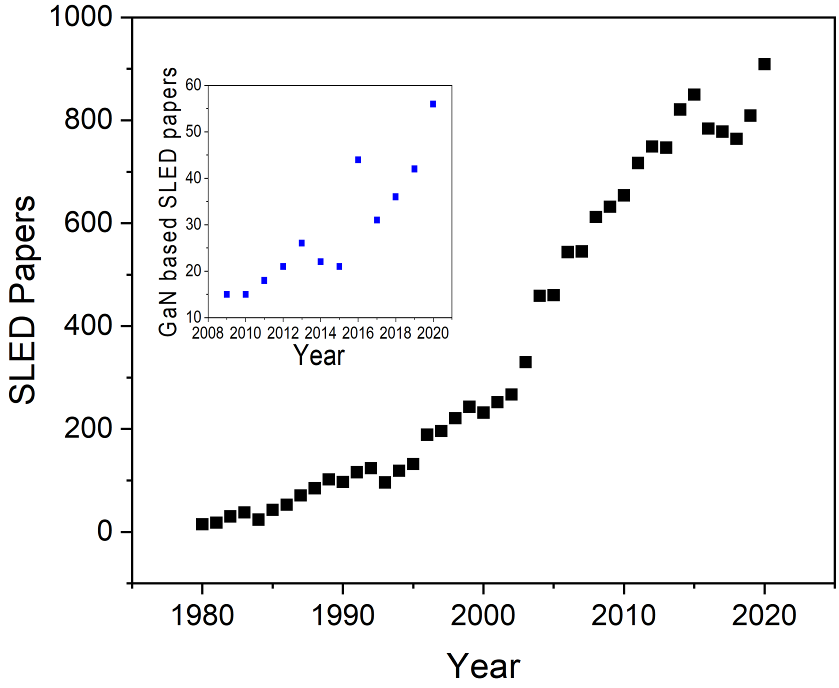

Figure 1.2: The number of papers published per year on the topic of SLEDs has increased in recent years. This data was obtained using a Google Scholar search for the keywords "superluminescent LED" "SLED" and "superluminescent diode". Data for GaN SLED papers used the same terms, also including "GaN", "InGaN" and "Gallium Nitride".

identified as the main limitation on the optical power which can be obtained from a SLED.

While all GaN SLEDs reported to date have been edge emitting devices, this thesis focusses on GaN based surface emitting SLEDs. These substrate emitting devices demonstrate a novel method of extracting high levels of light without the onset of parasitic lasing. The following chapters present theoretical and experimental work explaining the effectiveness of this design, as well as the improvements that could be made in the future. At the end of the chapter the motivation and content of the remainder of the thesis are explained.

1.1 The History of Superluminescent Light-Emitting Diodes

1.1.1 Early Advances in the Arsenide Material System

The first superluminescent light-emitting diodes were demonstrated by Pei et al. in 1973 [1]. The devices were introduced in the arsenide material system, emitting in the red. The objective at the time was to fabricate a device with low temporal coherence which could be efficiently coupled into an optical fibre. The initial motivation for a this type of light source was to avoid the formation of high energy density nodes due to Fabry-Perot (FP) mode formation in laser diode cavities. These nodes could result in a high build up of energy at the facet resulting in catastrophic optical damage, greatly reducing the lifetime of laser diodes.

Lasing was suppressed in the first SLEDs by using an absorbing region at one end of the waveguide. The resultant device could provide optical peak power up to 80 mW under pulsed operation with a pulse width of 200 ns and a repetition rate of 2 kHz. The spectral FWHM was 8 nm with a low divergence allowing for 80% coupling efficiency to a multimode optical fibre with a NA of 0.63. The device itself however was quite inefficient with external quantum efficiency (EQE) of 3.4%.

Several variations on the same geometry were used to fabricate SLEDs over the course of the next decade, with absorbing regions and antireflection coatings the preferred method of suppressing FP modes in the waveguide. Typically, the devices reported in this era could provide tens of milliwatts of power in CW operation with FP modulation depths between 10% and 25% [2]. The devices reported are exclusively in the AlGaAs material system.

A significant advancement in SLED technology occurred in the late 1980s when the innovation of a tilted waveguide geometry was reported by Alphonse et al [3]. By choosing a suitable angle (5°) at which to tilt the waveguide with respect to the facet, the facet reflectivity could be reduced by a factor of 10, while maintaining a directional, low divergence beam. These tilted waveguide devices could provide 15 mW of optical power in CW mode while maintaining a smooth emission spectrum with a FWHM of 8 nm. Efficiency was also greatly increased as an absorbing region was not required to control feedback in these devices. This meant that energy was not wasted generating photons when would go on to be absorbed in the waveguide.

Further investigations into SLED technology included extending the wavelength range further into the infrared. This was achieved using InAlGaAs/InP heterostructures [4, 5]. Power of up to 5 mW were reported for devices with a peak emission wavelength at 1.5 μm in 1990 by Noguchi et al [6]. Later in the 1990s SLEDs were introduced for the AlInP material system emitting at 670 nm. These devices were aimed at the DVD reader market.
In 1993 Lin and Tang reported ultrashort pulse generation from a SLED by using an integrated optical absorber [7]. Pulses as short as 190 fs were realised, increasing the SLED's credentials as a potential source for optical communications, machine vision and light detection and ranging applications.
Further research on GaAs SLEDs in the 1990s focussed on increasing spectral quality and spectral broadness. The bent waveguide structure was introduced in 1996 [8]. This structure had one end normal to the cleaved facet with the other bending to make a 7° angle with the facet. This bent waveguide SLED provided 6 mW of optical power with low spectral ripple of 10%. In 1997 an AlGaAs SLED with a spectral width of 91.5 nm was fabricated using a structure with four quantum wells (QWs) each of a different thickness.

Increased optical power was also of interest to researchers. Yamatoya et al. reported optical powers of greater than 1 W under pulsed operation in a InAlGaAsP SLED in 1999 [9]. The device used a tilted, tapered waveguide for the gain section and maintained a broad 60 nm spectrum at high power. Song et al then reported 20 mW of optical power in CW operation using a single mode tilted waveguide [10]. The high power was achieved by optimising the device mounting; the device was mounted p-side down on a copper heat sink. This effective heat sinking delayed the saturation of the L-I curve from 400 mA of applied current to 800 mA. This shows the importance of effective packaging of superluminescent devices to optimise performance.

1.1.2 21st Century Advances in GaAs and InP Based SLEDs

More recent developments in GaAs and InP SLEDs include the introduction of quantum dot (QD) based SLEDs [11–13]. These were first suggested in a theoretical paper in 1999 by Sun et al. [14] as a potential solution to provide very broad spectra. The favourite application for these very broadband devices was optical coherence tomography [15] due to their efficient fibre coupling and very low temporal coherence. Some of the QD based devices could provide spectral widths greater than 130 nm [16] with wavelengths in the infrared between 1.2 μm and 1.5 μm. Research also continued into the use of SLEDs as sources for FOGs [17] and gas sensing [18]. Quantum dot based SLEDs have been introduced in the InAs material as a means of increasing the bandwidth of the device [19, 20]. The size and indium content variation of the dots allows for a much broader range of wavelengths to be generated by the SLED with bandwidths of up to 144 nm being realised using this method.
As GaAs SLED technology matured it became commercially available with companies such as Superlum, OSRAM and EXALOS offering fully packaged GaAs SLEDs in the late 2000s. In the past year, surface emitting SLEDs were demonstrated by Jentzsh et al [21], using a monolithically integrated mirror to reflect light downward through the substrate.

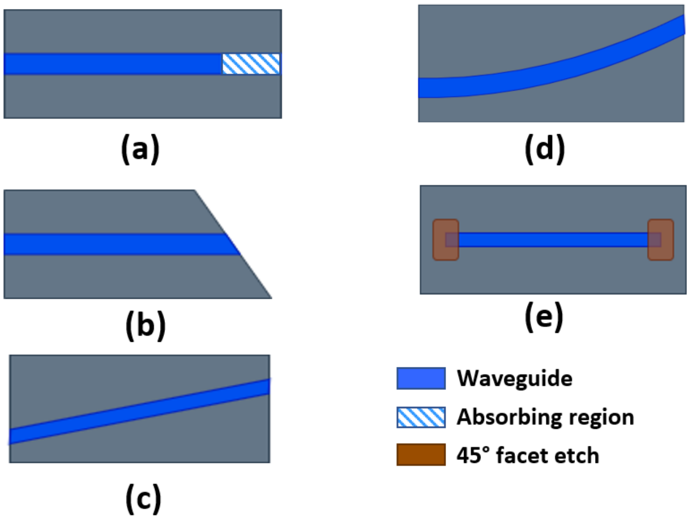

Figure 1.3: 2D schematics of different SLED structures: (a) passive absorbing region, (b) tilted facet, (c) tilted waveguide, (d) bent waveguide, (e) surface emitting SLED with 45° turning mirror which is introduced in this thesis.

1.1.3 The Development of GaN Based SLEDs

The first single crystal GaN was reported in 1969 [22]. The material was grown using Hydride Vapour Phase Epitaxy (HVPE). The difficulty in growing large crystals with low defect density inhibited their use as efficient light emitters. The large number of defects was mainly due to the lack of a suitable substrate for the growth of GaN films. Most GaN was grown on sapphire substrates which suffered from a significant lattice mismatch. GaN films showed naturally good n-type conductivity. Early attempts to p-dope GaN resulted in semi-insulating layers.

The first light emission from GaN was observed in 1971 when a very high voltage (60V) was applied to a GaN m-i-n structure resulting in green luminescence at 515 nm [23]. The luminescent GaN featured a Zn-doped p-region. Not long after this, the first blue GaN based LEDs were reported using the same Zn-doping [24]. The luminescence of these devices was at 475 nm. The issue with these early GaN LEDs was the very high voltages required for light emission due to the relatively poor conductivity of the Zn-doped p-type layers.

The introduction of Mg p-doping in 1972 greatly improved the conductivity of the p-type layers. This was demonstrated by the fabrication of a blue LED operating at 10 V with the emission spectrum centred at 425 nm [25]. Few significant advances were made in the ensuing years until the growth of GaN films with an AlN buffer layer using molecular beam epitaxy (MBE) by Yoshida et al. in 1983 [26]. This was followed by Amano et al. using Metal Organic Vapor Phase Epitaxy (MOVPE) to grow GaN with an AlN buffer in the 1986 [27]. These methods provided the twin benefits of better quality crystals and a reduction of the carrier density in the unintentionally doped GaN layers. The p-type layer resistivity still restricted the efficiency of GaN devices and prevented entirely the possibility of fabricating a laser diode which would require large current density to induce stimulated emission. The breakthrough in the solving this issue was made by Nakamura in 1992 [28]. By thermally annealing Mg doped GaN, passivated Mg dopant atoms could be activated, providing a more conductive p-layer. Amano, Akasaki and Nakamura would be awarded the Nobel prize in 2014 for enabling the fabrication of efficient blue LEDs. The first high-brightness GaN based LEDs were reported in 1994. A double heterostructure was used to confine carriers with undoped InGaN QWs sandwiched between GaN barriers acting as the active region. Tuning the Indium content of the QWs allowed for the desired wavelength to be precisely chosen.

As high-quality material and conductive p-type contact layers were now available research began into fabrication of blue laser diodes based on GaN. The first GaN based laser diode was reported by Nakamura et al. in 1996, emitting at 417 nm [29]. These early devices required high currents to reach the lasing threshold and suffered from poor lifetimes due to relatively high defect density due to growth on non-native substrates.

In 2003 Sumitomo et al. introduced a new method for growing bulk GaN substrates [30]. These substrates were grown using inverse pyramidal pits to eliminate dislocations in the material. This method confined dislocations to stripes on the wafer with very low defect density regions in between. Other methods of lateral overgrowth have also been used to grow high quality GaN films in recent years [31]. This method also allowed for the growth of semi-polar and non-polar GaN [32], a potential solution to the wavelength shift and efficiency reduction in GaN based devices due to the quantum confined Stark effect (QCSE).

The combined developments of efficient p-type doping and high-quality bulk GaN films allowed for huge improvements in GaN based laser diode performance. Green laser diodes, semi-polar and non-polar laser diodes have become popular areas of research. Record low lasing thresholds of 10 mA and optical powers greater than 107 W have been reported [33]. Today GaN based laser diodes are widely available commercially and are used in applications

such as BluRay readers and laser-based projection systems. The maturation of the GaN laser diode led to investigation into more novel device structures such as the SLED. In 2009 the first GaN based SLED was reported by Feltin et al. [53]. The optical power from the device was 10 mW in CW operation. This result sparked increasing interest in blue SLEDs over the next few years.
Several different methods of preventing reflections in GaN waveguides were suggested in the early 2010s including KOH wet etching to roughen the front facet [35], bent waveguides, tilted waveguides and anti-reflection coatings. Schematics of these different types of SLED are shown in Figure 1.3. These early SLEDs typically offered tens of milliwatts of optical power with spectral widths of 6-10 nm. The first high-power SLEDs (>100mW optical power) were reported in 2011 by Ohno et al. [36]. By using a tilted, exponentially tapered waveguide to reduce reflectivity and optical density at the front facet, 200 mW of optical power was achieved . The spectral width of the device was relatively narrow at 3 nm with visible modulations in the spectrum. This work showed that much higher powers could be obtained from blue SLEDs if the feedback could be sufficiently controlled.
Some of the key issues with early GaN based SLEDs were highlighted by Kafar et al. in 2012 [37]. They studied SLEDs of different lengths using different methods of reducing facet reflectivity and found the most important factor in increasing the optical power from a SLED was the length of the device. Increasing the length also had negative impacts such as narrowing the emission spectrum and increasing the spectral modulation depth. The factor which limited the output power of the SLEDs was not gain saturation or device failure at high power as might have been expected. The biggest obstacle to very high-power SLEDs was the tendency of the devices to lase at high current densities. Reinforcing the key finding of Ohno's paper; if the effects of parasitic lasing were minimised there was potential for the fabrication of SLEDs with much higher output powers.

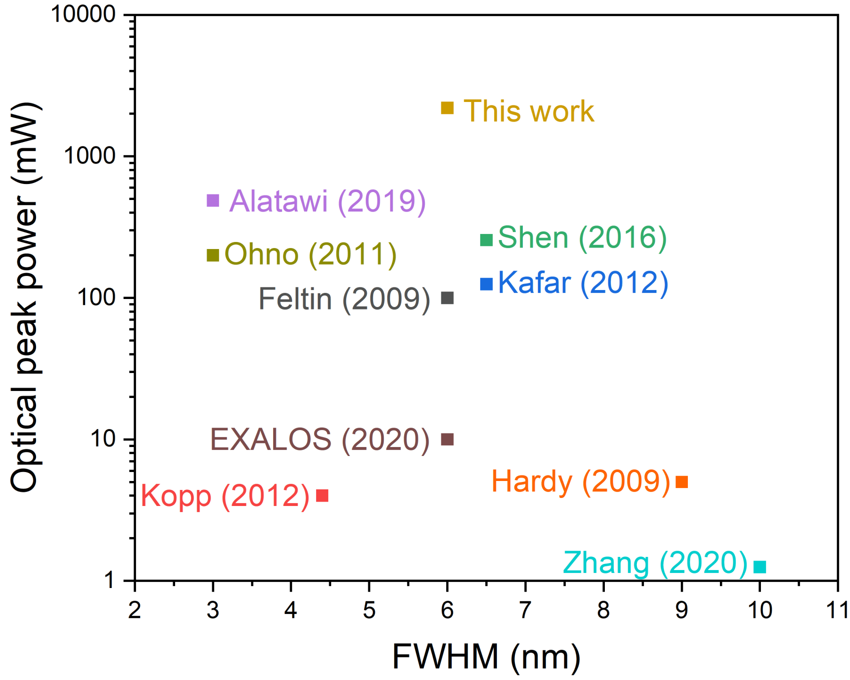

Figure 1.4: Optical peak power and FWHM of recently developed GaN based SLEDs.

Other important advances at this time included the extending of GaN SLED wavelengths into the Cyan/Green region by using QWs with high indium content in the active region [38]. The first high-power (powers >100 mW) SLEDs based on semi-polar GaN substrates [39] using an absorbing region at the back end of the device to reduce feedback.

At the beginning, one of the applications generating interest into GaN based SLED research was pico-projection [40, 41] . However, the potential for high modulation speeds and visible wavelength led to blue SLEDs being proposed as potential sources for smart solid-state lighting [42] and underwater visible light communications [43]. The characteristics of low temporal coherence and short wavelength has seen blue SLEDs mooted as a potential source for high-resolution optical coherence tomography [44]. Interest in the fundamental physics of the devices was also motivation for research. GaN based SLEDs were seen as a potential solution to the issue of thermal efficiency droop in nitride based emitters [45].

In recent years the optical power being reported in blue SLEDs has increased. By modifying commercial blue laser diodes Alatawi et al. reported a blue SLED capable of providing 487 mW of optical peak power under pulsed operation [46]. This device as used in tandem with colour converting

perovskite nanocrystals to create a directional white light source with a high colour rendering index (CRI) [47]. Once again, the limiting factor for these devices was parasitic lasing. Significant modulations are visible in the spectrum at high current. The interest in colour converting SLEDs to create a white light source is due to their potential as a source for Li-Fi [48]. The broad spectrum as well as high speed switching capabilities are suited to both room lighting and information transfer. As well as colour converters, RGB SLEDs were explored as sources for white light and displays [49].
Other recent developments have trended towards increasing the spectral bandwidth and include the fabrication of short cavity GaN based SLEDs [50]. That amplification can be achieved in these short cavity devices shows the high levels of optical gain in GaN structures which makes them ideal for SLED fabrication. Goldberg et al. also demonstrated enhanced spectral bandwidth using a three-section device [51] with bias applied to an absorbing rear section in order to control the spectral broadness. Table 1.1 shows the current state of the art for GaN based SLEDs. Analysis of the state of the art of GaN SLED devices suggests that parasitic lasing and high transparency current density are the principle obstacles to efficient, high-power operation.

1.2 GaN Surface Emitting SLEDs

This thesis introduces GaN based surface emitting SLEDs [52]. This device used a monolithically integrated turning mirror at either end of the waveguide to divert light downward through the transparent GaN substrate. A 3-D schematic of the device is shown in Figure 1.5. The two emitting facets and effectiveness of the turning mirrors in suppressing FP modes allowed for very high optical powers while maintaining a broad, smooth emission spectrum. 2.2 W of optical peak power was recorded from a single device at 1.5 A under pulsed operation with a 1% duty cycle. At this maximum power the FWHM of the spectrum was 6 nm. This result showed how important the minimisation of facet reflectivity is in the design of a SLED as very high efficiency and optical powers can be realised without lasing action if mode formation is prevented. This thesis will focus on the design development and characterisation of these devices. The result of this work is the device which has produced the highest optical peak power from a SLED to date as shown in Figure 1.4.
The epitaxial laser structure consists of two InGaN QWs with AlGaN cladding layers to confine the light in the waveguide. A narrow ridge is used to

generate the high carrier density required to reach transparency.

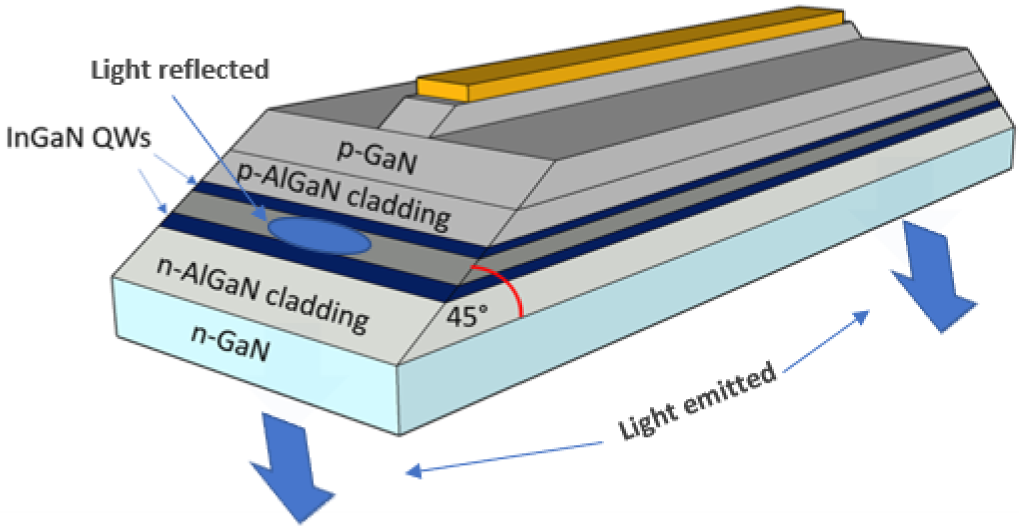

Figure 1.5: 3-D schematic of surface emitting SLED based on GaN.

One of the advantages of the surface emitting approach is that the amplified light is reflected out of the plane of the waveguide. This makes it more difficult for feedback to occur and for FP modes to form. The design also means that both facets emit in the same direction, effectively doubling the amount of light which can be collected from the device. As the light is emitted normal to the substrate, there is potential for the integration of additional technology such as micro lenses or colour converting materials onto the back side of the chip. The motivation of this thesis was to develop and increase understanding SLED devices.The optimisation of these surface emitting SLEDs presents the opportunity to create a reliable high-power, broad spectrum light source which is much improved on the current state of the art. The thesis aims to address the areas of the device design and fabrication process which can be controlled to optimise the device.

Table 1.1: Current state of the art for superluminescent light-emitting diodes.

Year	Group	Design	Optical Power (mW)	λ_{Peak} (FWHM) (nm)
2009	Feltin et al [53]	Tilted facet	100	420 (6)
2011	Ohno et al [36]	Tapered stripe	200	405 (3)
2012	Kopp et al [38]	Bent waveguide	4	500 (4.4)
2012	Kafar et al [37]	Bent waveguide	125	405(6.5)
2016	Shen et al [39]	Passive absorber	256	447 (6.5)
2019	Jentzsh et al [54]	Surface emitting	250	950 (3)
2019	Alatawi et al [55]	Tilted facet	487	457 (3)
2019	Cahill et al [52]	Surface emitting	2200	416 (6)
2020	Zhang et al [50]	AR coating	1.25	427 (7.5)
2020	EXALOS [56]	Tilted facet	6	510 (10)

1.3 Thesis outline

- **Chapter 2 - The fundamentals of SLED Operation**
  This chapter discusses the fundamental physics which is relevant to the operation of a SLED. Concepts such as carrier and photon confinement, carrier recombination, gain and mode formation are covered. This chapter points out the key points of difference between SLEDs, LDs and LEDs. The important factors which must be considered when designing the geometry and epitaxial structure of a SLED are highlighted.

- **Chapter 3 - Design and optimisation of SLEDs**
  A model for simulation the L-I and spectral characteristics of SLEDs is presented. Special attention is given to the non-uniform distribution of carrier and photon density across the waveguide. Numerical simulations are used to find the steady state conditions of longitudinal carrier density distribution, photon density distribution and optical gain in a SLED ridge. The results are analysed and suggestions made on how to best optimise the geometry and epitaxial structure for GaN based SLEDs.

- **Chapter 4 - Process optimisation**
  The process of SLED fabrication is outlined and the most important steps highlighted. The optimisation of these key process steps is then described later in the chapter. The optimisation of the p-contact is described. A low resistivity p-contact is critical to minimise the level of Joule heating at the metal-semiconductor interface and maximise the device lifetime. A wafer preparation process and thermal annealing are shown to greatly improve the contact resistivity of Pd on p-GaN. The development of an etch for the sloped turning mirror facet is described. The resist reflow

process was modelled in 3-D using the Surface Evolver soap film model to optimise mask design. An inductively coupled plasma etch was developed for the smooth etching of angled sidewalls. The optimisation of the bondpads for best heat management is also discussed in this chapter.

- **Chapter 5 - Device characterisation**
  The key characteristics of the SLED device are measured and analysed. The Light-Current-Voltage characteristics, spectra, near field and far field measurements are presented. A record optical peak power for a SLED is measured under pulsed operation. The impact of an anti-reflection coating on the emission spectrum is also examined. Results are compared with the theoretical model presented in Chapter 3. The characterisation of surface-emitting SLED arrays is also presented for the first time.

- **Chapter 6 - Conclusions and future work**
  The most important results of the thesis are summarised and recommendations for further development and understanding of SLEDs are made.

- **Appendix**
  The appendix includes the MatLab code which was used for the simulations discussed in Chapter 3.

Chapter 2

The fundamentals of SLED Operation

2.1 Introduction

This chapter explains the mechanisms by which superluminescent LEDs work as well as the different factors which can impact their performance. The beginning of the chapter explains the structure of a GaN SLED. Section 2.2 discusses how the epitaxial layer structure is used to confine excited carriers and how generated photons are confined using a ridge waveguide. Special attention is given to the challenges associated with working with the InAlGaN material system.
The injection of carriers into the device is then discussed. This section explains how the excited carrier population is affected by applied current and bias. The concept of gain is introduced. This section explains that population inversion must be achieved in order to amplify light in a semiconductor. The different carrier recombination mechanisms in a GaN SLED are discussed in section 2.5. This section outlines how carrier can be expected to recombine at different levels of injection and how this would affect the performance of a SLED.
Potential issues which could negatively affect the device performance are examined at the end of the chapter. Thermal management of the devices is one of the main issues in this area. The impact of facet reflectivity and optical coatings is also examined. Finally spatial and temporal coherence are discussed as the combination of high spatial coherence with low temporal coherence is what separates a SLED from both a laser diode and an LED.

2.2 Device structure

A SLED is a form of diode. P-doped and n-doped materials are put into physical contact with one another. This leads to the diffusion of free carriers into the material of opposite conductivity, leaving behind ionised donor and acceptor atoms. The result is an electric field between the two materials at the junction which prevents further carrier diffusion between the materials and a 'depletion region' free of charge carriers is formed. Diffusion and drift processes eventually lead to equilibrium in the system and the formation of a constant Fermi level throughout the system. The asymmetric distribution of carriers also results in a bending of the valence band and conduction band with a potential difference V_{bi} between the bands in the p-type material and n-type material. When a bias is applied in the forward direction the bands are flattened and there is a net movement of charge through the material. When an electron and hole come into contact with one another they can recombine, resulting in the emission of a photon.
To maximise the probability of radiative recombination, a heterostructure is used. Very narrow regions in the order of nanometers called quantum wells (QWs) form the active region. The bandgap is lower in the active region than in the surrounding p-type and n-type layers. High concentrations of carriers are then confined to the QWs creating a high spatial overlap of electrons and holes which recombine radiatively.
The band structure of a GaN based laser diode with two InGaN QWs in forward bias is shown in Figure 2.1 (a). The QWs are where the bandgap is lowest. Increasing the indium content in the QWs would lower the bandgap further. This is where the majority of carriers will be confined when a bias is applied. Next to the QWs is the wide bandgap AlGaN electron blocking layer (EBL). This layer provides a potential barrier which stops electrons from escaping the active region without recombining. A similar layer is not required to prevent holes from escaping as they have a higher effective mass and lower mobility than electrons. This band diagram was generated using the SiLENSe laser simulation package [57]. Figure 2.1 (b) shows a typical AlGaAs QW laser diode band structure.

The band diagrams illustrate one of the challenges of using GaN in laser diode and SLED fabrication. The inbuilt piezoelectric field in the InGaN QWs results in a shifting of the allowed electron states to lower energies and the hole states to higher energies. This causes a redshift of the emission wavelength as the

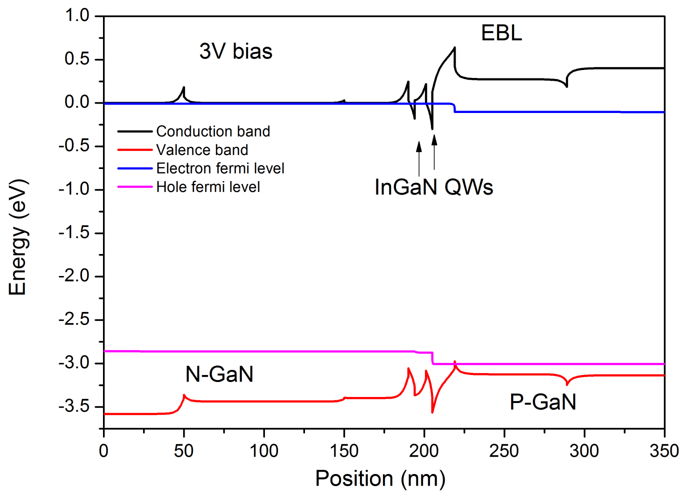

(a)

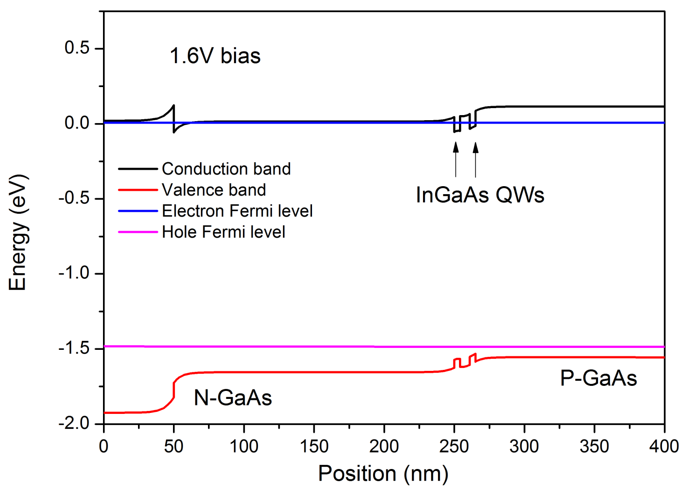

(b)

Figure 2.1: Band diagrams of (a) GaN (b) GaAs laser structures with applied bias above the bandgap.

bandgap energy is reduced. The electrons and holes are also pushed to opposite sides of the well, reducing the overlap integral and thereby decreasing the rate of radiative recombination. The result of lower overlap can be a reduction of internal quantum efficiency (IQE) by a factor of 2 [58]. This effect is known as the quantum confined Stark effect (QCSE).
At high current, the high number of carriers in the QWs can screen the QWs from the piezoelectric field. This results in the band flattening and the spatial overlap of electrons and holes increasing. This also results in a blueshift of the emission spectrum as the electrons are shifted back to higher energies while the holes are shifted down to lower energies in the absence of the QCSE. This effect is illustrated in Figure 2.2 where the band diagram at different bias voltages is presented. At higher bias, a flatter band structure with a larger energy gap E_g is seen in the QWs. The QCSE increases the threshold of laser and SLED devices with InGaN QWs due to the reduced overlap integral at low current. Once this is overcome however, high powers can be achieved at high current where the carriers are screened from the effects of the QCSE.
The QCSE does not affect GaAs or InP based devices to the same extent as GaN based devices. This allowed for a greater spatial overlap of electrons and holes at low current. This allows for a greater rate of radiative recombination and a lower lasing threshold.

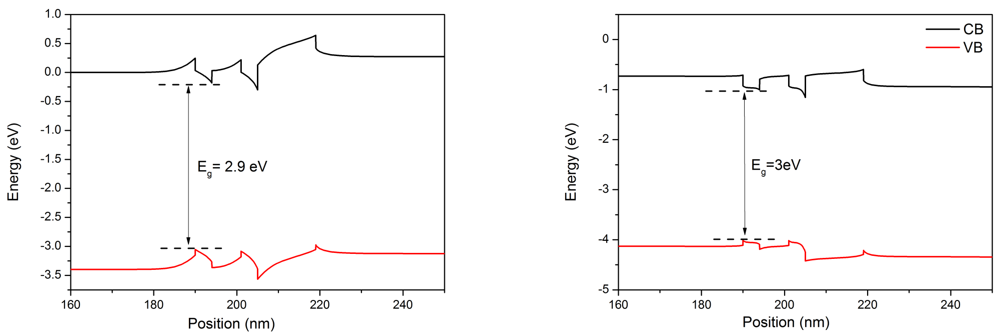

(a) (b)

Figure 2.2: Band diagram of InGaN QWs where the carrier density in the QWs is (a) $3 \times 10^{19} cm^{-3}$ and (b) $6 \times 10^{19} cm^{-3}$. Carrier screening of the electric field reduces the QCSE.

Confinement of the emitted photons in the transverse direction is achieved by using cladding layers in the stack. These layers are positioned either side of the active region. The active region has a higher refractive index than the cladding layers and so a portion emitted photons are confined by total internal reflection. Figure 2.3 shows a the transverse refractive index profile typical GaN laser stack. The size of the optical mode is clearly much larger than the size of the QWs. The level of overlap between mode and QWs defines the magnitude of the optical confinement factor Γ. Increasing the thickness of the QWs or using a greater number of wells can help to increase the level of confinement.

The refractive index of the free-standing GaN substrate is higher than the refractive index of the cladding layers. This creates the risk of the mode coupling into the high index substrate. This creates a second intensity lobe in the far field making it more difficult to focus the light to a small spot. The n-AlGaN layer must be thick enough to prevent this coupling of the mode into the substrate.

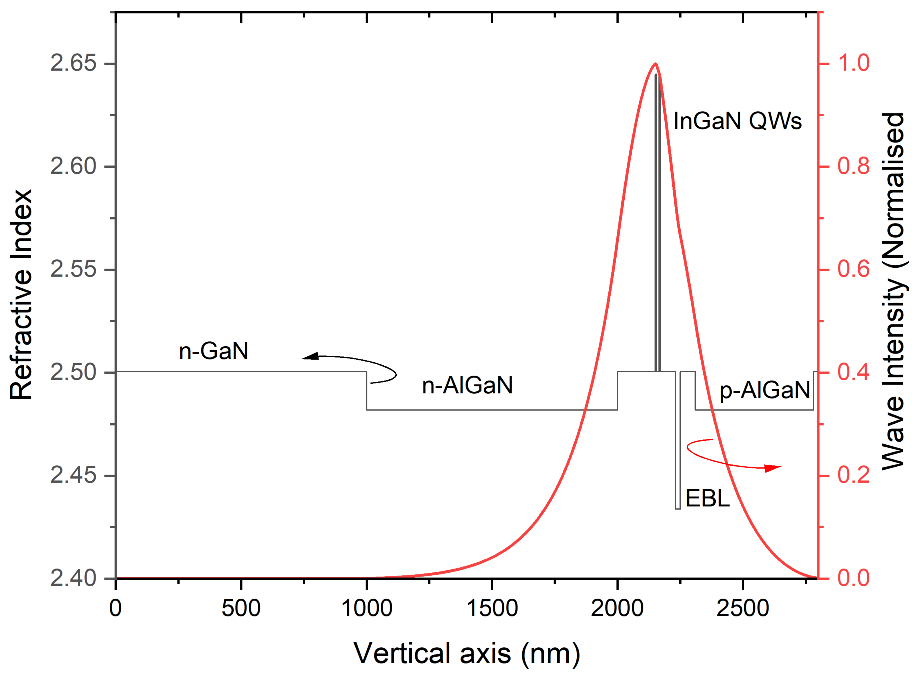

Figure 2.3: Refractive index profile of a GaN laser stack. The cladding layers with refractive index much lower than the active QW region confine light in the transverse direction. The optical mode is shown in red.

To confine photons in the lateral direction a ridge waveguide structure is used as shown in Figure 1.5. A narrow ridge with a metal contact on top is etched into the top layers of the semiconductor. An insulating material such as SiO_2 is deposited around the ridge. This prevents the metal from coming into contact with the sidewalls of the ridge waveguide, potentially shorting the device or

increasing the waveguide loss. The current is only injected through the narrow ridge. This means that recombination and population inversion occur only in the region underneath the narrow stripe. This region will be the only part of the chip which has optical gain, meaning all of the amplification of light takes place under the stripe and not at the sides. This is known as gain guiding. When the level of carrier injection is low, the SLED will behave as an LED, spontaneously emitting incoherent radiation in all directions. If a sufficiently high concentration of carriers is reached and population inversion is achieved then those spontaneously emitted photons which are coupled into the waveguide will go on to induce further recombination events as they travel along the waveguide. The results is an exponential increase in the number of photons travelling in the waveguide. The device is now behaving as an optical amplifier or SLED. The increasing carrier density with current provides higher levels of gain and spontaneous recombination. This allows for increasing optical power from the SLED.
The device structure in the longitudinal direction consists of the long ridge waveguide with a facet at either end. Optical feedback and the formation of FP modes is prevented by taking steps to reduce the reflectivity at the facets. There are several different techniques which can be used to achieve this which are discussed in Chapter 1. Figure 1.3 illustrates some of these methods. Preventing the formation of modes reduces the level of spectral narrowing in SLEDs. This is discussed in detail in section 2.8.

2.3 Carrier injection

In optoelectronic devices such as SLEDs the principle source of excited charge carriers is the electrical current applied to the device. The application of a bias either by applying a voltage or as a result of applying a current changes the electron and hole populations so that they cannot be described by a single Fermi level. Instead, separate quasi-Fermi energies for electrons (E_C) and holes (E_V) are used to describe populations close to the conduction and valence bands. These quasi-Fermi levels are separated approximately by the magnitude of the applied bias. The ground and excited states of the system are written as E_1 and E_2. The population in both bands follows the Fermi-Dirac distribution given in equations 1 and 2.

$$f_c = \frac{1}{1 + e^{(E_2 - E_C)/kT}} \tag{2.1}$$

$$f_v = \frac{1}{1 + e^{(E_1 - E_V)/kT}} \tag{2.2}$$

Where f_c describes the distribution of electrons in the conduction band and $1 - f_v$ describes the distribution of holes in the valence band.
As the current provides excited carriers, other processes in which electron-hole pairs annihilate each other remove carriers from the system. The overall carrier density in a device can be described using the continuity equation for electrons:

$$\frac{\partial N}{\partial t} = G - R + \frac{J}{qd} \tag{2.3}$$

Where N is the excited carrier density, t is time, G is the rate of photon generation not related to the applied current (e.g. electron hole pairs generated due to light absorption), R is the electron-hole recombination rate and J is the applied current density, q is the electron charge and d is the thickness of the active region. The principle of charge neutrality demands that the net charge in the semiconductor be equal to zero. The total carrier density in the QWs can be measured by measuring the injected electron density i.e. the current density.
The rate of recombination R can be split into several components;

$$R = R_{spon} + R_{stim} + R_{nonrad} \tag{2.4}$$

The spontaneous emission recombination rate (R_{spont}), the stimulated emission recombination rate R_{stim} and the non-radiative recombination rate (R_{nonrad}). The first two terms together provide the overall radiative recombination rate i.e. the rate at which excited carriers recombine to emit a photon. The latter term refers to cases where excited carriers recombine with the resultant energy being released in the form of a lattice vibration or phonon. Each of these terms is described in more detail in the coming sections.

2.4 Recombination mechanisms

2.4.1 Spontaneous Emission

Spontaneous emission occurs as a result of random fluctuations in field strength [59]. The strength of the fluctuation induces the recombination of an electron-hole pair resulting in the emission of a photon. These vacuum oscillations are random in direction and phase and similarly the emitted photons are random in phase and emitted uniformly in all directions. Because spontaneous emission is a two-particle interaction, the spontaneous emission rate is proportional to the square of the carrier density.

$$R_{spon} = Bnp \tag{2.5}$$

Where n is the electron density, p is the hole density and B is the bimolecular recombination coefficient. It is assumed that the electron and hole populations are approximately equal so the square of the carrier density N^2 is used. The B factor is dependent on the electron-hole overlap wavefunction.
The energy of a spontaneously emitted photon corresponds to the energy-gap between the recombining electron-hole pair. The spontaneous emission spectrum then has a peak at a slightly higher energy than the band-gap. This is due to the higher concentration of excited carriers near the edges of the band. While the spontaneously emitted photons are emitted randomly in all directions a small portion of them are coupled into the optical waveguide. The ratio of coupled photons to the total number of spontaneously emitted photons is approximately $\frac{1}{M}$ where M is the number of possible optical modes in the cavity. These photons can go on to induce further recombinations and so the spontaneously emitted photons can be thought of as the trigger for the amplified spontaneous emission process. Maximising overlap of electrons and holes in the QWs increases the level of spontaneous recombination. For this reason semi-polar and non-polar GaN are being investigated as potential materials for SLED fabrication. These orientations of GaN do not have the same inbuilt piezoelectric field which causes spatial separation of electrons and holes in the QWs in c-plane GaN.

2.4.2 Stimulated Emission

Stimulated emission occurs when a downward transition of an excited electron and recombination with a hole is induced by a photon. The resultant emitted photon will have the same energy, phase and direction as the photon which induced the transition. The rate equation for photon density in a SLED or laser can be written in terms of the recombination rates from Equation 2.4 as:

$$\frac{dS}{dt} = R_{stim} + \beta R_{spon} - \frac{S}{\tau_S} \tag{2.6}$$

Where S is the number of photons per unit volume. The isotropically emitted spontaneous emission is scaled by the factor β which represents the proportion of spontaneously emitted photons coupled into the waveguide. The $\frac{S}{\tau_S}$ term refers to the photon losses due to absorption where τ_S is the photon lifetime. If the gain in the waveguide is positive, the photons in the waveguide will induce further stimulated recombination, as a photon travels along the waveguide the photon density will increase as:

$$S(z) = S(0) \cdot e^{(\Gamma g - \alpha)z} \tag{2.7}$$

Where $z = \frac{ct}{n_{eff}}$ is the distance travelled by a photon along the waveguide, c is the speed of light in a vacuum, n_{eff} is the effective refractive index of the material, g is the material gain and α is the waveguide loss.
Assuming that stimulated emission is the dominant photon generation mechanism above threshold, the time derivative of Equation 2.6 gives the stimulated emission rate as:

$$R_{stim} = \Gamma g v S \tag{2.8}$$

Where the velocity of light in the semiconductor $v = \frac{c}{n_{eff}}$. The rate of stimulated emission is then directly proportional to the photon density and the gain. Gain will be discussed in more detail in Section 2.5.
In a conventional laser diode the reflective facets would lead to photons completing multiple round trips of the cavity. This leads to the formation of resonant cavity modes which favour the amplification of certain wavelengths leading to very narrow discrete spectra. As a broad smooth spectrum is desirable in SLEDs steps are taken to prevent reflections at the facets so that any photon only makes a single pass along the waveguide. In this particular scenario the stimulated emission process is known as amplified spontaneous emission (ASE). The absence of reflections at the facets has implications on the carrier density distribution in the device. If the distribution of photons in a device of length L is modelled by considering two waves travelling in opposite directions then the photon density at any point along the waveguide is given by Equation 2.9.

$$S(z) = \frac{\beta}{\Gamma g - \alpha} \cdot \left(e^{(\Gamma g - \alpha)z} + e^{(\Gamma g - \alpha)(L-z)}\right) \tag{2.9}$$

This leads to a non-uniform distribution of photon density across the waveguide with the maximum density at either end. ASE is a faster recombination process than spontaneous emission and becomes increasingly fast with increasing photon density with the ASE recombination lifetime in the order of femtoseconds while spontaneous transitions typically have a lifetime of several nanoseconds [60]. This means that regions of the devices with a higher density of photons will be dominated by stimulated recombination. This results in lower carrier density at the waveguide ends due to a high level of stimulated recombination. This non-uniformity becomes more pronounced as the gain increases. This effect is illustrated in Figure 2.4.

Lower carrier density decreases the transparancey of the waveguide and can cause a reduction in the efficiency of the device. After a certain point extra current injection will not result in an overall increase in carrier density due to the high level of photons in the waveguide inducing stimulated recombination. This effect needs to be considered when designing SLEDs as the optimal point to operate is the lowest current density which still achieves the maximum possible carrier density.

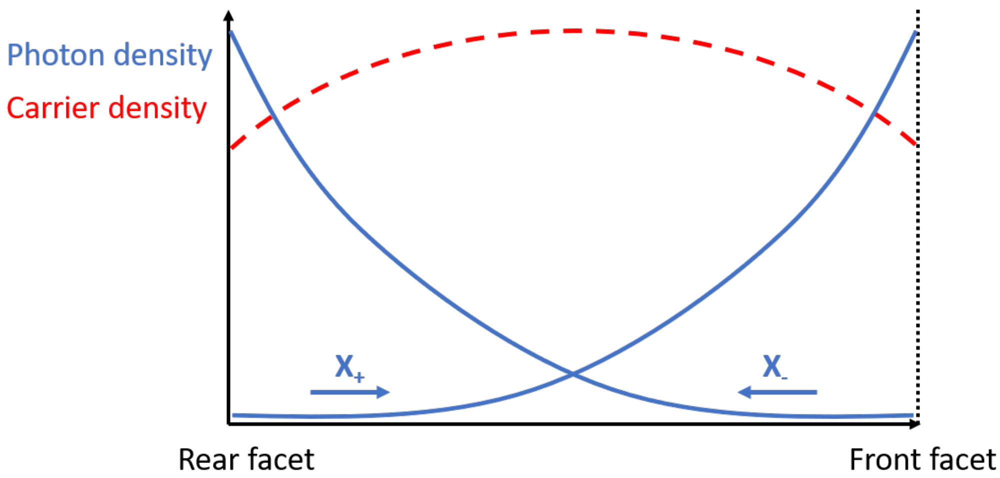

Figure 2.4: Above transparency photon and carrier density distribution for a SLED calculated using equation 2.9 with a positive net gain of 30 cm^{-1}.

2.5 Gain

2.5.1 Material gain

From Fermi's Golden Rule, the photon induced upward (W_{Abs}) and downward (W_{Em}) transmission rates between the conduction and valence bands can be written as [61]

$$W_{Abs} = \frac{2\pi}{\hbar}|H_{eh}|^2 \rho f_v(1 - f_c) \tag{2.10}$$

$$W_{Em} = \frac{2\pi}{\hbar}|H_{eh}|^2 \rho f_c(1 - f_v) \tag{2.11}$$

where the the Hamiltonian squared:

$$|H_{eh}|^2 = (\frac{eA_0}{2m_0})^2 |M_T|^2 \tag{2.12}$$

ρ is the density of states, f_v and f_c are the Fermi distributions given in equations 2.1 and 2.2, M_T is the transition matrix element and A_0 is the constant vector potential.
As carrier density increases with applied current, the gap between the quasi Fermi levels increases. When the carrier density exceeds a certain transparency density N_{Tr} and population inversion is achieved the number of downward transitions begin to exceed the number of absorption events. The material now has optical gain.
The material gain g_{mat} is the difference between the number of downward transitions $W_{Em} - W_{Abs}$ and upward transitions. Using Equations 2.10 and 2.11 gain can be written as:

$$g_{mat} = \frac{2\pi}{\hbar}|H_{eh}|^2 \rho(f_c - f_v) \tag{2.13}$$

It is clear that a greater separation of quasi-Fermi levels and higher density of states will provide higher levels of material gain. The $(f_c - f_v)$ part of Equation 2.13 is dependent on the level of current injection. Increasing the excited carrier density by injecting current then will lead to increased gain in the material, allowing for greater levels of light amplification. The gain at a given energy level is saturated when the Fermi function reaches its maximum value of 1. The other terms in Equation 2.13 relate to properties which are inherent to the material and are not influenced by the applied current.

2.5.2 Modal gain

In shallow etched ridge waveguide devices the size of the optical mode will exceed the size of the waveguide. Amplification takes place in the region where the mode overlaps with the active region, as shown in Figure 2.3. The modal gain takes this into account with the addition of the optical confinement factor Γ so that

$$g_{mod} = \Gamma g_{mat} \tag{2.14}$$

The optical confinement factor Γ is given by

$$\Gamma = \frac{V_a}{V_{mod}} \tag{2.15}$$

where V_a is the volume of the active region and V_{mod} is the volume of the optical mode. The optical confinement factor can be influenced by the epitaxial layer structure and by engineering the optical mode. These parameters should be optimised to give the maximum modal gain for a given current density.

2.5.3 Loss

The total loss α can be expressed as:

$$\alpha = \alpha_i + \alpha_m \tag{2.16}$$

where α_i is the internal waveguide loss and α_m is the mirror loss.
The mirror loss describes photons which exit the waveguide through the facet. These photons form the beam of the SLED. The internal losses describe photons which are lost due to parasitic absorption and through scattering on the side walls of the waveguide. The total loss defines the threshold gain for a laser.

$$\Gamma g_{thr} = \alpha \tag{2.17}$$

As the facets of a SLED are designed to have much lower reflectivity than the facets of a laser diode and FP modes are not formed, the threshold is less well defined than for a laser. Rather than instantly switching to a higher slope efficiency regime at transparency as a laser would, when the gain overtakes the loss there is an exponential increase in power with current.

2.6 Non-radiative recombination

Non-radiative recombination in semiconductors can broadly be described by two processes: Shockley-Read-Hall (SRH) recombination and Auger recombination. The total non-radiative recombination rate is then roughly:

$$R_{non-rad} = R_{SRH} + R_{Aug} \tag{2.18}$$

Both of these processes generate vibrations in the lattice which increase the overall temperature of the semiconductor. The device efficiency is reduced by these processes as they use up carriers which could otherwise combine radiatively.

SRH recombination is caused by defects in the crystal lattice. These defects create states at ‘forbidden’ energies between the conduction and valence bands. The energy released as electrons drop down from these trap states is in the form of a phonon. The rate of SRH recombination is directly proportional to the carrier density, N,

$$R_{SRH} = AN \tag{2.19}$$

where the constant A is the SRH recombination coefficient.

As these trap states exist within the band-gap they can be filled even when the carrier density is low. Choosing high quality materials with low defect densities can reduce the effects of SRH recombination on a device.

Auger recombination occurs when an electron drops from the conduction band to the valence band and the energy is released in the form of a phonon. This energy is transferred to another electron which is excited to a higher energy within the conduction band. When the second electron loses energy and returns to the bottom of the conduction band, the energy released is in the form of lattice vibrations. Auger recombination takes place at high carrier densities as it is a three particle interaction which increases proportionally to the carrier density cubed. The Auger recombination rate is written as:

$$R_{Aug} = CN^3 \tag{2.20}$$

where the constant C is the Auger recombination coefficient. As SLEDs require high current density to operate, a high level of Auger recombination is a potential barrier to high efficiency. It is often cited as the reason for the efficiency droop noticed at high current in GaN based LEDs [62]. This effect is discussed in more detail in the next section.

2.7 SLED operation

When the net gain in the waveguide is positive, a SLED is said to enter the superluminescent regime. For an ideal SLED i.e $R_1 = R_2 = 0$ the power output from a SLED in superluminescent mode can be written:

$$P_{ideal} = P_{sp} \cdot (e^{(\Gamma g(N,\lambda)-\alpha)L} - 1) \tag{2.21}$$

where $g_{mat}(N, \lambda)$ is the carrier density and wavelength dependent material gain and P_{sp} is the power of the guided component of the spontaneous emission.

For laser diodes, a certain 'threshold' current density where population inversion is achieved, a sharp superlinear increase in power output is observed. In SLEDs, however, the transition between the spontaneous emission regime and superluminescent or amplified spontaneous emission regime follows a gradual exponential curve. This difference is illustrated in Figure 2.5.

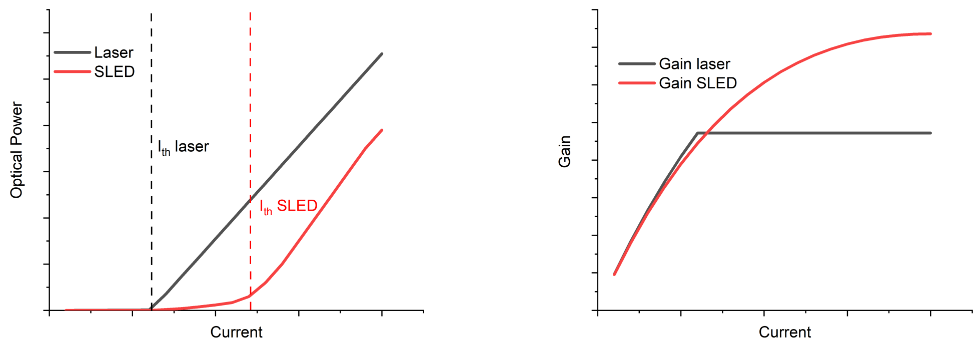

Figure 2.5: Plots showing the (a)difference in typical L-I curves for a laser diode and SLED and (b) typical gain vs current curves for a laser diode and SLED.

Increasing current density will increase the carrier density allowing for higher gain and higher optical power. This trend continues until all of the available states are filled and the carrier density reaches a maximum value. When the carrier density no longer increases with increasing current, a phenomenon called gain saturation is observed. As there are no more carriers available for stimulated recombination the device power levels off with increasing current. Once the material gain has been saturated, it is no longer efficient to increase the applied current density as it will only lead to more heat generation which made cause the device to degrade. Due to the extraction of photons after a single pass along the waveguide this gain clamping process will occur more

slowly than it would in a laser diode where the gain is immediately clamped above threshold.
In superluminescent mode the overall spatial coherence of the light emitted from the device increases. Below transparency where all of the light is emitted spontaneously the emission pattern will be Lambertian i.e. uniform in all directions. Above transparency the ASE process produces more photons travelling in the same direction. As the ratio of directional photons generated increases with respect to spontaneously emitted photons the far field pattern moves away from the Lambertian as most of the light is emitted through a smaller solid angle. This allows for better coupling of the light into optical systems.
In the superluminescent regime, the emission spectrum begins to narrow. This is due to wavelengths closer to the peak of the gain spectrum being amplified preferentially to those wavelengths further from the peak. The peak of the amplified spontaneous emission spectrum is at a lower energy than the peak of the spontaneous emission spectrum. This is due to the higher density of states at lower energies. This means that population inversion is most easily achieved at these energies and so most of the light amplification takes place at these energies.
The light amplification causes narrowing of the emission spectrum while the suppression of Fabry-Perot mode formation prevents the spectrum from narrowing to a series of discrete lines. This puts the SLED between a laser and LED in terms of spectral quality. This is illustrated in Figure 1.1.

2.7.1 Carrier recombination and efficiency droop

An obstacle to the efficient operation of nitride devices at high current density is the efficiency droop phenomenon. This is the reduction in internal quantum efficiency of GaN based emitters at high levels of injection. One of the main explanations offered for this phenomenon is Auger recombination [63–65]. As Auger recombination is a three-particle interaction which is proportional to the carrier density cubed, it becomes dominant at when high carrier densities are present. This is important to consider in modelling SLEDs as high levels of current injection and carrier density are required to reach the superluminescent regime. For this reason, the relative recombination rates of non-radiative Shockley-Read-Hall (SRH) recombination, spontaneous emission, Auger recombination and stimulated emission were modelled to allow for the potential impact of Auger in a SLED at high injection to be

estimated.
Using equations 2.3, 2.5, 2.7, 2.19 and 2.20 and assuming a low rate of external optical excitation, the carrier density rate equation can be written as:

$$\frac{dN}{dt} = \frac{J}{q} - AN - BN^2 - CN^3 - \frac{cgS}{n_{eff}} \tag{2.22}$$

This gives recombination in the InGaN QWs. The values used for the recombination coefficients were $A = 5 \times 10^6 s^{-1}$, $B = 10^{-10} cm^{-3} s^{-1}$ and $C = 10^{-31} cm^{-6} s^{-1}$ [66]. Above J_{thr} stimulated recombination comes into effect. The photon density in the device was calculated using equation 2.9. Plotting the fraction of current going to each recombination mechanism against current density gives the result shown in Figure 2.6.

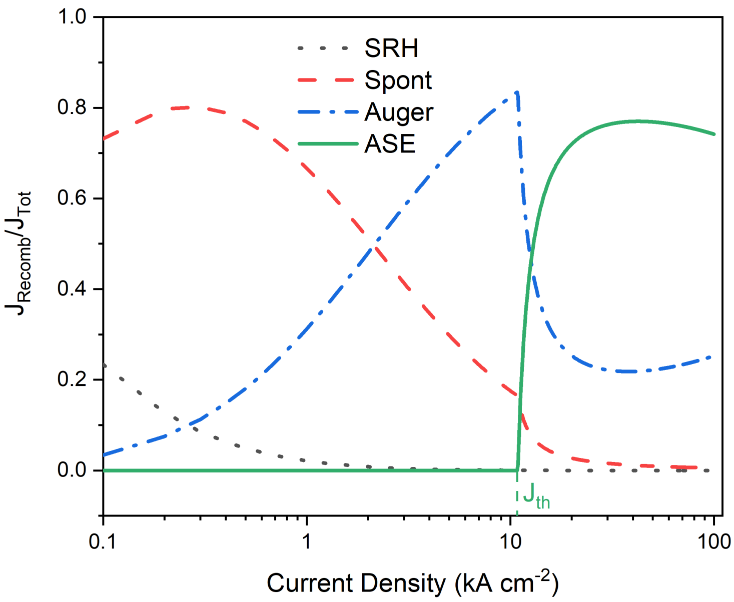

Figure 2.6: Recombination in SLED against current density.

Initially the SRH recombination dominates however this term is quickly saturated and overtaken by the spontaneous emission rate. Close to J_{thr} the Auger recombination increases to a level similar to that of the spontaneous emission. Above transparency however the stimulated emission quickly dominates. This is because the stimulated emission is proportional to the photon density, which increases exponentially above transparency. This is a faster increase even than the N^3 relationship by which Auger recombination increases. The rate of stimulated emission initially prevents Auger

recombination from causing efficiency droop above transparency. Similar results have previously been reported in laser diode modelling [62].
The dominance of stimulated emission can bee seen in Figure 2.7 by looking at the total level of recombination in the device. Above transparency, J_{recomb} increases rapidly with current density due to the rate of stimulated recombination.

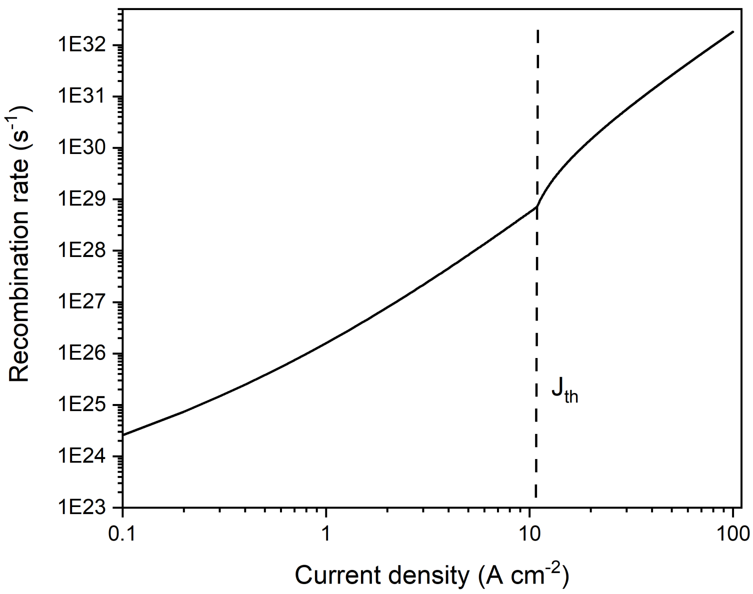

Figure 2.7: Total recombination in a SLED with increasing current density.

When the gain saturates at very high levels of injection ($> 100kAcm^{-2}$) the Auger may become the dominant recombination mechanism. Such high levels of injection are however unlikely to be required to achieve maximum efficiency and would probably result in damage to the device.

2.7.2 Power conversion efficiency

Power conversion efficiency (PCE) is a measure of how much of the electrical power applied to the device is converted into optical power. This measure takes into account not only the proportion of injected carriers which recombine radiatively, but also the energy of the injected carriers. If a the injected carriers have a higher energy than the emitted photons, the excess energy will be released as heat, reducing the efficiency of the device. The power conversion efficiency η_p is given by [67]:

$$\eta_p = \frac{\eta_i h\nu}{qV} \tag{2.23}$$

where η_i is the internal quantum efficiency (IQE) and V is the applied bias. LEDs tend to have high peak PCE as they operate at low current. Lasers and SLEDs however require high current density to reach threshold. High voltages are required to supply these currents, increasing the energy of the injected carriers. Figure 2.8 shows a comparison of PCE for a GaN based LED, SLED and laser with identical A, B and C recombination coefficients and in the case of the SLED and laser, identical gain curves. The extraction efficiency is assumed to be 1.

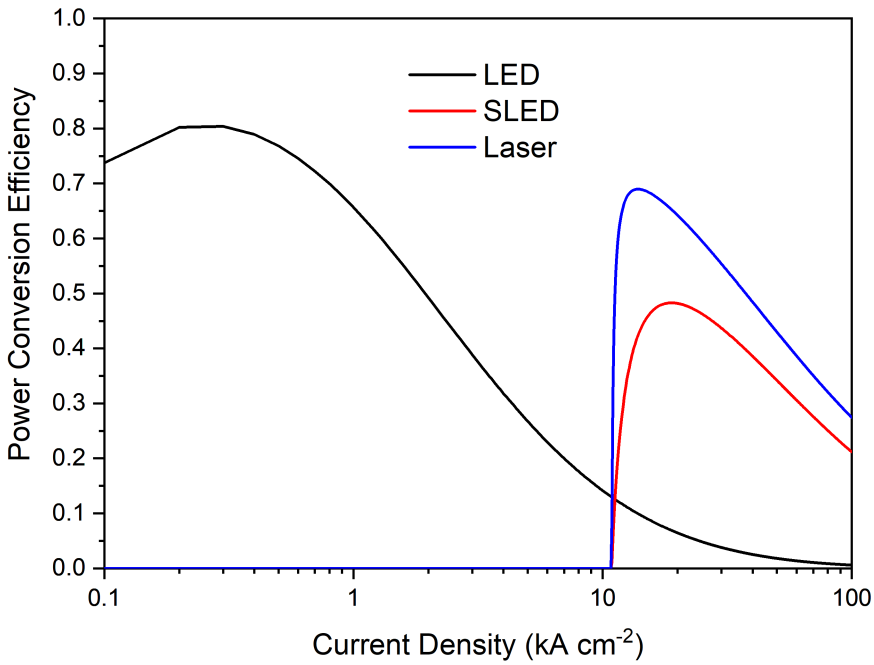

Figure 2.8: Example of power conversion efficiency for GaN based LED, SLED and laser.

The LED reaches the highest PCE of 0.8 at 300 Acm^{-2}. The laser and SLED have lower peak PCE values of 0.7 and 0.5 respectively due to the higher energy of the injected carriers. Reducing the resistivity of the contacts and of the p-GaN layers would help to improve the PCE of the SLED and laser. The laser shows greater efficiency due to photons making multiple round trips in the cavity. The higher photon density in the laser cavity results in more stimulated emission and a higher IQE than in the SLED. Introducing a reflective back facet to the SLED to allow for a single round trip of the cavity could increase the IQE in the SLED, however the spectral quality could be reduced. This will be discussed in more detail in Chapter 3.

2.8 Facet reflectivity management

The key distinction between SLEDs and laser diodes is in the management of the facet reflectivity. For laser diodes, highly reflective facets are desirable to allow for multiple round-trips of the cavity and the formation of Fabry-Perot modes. In the case of SLEDs it is preferred to have facets with low reflectivity to prevent the formation of modes and maintain a broad, smooth emission spectrum.
From the Fresnel equations the reflectivity of the interface between two media with refractive indices n_1 and n_2 for a normally incident beam is given as:

$$R_{12} = |\frac{n_1 - n_2}{n_1 + n_2}|^2 \tag{2.24}$$

For example for a GaN based device with a waveguide index of $n_{GaN} = 2.4$ the facet reflectivity is $\sim 17\%$.
To analyse the impact of facet reflectivity on a SLED, a Fabry-Perot cavity with finite reflectivity is considered where the power output P_{out} is

$$P_{out} = \frac{\beta}{\Gamma g - \alpha} \cdot (G_s - 1) \cdot (\frac{(1 - R_F)(R_B G_s + 1)}{1 + (R_F R_B G_s)^2 - 2 R_F R_B G_s cos(\frac{4\pi L n}{\lambda})} \tag{2.25}$$

where R_1 and R_2 are the facet reflectivities, and n_{wav} is the waveguide refractive index and $G_s = e^{(\Gamma g - \alpha)L}$ is the single pass gain. The magnitude of the cosine term is dependent on wavelength and facet reflectivity. The maximum and minimum powers at a given wavelength P_{max} and P_{min} occur when the Cosine term is equal to zero and one respectively.
The spectral modulation depth is defined as:

$$D_{mod} = 1 - \frac{P_{min}}{P_{max}} \tag{2.26}$$

The modulation depth then is dependent on the facet reflectivity as higher reflectivity will increase the magnitude of the cosine term in Equation 2.26. Keeping the modulation depth to a minimum is very important for maintaining a broad, smooth emission spectrum. The influence of facet reflectivity on the output power and spectra of SLEDs will be discussed in more detail in the next chapter.

2.8.1 Fabry-Perot modes

The way in which parasitic lasing can occur in a SLED device is by the formation of a Fabry-Perot cavity. This cavity is formed by two parallel reflective surfaces at either end of the semiconductor waveguide. When two waves of equal frequency are travelling in opposite directions in such a cavity, destructive and constructive interference results in a standing wave. The allowed wavelengths in the FP cavity are given by:

$$\lambda_l = \frac{2nL}{l}, \tag{2.27}$$

where L is the length of the waveguide, n is the refractive index of the semiconductor and l is the mode number. The wavelengths which do not satisfy Equation 2.27 are suppressed. The result is a series of narrow linewidth peaks in the spectrum. These modes are separated by $\delta\lambda$, which is given by

$$\delta\lambda = \frac{\lambda_0^2}{2nL}. \tag{2.28}$$

As the formation of these standing waves is dependent on photons making multiple round trips of the cavity, reflections at the facet increase their prominence. While no device can have zero facet reflectivity, minimising the reflections at the facet can help to prevent the formation of these modes.

2.9 Thermal management

In order to reach the levels of gain required for a SLED to produce high optical powers, large current densities must be applied to the device. This inevitably leads to high levels of non-radiative recombination and heat generation in the device.

Heat is generated in SLEDs by Joule heating. The metal-semiconductor interface provides a resistance. When a current density J is applied to the device heat is generated at a rate P.

$$\frac{P}{A} = J^2 \rho_C \tag{2.29}$$

where ρ_C is the contact resistivity and A is the area of the contact. As very large current density is required to achieve population inversion, it is crucial to minimise the contact resistivity.

As some level of contact resistivity is unavoidable, steps can be taken to reduce the thermal load on the device. Thick bondpads can help to dissipate heat generated under the metal contacts away from the junction.
The active-region can also be a source of heat. At high current density the Auger recombination becomes significant as it goes with the carrier density cubed. In a SLED however this can often by reduced as stimulated emission is the dominant recombination mechanism at high current density. This is discussed in more detail in section 3.3.

These heating effects must be considered as they can impact the device efficiency by reducing the gain and lifetime by thermal runaway. High temperatures can also result in short circuits and the localised failure of the metal contact. Methods such as utilising packaging to dissipate the heat or operating the device in pulsed mode can be used to reduce their effect.

2.10 Spatial and temporal coherence

Key advantages of SLEDs over LEDs and laser diodes can be explained in terms of spatial and temporal coherence. It is the unique combination of high spatial coherence and low temporal coherence which makes SLEDs suitable for applications such as pico-projection, optical coherence tomography (OCT) and fibre-optic gyroscopes.

2.10.1 Spatial coherence

Spatial coherence describes the relationship between waves at a given point in space. If a wave has only single value of amplitude over a region of space it is said to be perfectly spatially coherent in this region. This would be the case for a monochromatic point source.

For sources of a finite size and emitting multiple wavelengths however, the photons emitted from different points on the source may not be perfectly correlated in phase and wavelength. Spatially coherent sources then, are emitters which emit photons with a fixed phase relationship. The spatial coherence of a source can be measured using a Young's slits experimental setup [68]. When the slits are illuminated by a coherent source a set of interference fringes are visible. The spatial coherence can be determined using these fringes by the relation:

$$\mu = \frac{I_{max} - I_{min}}{I_{max} + I_{min}} \tag{2.30}$$

Where I_{max} is the central peak intensity and I_{min} is the neighbouring valley intensity.
The ASE process produces photons with identical phase and direction to the photon which induces recombination. This means that SLEDs operating in the superluminescent regime will be highly spatially coherent. Deng et al. showed that SLEDs can demonstrate $\mu = 0.67$, close to that of a laser diode ($\mu = 0.81$). In LEDs, where the photons are emitted spontaneously over a large area with random direction and phase relationship the spatial coherence is low, less than 0.1. Spatially coherent sources are useful for systems in which the light must be directed or controlled by optics.

2.10.2 Temporal coherence

Temporal coherence describes the correlation between waves over time. In effect temporal coherence is a measure of how monochromatic a light source is. It measures the degree of interference a wave can have with itself at a given time. Equation 2.31 gives the coherence length for a light source with a Guassian emission spectrum [69].

$$L_c = \frac{2ln(2)}{\pi}\frac{\lambda^2}{\Delta\lambda} \tag{2.31}$$

Where λ is the central emission wavelength and $\Delta\lambda$ is the full width half maximum of the emission spectrum.
A perfectly monochromatic source will have infinite temporal coherence. Waves with a broader range of frequencies will have a shorter L_c and decorrelate quickly. Because of the formation of FP modes in laser diodes, these devices tend to have very narrow bandwidth and high temporal coherence. This can lead to interference effects such as speckle when the light

strikes a surface [70]. The high degree of correlation between incoming and reflected waves allows for destructive interference to occur. In LEDs and SLEDs, the broad spectrum means there are several frequencies in the travelling wave. The wave decorrelates quickly. The lack of correlation means that effects such as speckle and diffraction have less of an impact on these devices.

The level of temporal coherence is equivalent to the axial resolution of OCT systems. The axial resolution also depends on the peak wavelength of the system, with shorter wavelengths providing shorter coherence lengths. This means that GaN based blue SLEDs in particular could be an ideal light source for high resolution OCT. GaN SLEDs have been demonstrated to provide axial resolution of less than $7\mu m$ [44].

2.11 Summary

Superluminescent LEDs based on GaN are based on similar principles to laser diodes. To obtain superluminescence, high power and high efficiency, carrier population inversion must be achieved by electrical injection. As the light is only amplified in a single pass along the waveguide, and mirror losses are high, SLED can be expected to have a higher transparency current density than a laser diode. The high gain required for the device to operate in superluminescent mode can be achieved by applying high current density to the device generating a high carrier density in the QWs. As the carrier density in a SLED is not clamped at threshold as it is for a laser diode, increasing carrier density above threshold can provide high levels of gain and optical power. The number of QWs can influence the threshold and overall gain and will be investigated in the next chapter.

The various recombination mechanisms in a SLED are examined. Simulations show that GaN SLEDs may be able to overcome the efficiency droop which affects GaN based LEDs. Once transparency is reached the combination of increasing gain with drive current and increasing photon density result in a large amount of stimulated emission. The rapid increase in stimulated recombination above transparency prevents Auger from becoming the dominant recombination mechanism in a SLED.

The high carrier and current densities cause heat to be generated in SLEDs. Contacts with low resistivity are required to reduce the amount of Joule heating which can cause degradation and failure.

Chapter 3

Design and Optimisation of SLEDs

3.1 Introduction

Several factors can influence the performance of SLEDs including the device geometry, facet reflectivity, wafer structure and thermal management. The interaction of these factors determines the maximum achievable power, efficiency, spectral quality and modulation speed of the device. The goal of this chapter is to find the combination of these factors which provide the best balance of low transparency, high power and low temporal coherence.

While a certain amount can be achieved using analytical models and experimental studies, this can require high degrees of complexity in the case of analytical models, and, in the case of experimental work, can be time consuming and limited in the number of variations which can be examined. A numerical tool which could calculate the impact of different device geometries, facet reflectivities and wafer structures could help to find the optimal device design without the need for expensive and lengthy trial and error based fabrication.

Section 3.4 presents a numerical model used to analyse the impacts of these parameters and discussed how best to use them to optimise SLEDs for a given application. The model considers the co-dependent relationship of the carrier and photon densities in the waveguide, using these parameters to calculate the optical gain. The average optical gain over the entire waveguide is then used to calculate the output power and spectral modulation depth. The model is designed to work with any III-V material system so that the simulation of SLEDs at any wavelength can be done provided there is knowledge of the relationship between optical gain and carrier density in the active material.

The model provides insight into which factors are the most important for achieving the best SLED performance. Low facet reflectivity emerges as the most important design feature for high power devices as maintaining spectral quality becomes more difficult when dealing with a high density of photons. While the model in this chapter describes the potential capability of ideal SLEDs, in practicality there are many limitations on device performance. These include degradtion due to heating, limitations of current sources and fabrication considerations. The model presented in this chapter is used to optimise the devices within these limitations and this will be discussed further in Chapter 5.

3.2 Design considerations for SLEDs

The parameters which will be discussed in relation to their impact on SLED performance are:

- **Length**
  The length of the waveguide can have a significant effect on SLED performance. As seen in Equation 2.21, increasing the device length can exponentially increase the optical power output from a SLED. The longer device length will also increase the area of the p-electrode however which will increase the level of applied current needed to reach transparency and to reach equivalent levels of gain as shorter devices. This has implications for the efficiency of the device at different currents. The shorter devices are more efficient at lower currents due to their lower threshold while longer devices become more efficient at higher currents as the amplification of light is greater once threshold is reached. This needs to be considered when designing a SLED for a given application. Knowing the level of power required, the most appropriate length can be chosen for maximum efficiency.
- **Width**
  Increasing the width of the waveguide increases the emitting area of the device, increasing the maximum possible optical power output. Increasing the width of the waveguide introduces also introduces extra risks by increasing the potential for the device to operate in filamentary mode and for the formation of higher order modes.
- **Material Gain**

Different numbers of QWs will provide different levels of material gain. This should be considered before designing a SLED for a given material system. Materials with higher material gain can potentially provide very high optical power, however high values of gain can also make these materials more prone to lasing so extra steps may need to be taken to maintain good spectral quality. Other factors which can influence the overall material gain are the number of QWs, the material loss, the cladding layers and the strength of the QCSE which influences the overlap of the electron and hole wavefunctions. SLEDs with lower material gain may need different geometry (i.e. longer or wider ridges) than higher gain equivalents to achieve the same optical powers.

- **Facet reflectivity**
  The facet reflectivity is a crucial parameter to SLED operation. More highly reflective facets allow for a higher level of amplification and greater optical power. Increasing reflectivity can lead to narrowing of the spectrum and increase the modulation depth. Depending on the application, the ideal reflectivity must be chosen to give the best balance of optical power and spectral quality.

3.3 Modelling SLEDs

The symbols and values of parameters used in the model described in this chapter are summarised in Table 3.1.

Table 3.1: List of parameters used in modelling of SLEDs.

Symbol	Definition	Units	Value
$S^{\pm}$	Forward and backward propagating photon densities	cm^{-3}	
$s^{\pm}$	Normalised forward and backward propagating photon densities		
$N(z)$	Carrier density distribution	cm^{-3}	
N_{tr}	Carrier density at transparency	cm^{-3}	7×10^{18}
A	Non-radiative recombination coefficient	s^{-1}	5×10^{6}
B	Radiative recombination coefficient	$cm^3 s^{-1}$	10^{-10}
C	Auger recombination coefficient	$cm^6 s^{-1}$	10^{-31}
τ	Average carrier lifetime	s	2.5×10^{-9}
P_{out}	Optical power output	W	
P_{sp}	Optical power due to spontaneous emission	W	
β	Spontaneous emission coupling factor		10^{-3}
a	Linear gain coefficient	cm^2	1.5×10^{-16}
$g_{mod}(z)$	Modal gain	cm^{-1}	
g	Average material gain	cm^{-1}	
Γ	Optical confinement factor		
Γ_L	Optical confinement factor, lateral component		
Γ_T	Optical confinement factor, transverse component		
Π	Size of optical mode	cm^2	10^{-7}
z	Longitudinal position along waveguide length, z=0 is the rear facet	m	
J	Applied current density	Acm^{-2}	
λ	Wavelength	nm	
α	Optical loss	cm^{-1}	25
G_s	Single pass gain		
n	Refractive index		2.4
R_F, R_B	Front and rear facet reflectivity		
q	Electron charge	C	1.6×10^{-19}
L	Ridge length	cm	
w	Ridge width	cm	
d	Active region thickness	cm	
h	Planck's constant	Js	6.63×10^{-34}
ν	Frequency	s^{-1}	
c	Speed of light	ms^{-1}	3×10^{8}

3.3.1 Amplificiation, gain and loss

For modelling purposes the SLED can be considered to be similar to a semiconductor optical amplifier (SOA) with zero external optical input. In this model, the distribution of photons in the SLED waveguide is imagined as two waves travelling in opposite directions from opposite ends of the waveguide. The forward and backward propagating photon densities for an ideal SLED (zero facet reflectivity) S_+ and S_- at a position z in a waveguide of length L can be written as:

$$S_+(z) = \frac{\beta n_{eff} R_{spon}}{c(\Gamma g - \alpha)}(e^{(\Gamma g-\alpha)z} - 1) \tag{3.1}$$

and

$$S_-(z) = \frac{\beta n_{eff} R_{spon}}{c(\Gamma g - \alpha)}(e^{(\Gamma g-\alpha)(L-z)} - 1) \tag{3.2}$$

where g is the average gain across the waveguide, given by

$$g = \frac{1}{L}\int_0^L g(z)dz \tag{3.3}$$

and the power out from a single facet is

$$P_{out+} = h\nu c\Pi S_+(L) \tag{3.4}$$

where β is the spontaneous emission coupling factor, α is the waveguide loss and Π is the size of the optical mode [71].
In this simulation the values $\beta = 10^{-3}$ [72], $\alpha = 25cm^{-1}$, and $\Pi = 10^{-7}cm^{-2}$ were used. The α parameter was measured experimentally.
The material gain $g(z)$ is assumed to be linearly dependent on the local carrier density $N(z)$ which in turn is linearly dependent on the local photon density $S_+(z) + S_-(z)$. This mutual dependence demands numerical analysis of the system. To model the system numerically the waveguide is divided into n sections of length ΔL.

3.3.2 Carrier and photon distributions

From the model of a SOA by Brosson [73] the carrier density at a given position z along a waveguide of a SLED with current density J applied is:

$$N(z) = \frac{J\tau/qd}{1 + s_+(z) + s_-(z)} \tag{3.5}$$

where τ is the average carrier lifetime and q is the electron charge. The active region thickness d is equal to the number of QWs in the structure times their width. Here the photon density is normalised with $s_{\pm} = ca\tau S_{\pm}$. This inverse dependence of carrier density on photon density is due to the high rate of stimulated recombination as a result of the higher number of photons available to induce recombination.

In this model it is assumed that the material gain is linearly dependent on the carrier density, so the modal gain is given by:

$$g_{mod}(z) = \Gamma a(N(z) - N_{tr}) \tag{3.6}$$

where a is the constant of proportionality relating the material gain and the carrier density $N(z)$ and N_{tr} is the carrier density at transparency. In the simulations described in this chapter these parameters have the values $a = 1.5 \times 10^{-16} cm^2$ and $N_{tr} = 7 \times 10^{18} cm^{-3}$. These values are consistent with the reported characteristics for InGaN QWs [66, 74, 75]. It is expected that the increasing levels of stimulated emission will deplete the carriers at the waveguide ends reducing gain in these regions. When the photon density reaches a certain threshold the carrier density will no longer increase with increasing current as all available free carriers are used by the stimulated emission process. This leads to the saturation of carrier density and thereby the saturation of gain in the device. Finding the level of current at which the optical gain saturates can help to decide the ideal operating conditions for a SLED.

3.3.3 Numerical model

As the the carrier density, photon density and optical gain are mutually dependent on one another, a numerical model was used to simulate the system. The waveguide is divided into n sections of length ΔL as shown in Figure 3.1. The model assumes the initial carrier density is uniform across the waveguide of length L. This carrier density determines the gain through the relation in Equation 3.6 and spontaneous emission rate which are in turn used to calculate the photon density in each segment of the waveguide.

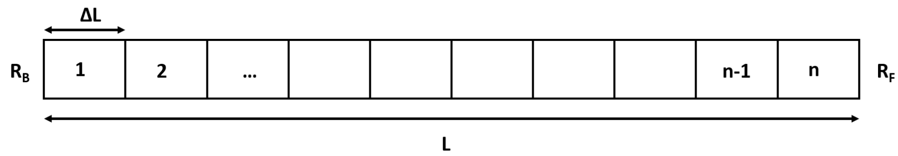

Figure 3.1: SLED waveguide split into n segments of length ΔL. The front and back facets have reflectivity R_F and R_B.

The program uses the changes in the photon density to continuously update the values for the carrier density and optical gain in each segment which on the next iteration would update the value for the photon density. The program was run until a steady state convergence was reached. The schematic in Figure 3.2 illustrates this process.

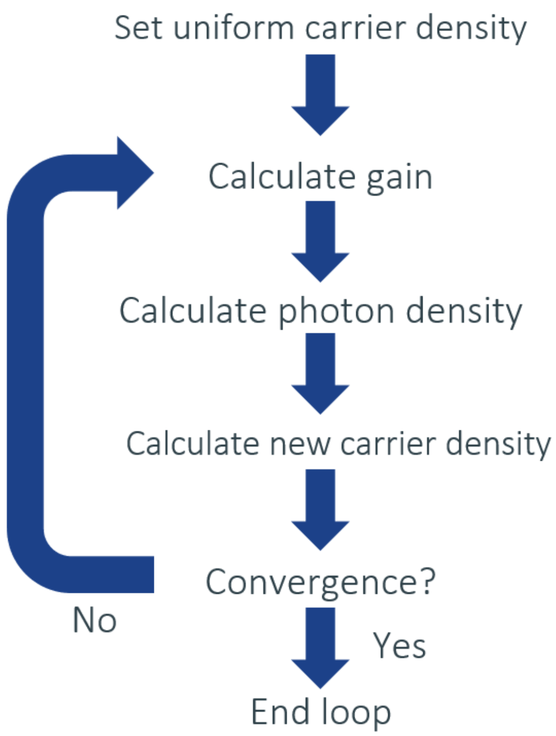

Figure 3.2: Schematic showing loop used to calculate steady state gain, photon density and carrier density in a SLED.

The following assumptions were used in the calculations:

1. The initial carrier density is distributed uniformly across the ridge.
2. Carrier leakage is negligible.
3. The material gain is constant with photon energy close to the peak wavelength.

4. The material gain evolves linearly with carrier density.
5. Polarisation is not included in the model.
6. The carrier lifetime τ is constant above transparency. From the recombination simulations above it is assumed that stimulated emission is the dominant recombination mechanism above transparency, with a carrier recombination lifetime of 300 ps. The other dominant mechanisms are Auger and spontaneous emission which are both assumed to have a lifetime of 10 ns. The carrier lifetime is calculated by $\frac{1}{\tau} = \frac{1}{\tau_{stim}} + \frac{1}{\tau_{nonrad}}$ to be 350 ps above transparency.

Once a steady state convergence had been reached the resulting gain value was used to calculate the optical power out of the device using the equation for the optical power from a Fabry-Perot cavity with finite facet reflectivity:

$$P_{out} = P_{sp}(G_s - 1)(\frac{(1 - R_F)(R_B G_s + 1)}{1 + (R_F R_B G_s)^2 - 2 R_F R_B G_s Cos(\frac{4\pi Ln}{\lambda})} \tag{3.7}$$

Where P_{sp} is the spontaneous emission coupled into the waveguide. This is approximated as $\beta B N^2$ where β is 0.1%. The equation is evaluated close to the peak of the gain spectrum where the gain has an approximately constant value.
The single pass gain G_s is given by:

$$G_s = e^{(\Gamma g - \alpha)L} \tag{3.8}$$

Where the gain g is the average material gain along the waveguide. This is calculated by taking the sum of the gain in each segment and dividing by the number of segments.

$$g = \frac{a}{L} \sum_{1}^{n} N(n) \tag{3.9}$$

An example of a gain curve calculated using this numerical model is shown in Figure 3.3 which shows the gain curve with current density in a 1 mm long device with a 3 μm long waveguide. The loss of $25 cm^{-1}$ is a value which was measured experimentally by extracting the gain curve from the measured L-I characteristic of a GaN SLED. This is discussed in more detail in Chapter 5. R_F and R_B are the front and back facet reflectivities. They are set equal to 0.1% unless otherwise specified.

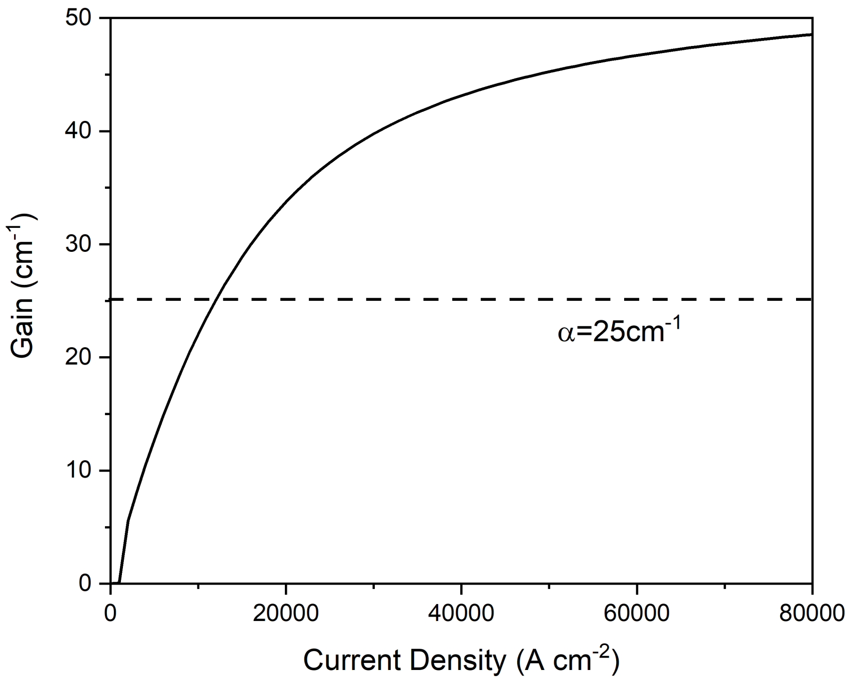

Figure 3.3: Modal gain curve for 1 mm GaN SLED with 2 QWs calculated using numerical model. The waveguide loss of $25cm^{-1}$ is a value which was measured experimentally.

The simulations were carried out for a number of different device parameters. In all cases the non-uniform longitudinal distribution of carriers and photons played an important role in determining the material gain and optical power output. An example of these distributions is shown in Figure 2.4

3.4 Length Variation

Figure 3.4 shows the simulated two-facet L-I curves of SLED devices of different lengths. The peak efficiency of each device occurs at different levels of current injection and output power. The longer devices are less efficient than shorter devices at low current as high current injection is required to reach the transparency current density. While shorter devices reach transparency more easily, the shorter length of the gain medium and smaller area means that the level of amplification is lower and that gain saturation occurs more quickly as high carrier density results in more non-radiative recombinations, heating up the chip and reducing the gain. This limits the maximum optical power which can be obtained from a given device. For example, the 0.5 mm long device shows the highest level of efficiency if 800 mW of power is required, however the 1 mm device becomes more efficient for generating powers greater than 800 mW.

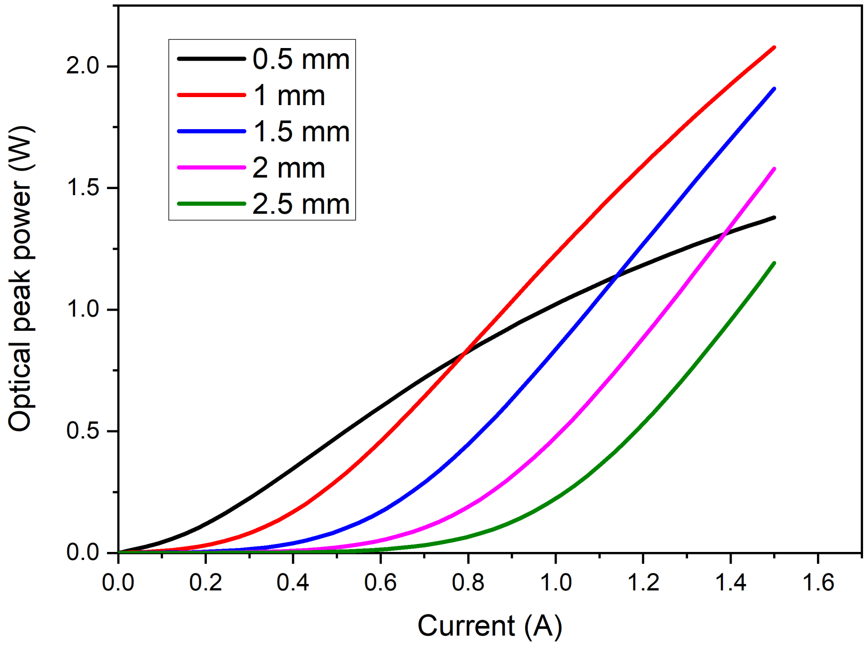

Figure 3.4: Simulated L-I curves of GaN SLEDs with different waveguide lengths.

Figure 3.5 shows the variation of power with length for devices with the same current density applied. The cases where non-uniform carrier density is considered and where a uniform carrier density model is used are compared. While the models show good agreement with one another at lower powers, there is a large deviation for devices with higher material gain. The potential increase in optical power which can be obtained by increasing the length is overestimated by the uniform carrier density model. The non-uniform model factors in the large decrease of carrier density near the waveguide ends which decreases the average gain. It is clear from these results that the non-uniformity of carrier density distribution in the waveguide must be considered when optimising the length of high-power SLEDs. The uniform carrier density model is a suitable model for lower power devices.

Increasing the length also results in an increase in modulation depth. Figure 3.6 shows simulated gain spectra for SLEDs of different lengths with 1% reflectivity at both facets and modal gain of 30 cm^{-1}. The gain spectrum is assumed to be Gaussian and symmetrical about the peak. While the 2.5 mm

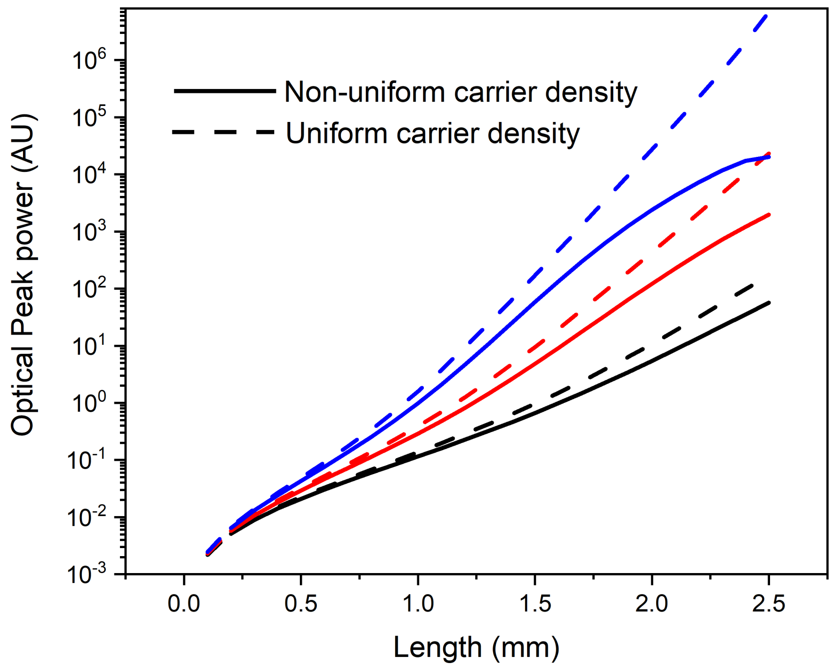

Figure 3.5: Power versus length for SLEDs with different material gain. The dotted lines show the uniform carrier density approximation. Solid lines show the non-uniform carrier density model.

device offers the highest power, the spectral quality is greatly reduced. The FWHM reduces from 5.5 nm to 4.2 nm as the length is increased from 1 mm to 2.5 mm. This should be considered if SLEDs are being designed for an application such as OCT where a short coherence length is key to achieving high axial resolution. In the example shown, the 2.5 mm SLED provides an axial resolution of 18.2 μm while the 1 mm device provides an axial resolution of 13.8 μm, albeit with lower optical power. Using an array or shorter SLEDs may be a more effective way to achieve high power while maintaining the broad spectrum required for such an application.

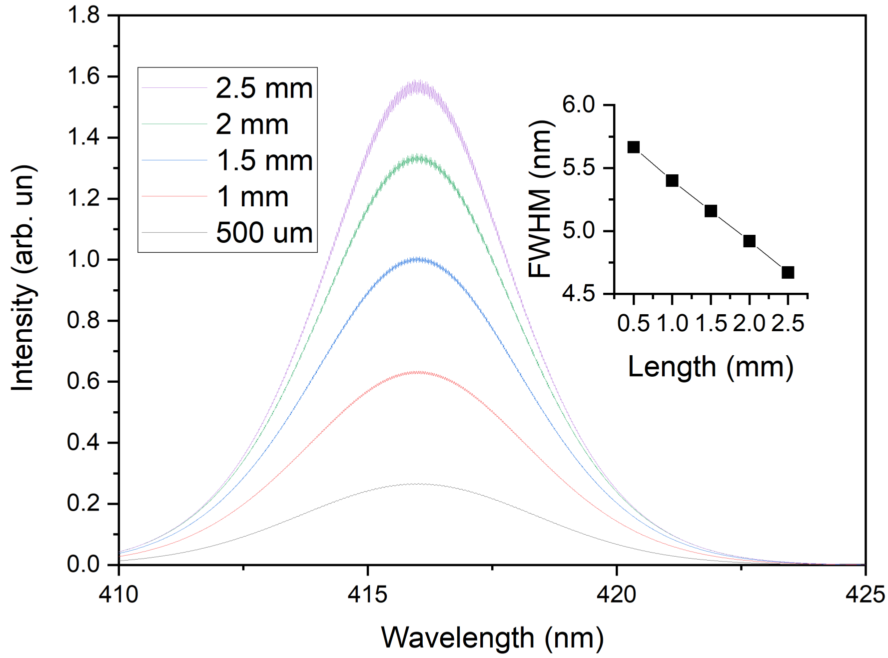

Figure 3.6: Simulated ASE spectra for GaN SLEDs of different lengths with 50 $kAcm^{-2}$ applied current density.

3.5 Width variation

A common method to achieve high optical power from a ridge waveguide device is to use a wide ridge, increasing the emitting area and the number of photons in the waveguide.This has the effect, however, of increasing the transparency current. This is a particular concern when designing a SLED as the transparency current is approximately double that of a laser diode based on the same material.

Increasing the width also has the benefit of increasing the lateral component of the optical confinement factor Γ. As a greater fraction of the generated photons overlap with the active area, the modal gain is increased. This reduces the transparency current density and increases the potential maximum optical power. Figure 3.7 shows the optical change in optical confinement factor and transparency current density with ridge width.

The risk associated with increasing the ridge width is that the device may begin to operate in filamentary mode with some sections of the waveguide lasing preferentially over others [76, 77]. This can lead to the formation of higher order which would distort the spectrum. This means that keeping the ridge as narrow as possible while maximising the Γ factor should be the objective when designing a SLED. Figure 3.8 shows the simulated L-J curves of SLED devices with different ridge widths. The devices in these simulations have a waveguide length of 1 mm and the reflectivity of both facets is 0.1%.

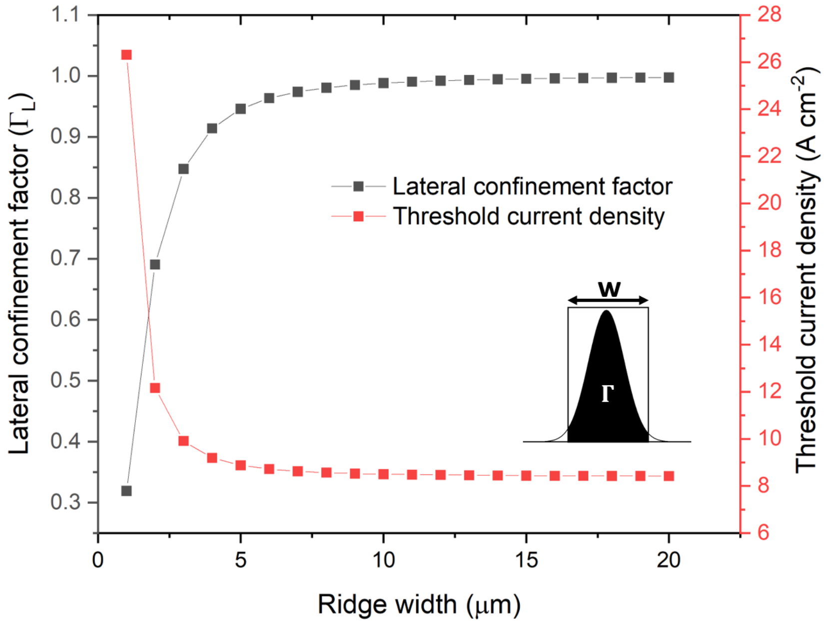

Figure 3.7: Lateral component of the optical confinement factor and transparency current density of a GaN SLED versus ridge width.

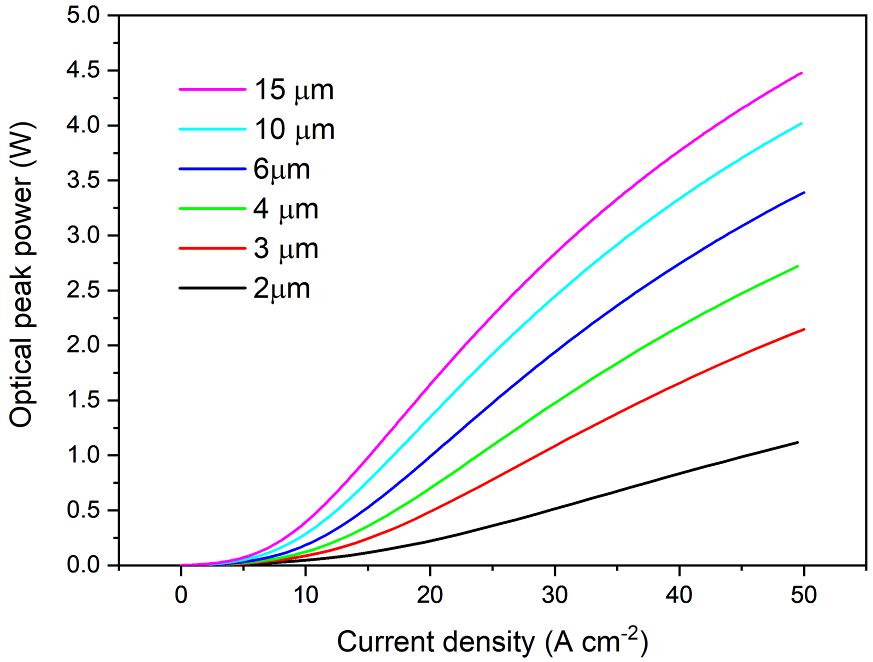

Figure 3.8: Simulated L-J characteristic for 1 mm long SLEDs with different ridge widths.

It is clear that wide ridge devices are more efficient at any current density due to their lower transparency current density and greater emitting area. The current required to reach these current densities is much greater, however, than it is for narrower ridge devices. Figure 3.9 shows the simulated L-I curve up to 2 A for devices with different ridge widths. The narrower ridge devices are more efficient in this region and therefore appear a better design choice for applications where the extremely high currents required to drive the wider devices cannot be easily supplied.

An advantage of using an increase in ridge width rather than length to increase optical power output is that the gain medium remains the same length. This means a lower modulation depth and a reduced chance of the device beginning to lase at high power. The optical power boost increases linearly with width however as the emitting area is increased, while increasing the length provides a superlinear increase in optical power.

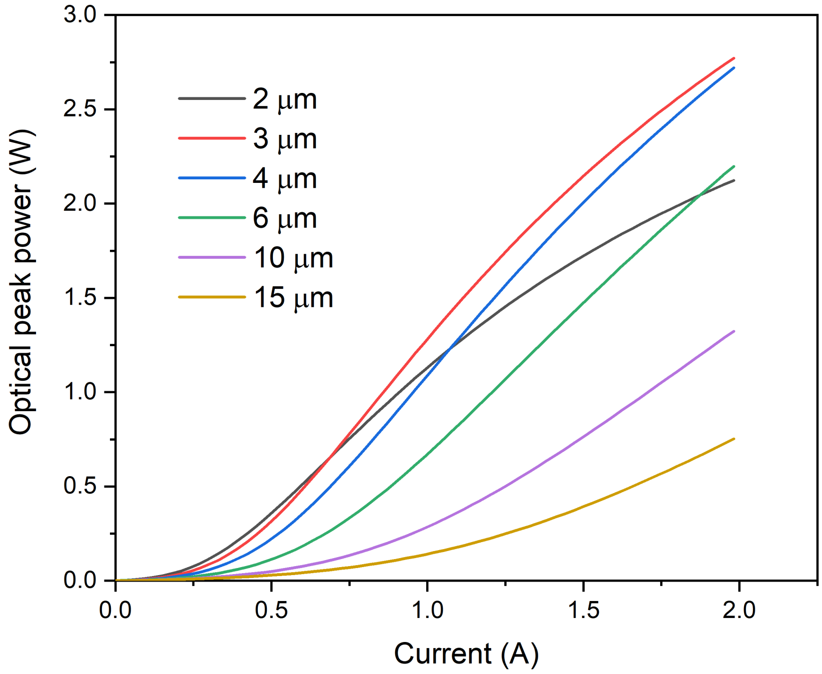

Figure 3.9: Simulated L-I characteristic for 1 mm long SLEDs with different ridge widths.

3.6 Facet reflectivity variation

Controlling the reflectivity of the facets is vital to prevent parasitic lasing and achieve high optical power. While an ideal SLED has zero reflectivity at the facets, optical power can potentially be increased by allowing some reflectivity at the back facet, allowing the light a double pass of the waveguide. This would lead to a greater level of stimulated recombination and greater amplification of the light in the waveguide. Figure 3.10 shows the evolution of power with device length for SLED devices with different facet reflectivity. In this case the SLED device is considered to be an InGaN based device with a modal gain of 60 cm^{-1}. The dotted lines show powers for which the modulation depth in the spectrum is above 0.5 and the curves cut off at the point where the modulation depth reaches 1 which is analogous to lasing.

The plot shows that a significant boost to output power can be achieved by increasing the rear facet reflectivity. The devices with rear facet reflectivity however are more prone to high levels of modulation. The results suggest that a small increase in rear facet reflectivity when combined with low front facet reflectivity can provide approximately one order of magnitude greater optical

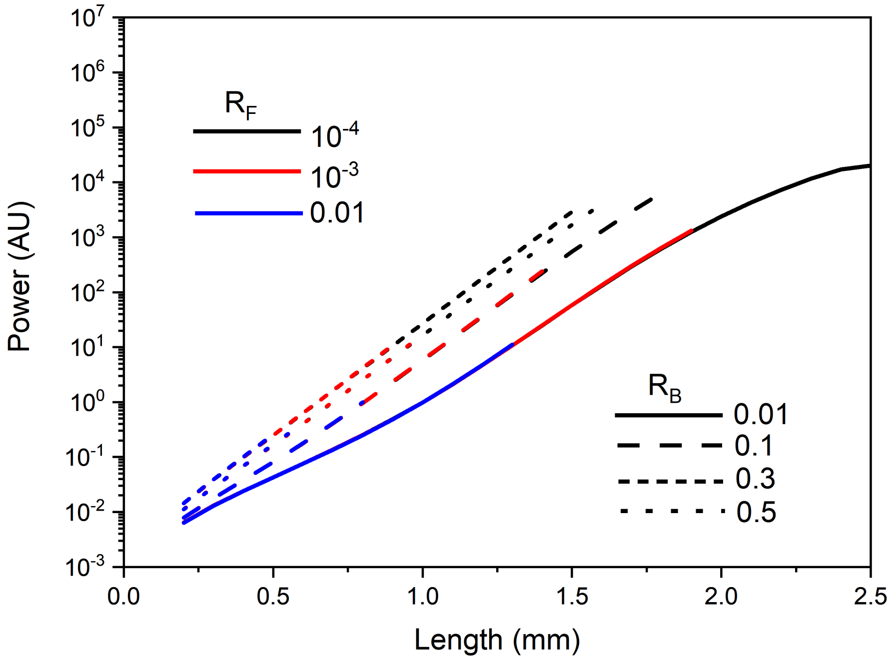

Figure 3.10: Power versus length for SLED devices with different facet reflectivities. The lines become dotted when the modulation depth exceeds 0.5.

power while maintaining a modulation depth less than 0.5.

For some applications where low temporal coherence is essential such as OCT or projection, low modulation depth is essential. Figure 3.11 shows the evolution of modulation depth with device length for devices with different facet reflectivities. The modulation depth increases rapidly with facet reflectivity. It is clear that maintaining very low front facet reflectivity is essential for applications where spectral quality is important. The simulations suggest that even a facet reflectivity as low as 10^{-3} is not sufficient to prevent parasitic lasing in a high power device.

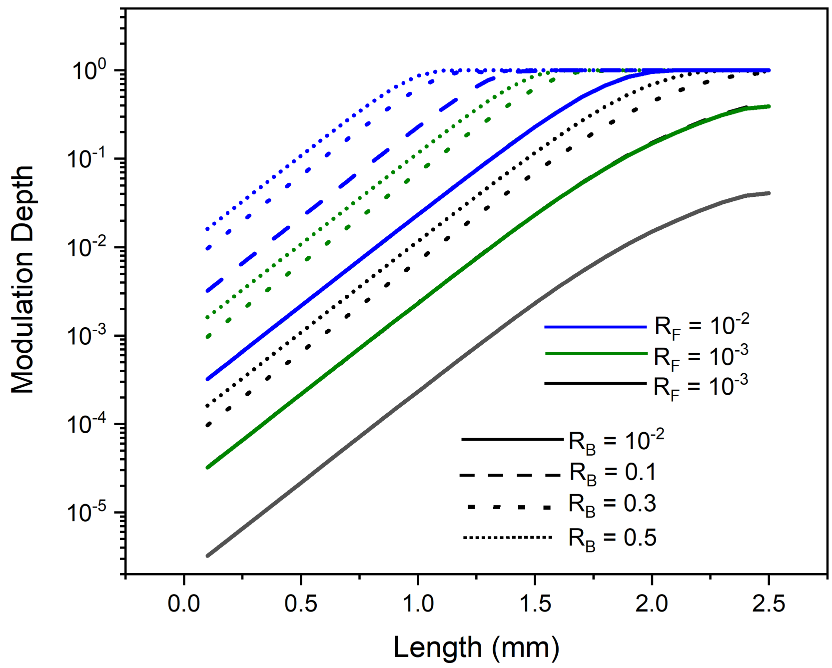

Figure 3.11: Modulation depth versus length for SLED devices with different facet reflectivities.

3.7 Quantum Well Variation

The epitaxial structure used in device fabrication decides the material gain, carrier confinement and optical confinement. The number of quantum wells in the structure is a very important factor for the performance of the device. Including a larger number of quantum wells in the structure increases the mode overlap with the active region, increasing the maximum gain which can be achieved. Fewer quantum wells allow for higher carrier densities to be achieved in the wells at lower driving currents which will decrease the transparency current density. Achieving the optimum balance between high gain and low threshold can be achieved by choosing the correct number of quantum wells. The gain curves for GaN devices with different numbers of quantum wells were simulated using the SiLENSe laser diode simulation package. This package simulates the bandgap, carrier density and electric field distribution for a given layer structure. For these simulations, identical current injection and cladding layers were used and the number of wells in the active region was changed between calculations.

The laser parameters used in these simulations are shown in Table 3.2. These parameters were chosen to simulate a SLED with low facet reflectivity. The software calculates the TE and TM modes in the waveguide as well as the mode overlap with the active region. These factors together with the carrier density in the active region and the waveguide loss allow for the net gain per well to be calculated by the program. This value is multiplied by the number of wells to give the total gain in the active region.

Table 3.2: Laser parameters used in simulation of GaN based laser diodes.

Parameter	Value (Units)
Waveguide length	1000 (μm)
Waveguide width	3 (μm)
Front facet reflectivity	0.01
Back facet reflectivity	0.01
Substrate thickness	300 (μm)

Figure 3.12 shows the evolution of gain with current density for different numbers of QWs. It is clear that reducing the waveguide loss would be highly advantageous. The gain increases at the fastest rate at low currents with diminishing returns as the current is increased further. A lower waveguide loss would allow for a significantly decreased transparency current density as well as greater amplification in the waveguide.

In the single QW device the gain overtakes the waveguide loss at a current density of 6 $kAcm^{-2}$. In the devices with more QWs the transparency is reached at higher current densities. The gain in the MQW devices increases more rapidly with current than in the SQW devices, providing the potential for much higher power.
Figure 3.13 shows simulated L-J characteristics for SLEDs with different numbers of QWs. As suggested by the gain curves, the SQW device is the first to reach transparency, with the efficiency decreasing as the gain saturates. The MQW devices increase rapidly with increasing current density above transparency. This suggests that devices with fewer QWs should be used in cases where the threshold for superluminescence in the material is high as very high current density would increase heating and possibly damage the metal contacts. For materials with relatively low transparency current densities and where there is a robust contact, MQWs should be chosen to maximise the output power.

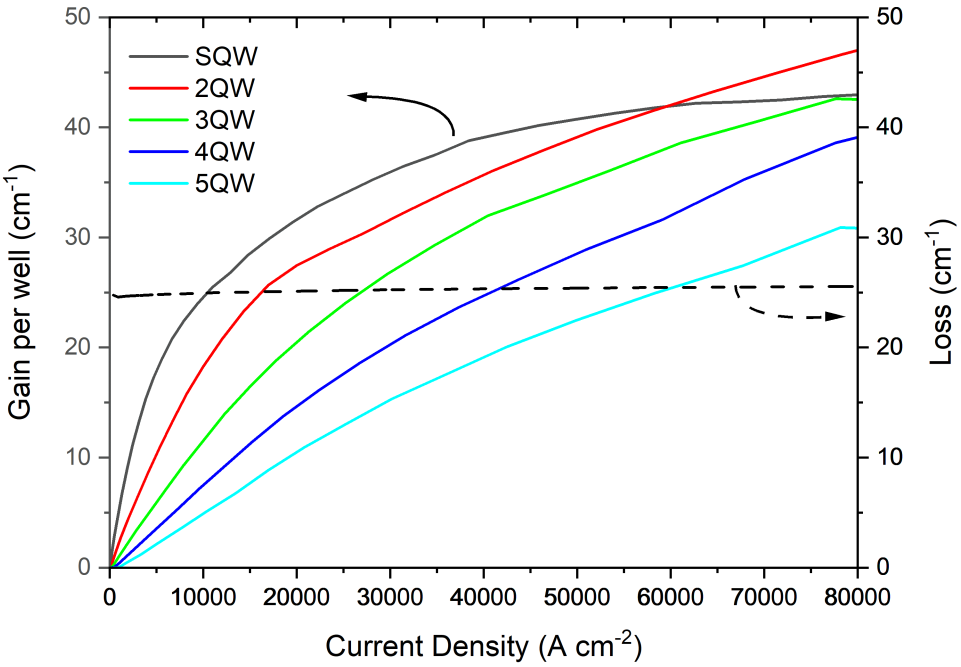

Figure 3.12: Simulated gain curves as a funciton of current density of GaN laser structures of with different numbers of QWs.

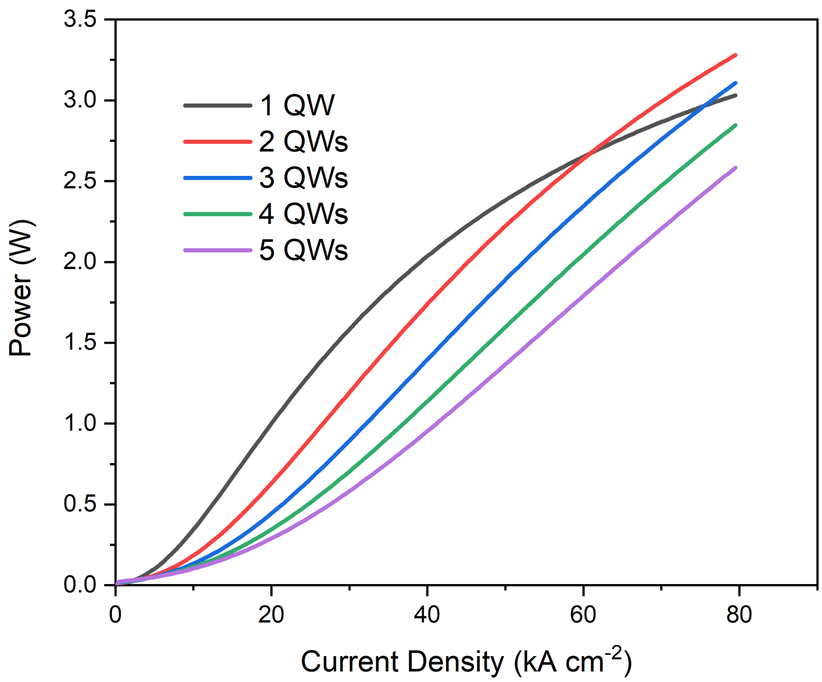

Figure 3.13: Simulated L-J curves of GaN SLEDs with different numbers of QWs.

3.8 Waveguide Loss

Equation 2.21 shows that the power in a SLED increases exponentially with the net gain, i.e. the modal gain Γg minus the loss α. In Figure 3.3, the loss is 25 cm^{-1}. The SLED enters the superluminescent regime when the gain overtakes the loss. If the loss could be reduced, superluminescence could be reached at a lower current density. Figure 3.14 shows simulated L-I characteristics of 1 mm long SLEDs with different levels of waveguide loss. As expected, decreasing the loss allows for higher optical power to be attained. Reducing the loss from 25 cm^{-1} to 10 cm^{-1} leads to an increase in optical power by a factor of 1.8. The gain appears to be saturating earlier in the devices with lower loss. This is due to the high photon density inducing recombinations and reducing the carrier density as discussed earlier in this chapter. In GaN SLEDs the loss can be reduced by reducing the Mg doping near the QWs. The extra holes in the p-type GaN can absorb photons, increasing the loss.

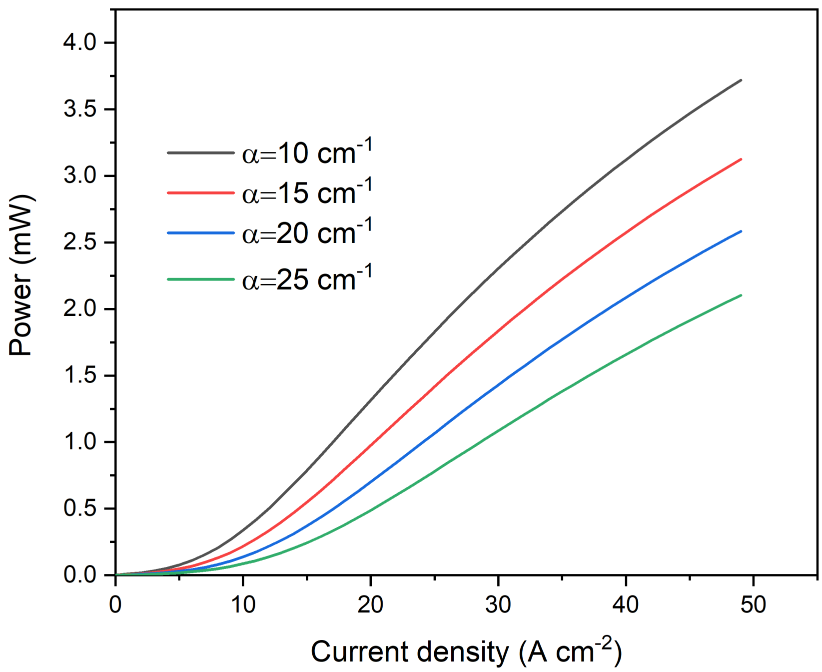

Figure 3.14: Simulated L-I characteristic of GaN SLEDs with different levels of waveguide loss.

3.9 Summary

In this chapter a model of the performance of SLEDs with different device geometries and epitaxial structures is presented. The model shows how the non-uniform distribution of the carrier density must be factored into the calculations for high power devices. A uniform carrier density model overestimates the increase in gain from increasing device length.
The trade-offs between increasing device power using length, facet reflectivity and epitaxial structure and maintaining a broad emission spectrum are discussed. The output facet reflectivity is found to be the crucial determinant of whether a broad, smooth spectrum is achieved. With sufficiently low front facet reflectivity, large optical powers can be produced without incurring a decrease in spectral quality. The facet reflectivity must be particularly low in high power devices, where a reflectivity as low as 0.1% can still result in significant modulations.
It is suggested that for devices with lower optical gain, steps can be taken to significantly increase power without needing to ensure very low reflectivity. For these devices a reflective back facet could be a useful method of boosting the optical power. For higher power devices such as GaN based SLEDs, extra steps may be needed to prevent parasitic lasing. For example an anti-reflection coating could be used as well as another feedback suppression method like a tilted facet.
The epitaxial structure is discussed. It is shown that devices with fewer QWs can achieve transparency at a lower current density than devices with more QWs. Devices with more QWs can achieve higher gain and may be useful in low threshold materials where contact resistivity is not an issue. Several quantum wells are recommended for GaAs and InP based SLEDs where as fewer QWs are recommended for GaN devices. Although using several QWs theoretically enables the highest power conversion efficiency, very high bias and current density are required to reach the regime where this occurs. For example in the simulations shown the 2QW GaN SLED becomes more efficient than the SQW device at an injection level of $50kAcm^{-2}$. Finding an Ohmic contact which can provide low enough contact resistivity to allow this level of injection without failure presents a difficult obstacle to realising such a device. Choosing the configuration which is most efficient up to 50 $kAcm^{-2}$ i.e using one or two QWs appears to be the most practical option for high power GaN SLEDs. The impact of waveguide loss on the output power is also discussed. It is shown that reducing this loss can allow for a reduction in the threshold for

superluminescence and boost optical power. This can be achieved by reducing the level of p-doping close to the active region.

The optimisation of ridge geometry is discussed. Increasing the width of the waveguide is shown to reduce transparency current density and provide higher optical power. However, the benefits of this are only seen when very high currents are applied. Also increasing the ridge width increases the risk of filamentation and non-uniformity in the lateral intensity distribution. For these reasons a narrow ridge appears to be the best choice for SLEDs.

Short cavity lengths appear to be a useful method of achieving high powers on GaN devices, providing a lower transparency current and reduced spectral modulations when compared with longer devices. Arraying shorter devices is suggested as an alternative to lengthening waveguides as a means to achieve higher optical peak powers from GaN SLEDs. The spacing and size of these arrays would need to be optimised however to find the best compromise of maintaining a small etendue and preventing overheating due to closely spaced ridges.

Chapter 4

Process Optimisation

4.1 Introduction

This chapter describes the fabrication of GaN surface emitting SLEDs. The crucial process steps are identified and described in detail.
As high current density is required to achieve population inversion and superluminescence, a high quality Ohmic p-contact with low resistivity is essential. Achieving such a contact to p-GaN has been the subject of intensive research for decades [78–80]. The difficulty in growing highly doped p-GaN layers provides a challenge to forming laser-quality ohmic contacts. Another challenge arises from the lack of metals or conducting oxides with a work function greater than that of p-type GaN [81]. Palladium was selected due to its high work function and usefulness as a hard mask.
The high current densities mentioned above also necessitate good heat spreading to alleviate the thermal load on the Pd p-contact. A thick electroplated gold contact was developed to improve heat dissipation. The design of these contacts was important as heat dissipation needed to be maximised while maintaining good optical and electrical performance.
Also crucial to the fabrication of these devices is the etching of a smooth 45° sidewall for the downward reflection of light through the substrate. This process requires knowledge and control of several factors including the resist profile, etch chemistry and selectivity as well as the need to consider the impact of other features such as the ridge waveguide on the mirror etch in the mask design. The development of this etch is explained below.

4.2 Wafer Structure

For superluminescence to be achieved, the modal gain in the waveguide material must exceed the loss. For this reason, the GaN epitaxial structures used for the fabrication of blue SLEDs were grown on bulk GaN substrates. Bulk GaN substrates provide better lattice matching with the GaN epitaxial layers grown on them than sapphire or silicon substrates. The reduction in lattice mismatch reduces the defect density in the material. Fewer defects means less non-radiative recombination and loss due to absorption, improving the net gain and overall efficiency of the device while simultaneously reducing the amount of heat generated during operation. The better quality growth enabled by using a bulk GaN substrate also improves the reliability of devices due to the reduction in defect density.

The epitaxial layers were laterally grown by metal organic vapour phase epitaxy (MOVPE) on the c-plane (0001) Sumitomo GaN substrate [30]. This growth method confines defects to high defect density 'lines' shown in Figure 4.7, while the regions in between have very high crystal quality. The devices are fabricated in these high quality regions.

The epitaxial structure is shown in Table 4.1. The laser waveguide structure was composed of two InGaN quantum wells separated by GaN barriers, a 1 μm thick n-type AlGaN bottom cladding layer and Mg doped AlGaN electron-blocking layer, a 100 nm thick p-type GaN waveguide layer and a 500 nm thick p-type AlGaN top cladding layer. A heavily p-doped GaN cap layer completes the structure.

Table 4.1: Wafer structure used for fabrication of blue SLEDs.

Layer	Thickness (nm)
p-GaN cap	50
p-AlGaN	500
p-GaN	60
p-AlGaN cladding	20
p-GaN	50
GaN EBL	50
GaN barrier	150
InGaN QW	-
n-GaN barrier	-
InGaN QW	-
n-GaN barrier	-
n-GaN	150
n-AlGaN cladding	1000
n-GaN	1000

4.3 A typical laser diode process

Figure 4.1 shows a typical GaN laser diode structure. The wafer structure is as described in the previous section with the cladding layers providing confinement in the transverse direction. A ridge waveguide confines the light in the lateral direction and two reflective etched facets at either end of the device create the Fabry-Perot cavity.
A p-contact on top of the etched ridge structure and n-metal on the conducting n-GaN substrate provide the contacts for electrical injection. The deposition of

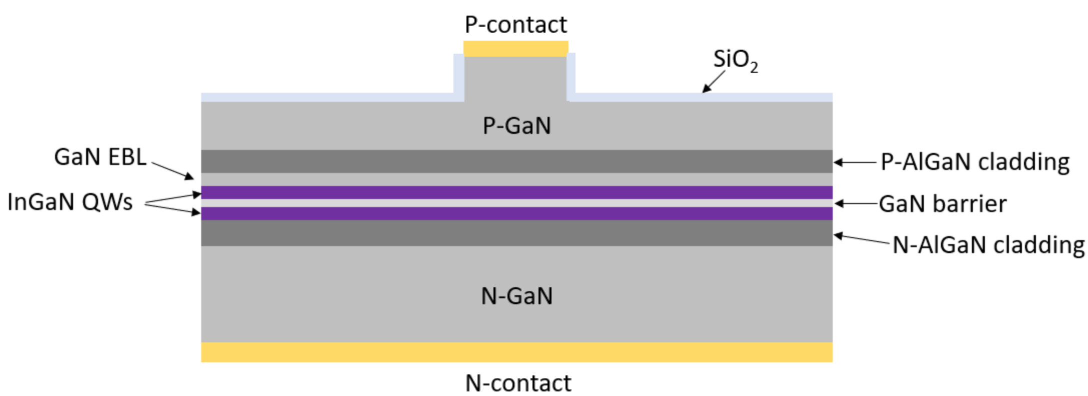

Figure 4.1: Cross section of GaN based laser diode.

this p-contact is the first step in a laser diode fabrication process. After the p-contact has been deposited the ridge structure is etched. As c-plane GaN is chemically inert this is done by ICP dry etching. The next step is to deposit an insulating oxide layer on to the surface of the chip. This is to prevent short circuiting after the bond pads are deposited. A window is opened in the oxide above the p-contact either by chemical wet etch or ICP etching. The bondpad is then deposited on top of the exposed contact and oxide layer. The bondpad is deposited to provide a larger electrical contact for wire-bonding during the packaging process.
Next the n-contact is deposited on the back surface of the chip by e-beam evaporation. The n-contact can alternatively be deposited on the top surface of the chip if the surface is etched down to the top of the n-GaN layer.
Finally the reflective facets must be formed. This can be achieved by cleaving the devices or by etching a vertical facet at either end and depositing high-reflectivity coatings on the facets.

4.4 SLED fabrication process flow

A surface emitting SLED fabrication process has several key requirements in order to produce a functioning and efficient device. While the fabrication process is similar to that of a laser diode there are some unique considerations which must be taken into account. The waveguide must be sufficiently long for amplified spontaneous emission to provide high powers, as the light does not undergo multiple round trips of the cavity a longer waveguide may be required to reach laser-like levels of optical power. The waveguide must also be narrow to confine the light in the lateral direction. The current injection area must be small enough to allow high current densities to be achieved easily. The high current density is required to cause the carrier population inversion needed for light amplification. The turning mirrors must have extremely smooth sidewalls so that beam quality is maintained during the reflection. If the sidewall is rough the light will be scattered and the directionality will be lost. Thick gold bondpads are required to make wire-bonding and probing the devices easier, but also to help dissipate this heat. A process flow was created to efficiently address all of these requirements. A brief outline of the process is described here with the steps described in more detail in this section.

4.4.1 P-contact deposition

The Pd p-contact is deposited by e-beam evaporation. A two level lift-off resist lithography is used to pattern the semiconductor surface. First a pre-exposed resist (PMGI SF11) is spun onto the surface of the semiconductor. This is cured at 170C before the imaging resist is spun on. The pattern is generated by exposing the imaging resist to UV light through a chrome and quartz mask. The pattern is developed using a resist remover chemical which removes the resist which has been exposed to UV light was well as any pre-exposed resist. The pre-exposed resist is developed quickly resulting in an undercut of the imaging resist.
After the patterning the sample is dipped in Aqua-Regia to remove any dirt or surface oxides which may be present. The Pd is then deposited and the samples placed in a solvent to remove the excess resist, leaving the patterned metal on the surface. The patterned metal defines the ridge of the SLED.

4.4.2 Ridge etch

In order to confine the light in the lateral direction, the ridge waveguide must be etched. The Pd pattern acts as a hard mask for this step so no alignment is required. The samples are etched by ICP in Cl_2 plasma with laser end point detection used to monitor the etch depth. The depth is confirmed using a profilometer after the etch is complete.

4.4.3 Pd wet etch

As the Pd acts as a mask and is quite resistant to ICP etching, the Pd at the ends of the waveguide must be removed to allow for the etching of the angled turning mirror. The sample is patterned with an imaging resist and dipped in Aqua Regia which removes the Pd from the exposed areas. Once the Pd has been completely removed from the desired areas the resist is removed with solvent.

4.4.4 Sloped mirror etch

The turning mirrors at the ends of the waveguide require a smooth, sloped profile to reflect the light downward through the transparent substrate. The ideal angle for this is 45 deg.

4.5 P-contact optimisation

It is crucial in a SLED that the p-contact is optimised to provide the lowest possible contact resistivity. Reducing the voltage required to drive current into the device will reduce the amount of heat generated and allow the device to operate at higher current densities or with longer pulse lengths. An ohmic contact is also essential for the most efficient delivery of current from metal to semiconductor. Initial attempts to form a contact to p-GaN laser material showed that the contact was non-Ohmic as deposited. The contact resistivity of the order of $10^{-2}\Omega cm^2$ was also much higher than required. For this reason additional steps had to be taken to optimise the Pd p-contact process on this material.

4.5.1 Circular Transmission Length Measurements (C-TLM)

The principle method used to characterise the quality of the Pd contact on GaN was the circular transmission length (C-TLM) method. This is a modified version of the linear transmission line measurement however it is a simpler test to perform as it requires only a single level of lithography where a linear TLM requires both metal deposition and etching of a mesa.
The linear TLM measurement was introduced by Shockley [82]. Through this method the specific contact resistance of a given contact could be calculated using the known distance between contacts and the resistance between the contacts. A disadvantage of this kind of structure can be the spreading of current between adjacent contacts due to current crowding. To address this issue the circular TLM structure was introduced [83]. The structure consists of a circular central electrode separated from the outer electrode by a concentric gap. A schematic of such a structure is shown in Figure 4.2.

For linear TLM structures the contact resistance is calculated by plotting the point to point resistance (R_{pp}) against the gap spacing between contacts. The intersection of the linear fit of the data with the resistance axis gives the contact resistance. The intersection of the fit with the distance axis provides the magnitude of the transfer length, a measure of the quality of the ohmic contact.
The specific resistance of a contact in a TLM structure is given by

$$\rho_c = R_{sh} L_T^2 \tag{4.1}$$

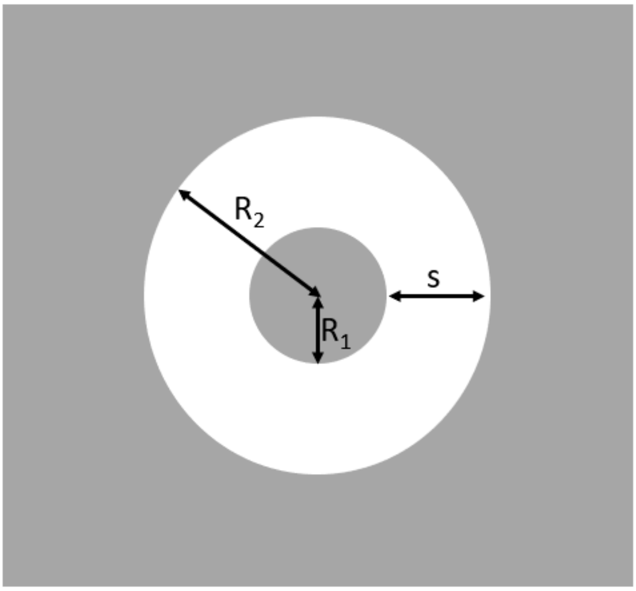

Figure 4.2: Schematic of a C-TLM feature. The grey indicates Pd deposited on the GaN surface which is indicated by white.

where R_{sh} is the sheet resistance and L_T is the transfer length. These are related to the measured point to point resistance by

$$R_{pp} = \frac{R_{sh}}{2\pi}[ln(\frac{R_2}{R_2 - s}) + L_T(\frac{1}{R_2 - s} + \frac{1}{R_2})] \tag{4.2}$$

Under the condition that $R_2 = R_1 + s$ the ln term in Equation 4.2 can be evaluated using a Taylor expansion. This allows the equation to be rewritten as

$$R_{pp} = \frac{R_2}{2\pi R_1}[s + L_T]c \tag{4.3}$$

where c is the correction factor

$$c = \frac{R_1}{s}ln(\frac{R_1 + s}{R_1}) \tag{4.4}$$

For circular TLM features the correction factor must be applied to each R_{pp} value [83]. This provides a linear data set from which the contact resistance and transfer length can be extracted in the same way as with a linear TLM.

4.5.2 Surface preparation

In order to achieve a good ohmic contact between metal and semiconductor the wafer surface must be cleaned before the metal is deposited. Initial tests on the high quality GaN wafers used for laser fabrication showed that the Pd contact had a higher resistivity than on GaN LED material on a sapphire substrate. As the evaporation conditions for both samples were identical, the surface preparation was suggested as the potential reason for the difference in resistivity. Another factor could be differing levels of doping between the two wafers.

During the epitaxial growth of GaN, there is a tendency for carbon and oxides to form on the surface of the p-type material [84]. This can act as a barrier to hole transport and increase the p-contact resistivity.

For this reason the GaN LED samples were cleaned in KOH prior to loading into the e-beam evaporator. KOH has been shown to be effective in removing C from the surface of GaN wafers. It can also etch facets presented by threading dislocations to present a "new surface" with a lower threading defect density [85, 86]. The laser material however was not cleaned in this way as KOH attacks n-face GaN and would damage the back surface of the wafer. A test was run to find the impact of KOH cleaning on contact resistivity on the laser material. Two identical samples of free-standing GaN were used in this test. The cleaning process was:

- 5 minutes in SiO_2 etchant
- 1 minute flowing DI water rinse
- 5 minutes in HCl
- 1 minute flowing DI water rinse
- 30 seconds in KOH at 100°C
- 30 seconds in DI water
- 1 minute flowing DI water rinse

The KOH step was skipped for one of the samples. A 40 nm layer of Pd was then deposited onto the surface of the samples by e-beam evaporation. C-TLM test sites were used to check the contact resistivity and sheet resistance of the Pd. Figure 4.3 shows that the sample cleaned with KOH provides an ohmic contact with much lower resistance than the sample which was not cleaned with KOH. The sample which was not cleaned in KOH does not provide an Ohmic contact. These measurements were taken using a Keithley 2400 sourcemeter which is accurate to within 0.12% in this range.

The samples were inspected using an optical microscope before and after cleaning. The KOH clean has a visible impact on the surface, with stains and dirt removed after the KOH dip. Figure 4.3 shows the surface of a GaN laser wafer before and after the KOH cleaning step. It is clear that the KOH step is effective in removing foreign contaminants arising from the dicing process from the wafer surface.

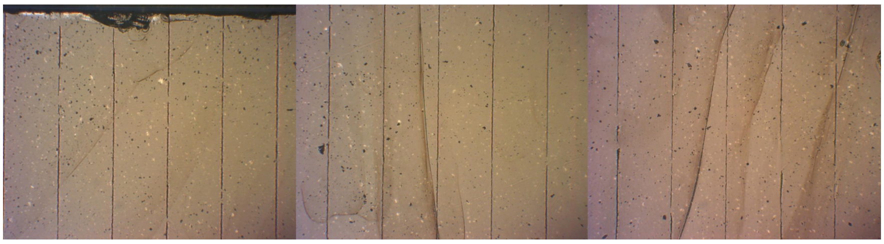

(a)

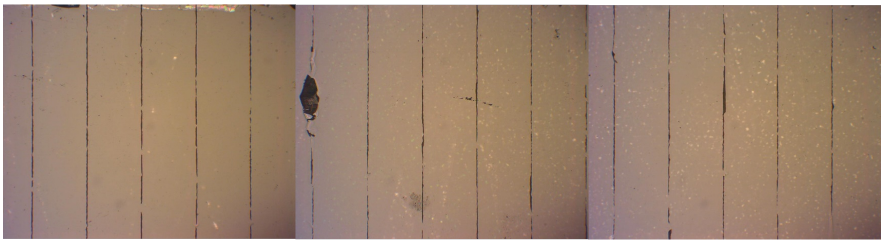

(b)

Figure 4.3: Surface of GaN laser wafer (a) before and (b) after KOH cleaning step in three different locations on the wafer.

It is clear that a large contribution to the total point to point resistance on the sample that was not cleaned comes from the contact resistance rather than sheet resistance as there is very little change in point to point resistance with decreasing feature size. If the sheet resistance is dominant and the contact resistance is low the expected result is for the point to point resistance to decrease with decreasing feature size as is observed on the sample which is cleaned with KOH before the metal is deposited. This difference is most likely due to the removal of C and native oxides from the surface of the material by KOH allowing for a better metal-semiconductor contact [87]. From these results it was decided that the KOH cleaning step is essential to achieving a quality ohmic contact with low resistance.

4.5.3 Annealing

It was observed in early attempts at fabricating devices that annealing the devices at 300°C for five minutes in Nitrogen ambient gas improved the

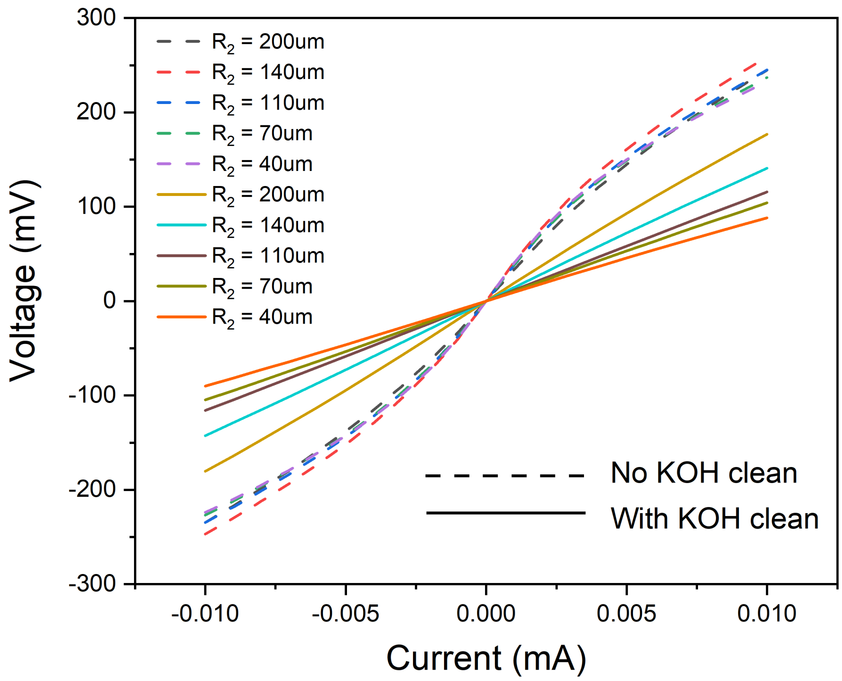

Figure 4.4: Comparison of circular TLM measurements for Pd deposited on GaN laser wafer with and without KOH cleaning. The inner contact radius for all sites was 25 μm, the outer radius R_2 is indicated in the legend.

p-contact characteristics. This may be due to the formation of $AlPd_2$ and $GaPd_2$ phases at the interface between metal and semiconductor [88, 89].

These annealed contacts were on surfaces which had not been cleaned with KOH prior to the Pd evaporation. To find the ideal conditions for annealing, the improved KOH cleaned samples a series of anneals were performed with different conditions.

Earlier work in this group showed that annealing Pd at temperatures greater than 600°C can damage the contact while annealing at temperatures lower than 300°C has little effect. For this reason the three temperatures used in the annealing trials were 300°C, 400°C and 500°C. All samples were annealed in N_2 ambient gas.

The samples were prepared according to the steps outlined in section 4.2.1, including the KOH clean. Figure 4.5 shows the C-TLM data for each of the samples. The correction factor has been applied to the data to provide a linear data set from which the contact resistance and transfer length could be calculated. Table 4.2 shows the correction factors used for each gap spacing.

Table 4.2: Linear correction factors for different gap spacings (s) for C-TLM measurements.

Gap length (μm)	Correction factor
175	0.501359
115	0.519097
85	0.584866
45	0.713171
15	0.874548

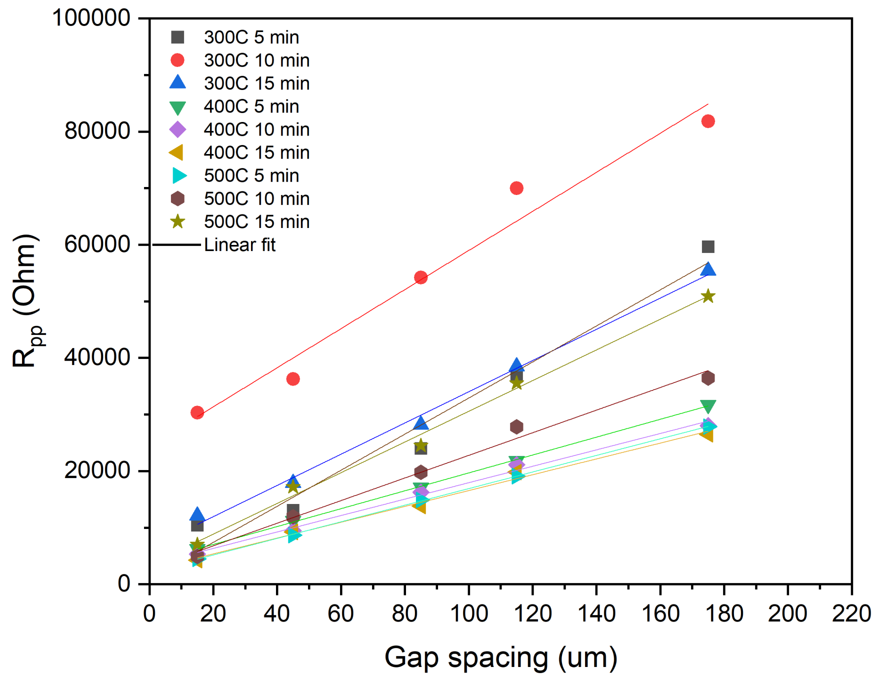

Figure 4.5: C-TLM data for GaN laser samples with Pd annealed for different times at different temperatures. Linear correction factor has been applied to the data.

Initial measurements showed differing levels of sheet resistance between the samples. It was noticed that the high defect density lines in the material had a significant effect on the R_{pp}. This is why the increased slope comes into effect at high gap spacings on some chips. If a high defect density line ran through the gap as shown in Figure 4.7, the R_{pp} is greatly increased. This is much more likely to occur at a feature with a larger gap spacing. This may explain the apparent difference in sheet resistance between the measurements shown in Figure 4.5. The slopes look similar for all measurements at small gap spacing with the apparent sheet resistance difference only evident as gap spacing increases.

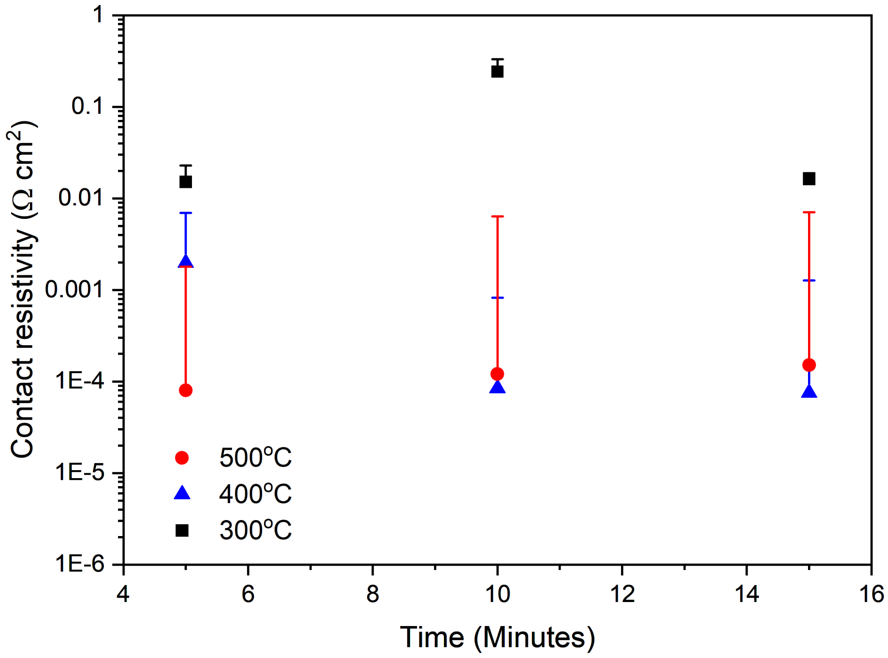

Figure 4.6: Contact resistivity of Pd contact on samples with different anneal temperatures.

Taking care to measure only features without defect lines running through the gap spacing, the sheet resistance is consistently $2.5 \times 10^4\ \Omega$ on all samples. This suggests that anneal does not affect the properties of the p-GaN itself, rather the interface between the Pd and p-GaN.
The annealing does have an effect on the contact resistance particularly at 400C and 500C. The lowest contact resistivity was achieved on the sample which was annealed at 500C for five minutes. On this sample the point to point resistance measured at the site with 15 μm gap spacing was 2228 Ω. Resistances of this magnitude were also achieved with the 500C anneal for ten minutes and fifteen minutes as well as with all of the 400C anneals.
The 300C anneals did not provide the same low contact resistivity as the higher temperatures. This may have been due to it being insufficiently hot to promote the formation of a thermal nitride at the interface. The ten minute anneal at 300C provided particularly high contact resistance when compared with the other results. This may be due to a poor lift-off or cleaning of the area on which the contact is deposited.
The chips were inspected under an optical microscope after the anneal process. There was no visible evidence that the anneal had damaged the contact or impacted on the surface of the metal. The patterns remained well

defined during the anneal.

Figure 4.6 indicates the high level of error in the contact resistivity measurement. This level of error makes it difficult to determine which anneal truly provided the lowest resistivity, however it is clear that the 300°C anneal provides the highest resistivity. The margin of error also appears lowest for the 400°C anneal suggesting that it is a more reliable result and more likely to provide low resistivity than the 500°C anneal. The 400°C anneal is also preferred as there is a lower risk of damage to the material when a lower temperature is used. The fabrication of LEDs using each of these anneals would help to give a better indication of which anneal conditions provide the best contact.

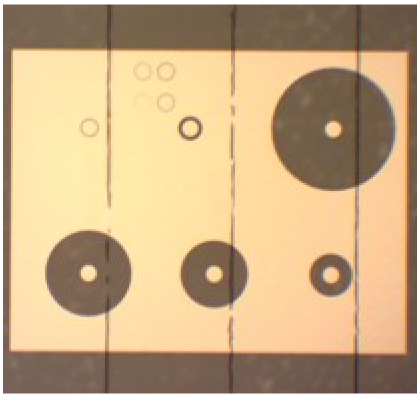

Figure 4.7: C-TLM site with high defect density lines. The position of these lines affects the sheet resistance measurement at different positions.

4.5.4 Post-processing annealing

Some devices which were fabricated before the p-contact optimisation were annealed in an attempt to improve the I-V characteristics. The devices were annealed in N_2 at 400C for five minutes as these were the conditions which provided the lowest contact resistivity. The results shown in Figure 4.8 show that the anneal post-processing significantly reduced the operating voltage of the devices.
Another explanation could be that the later devices were fabricated on a wafer with a lower level of p-doping. This was an attempt to reduce losses in the waveguide due to absorption by magnesium dopants in the cladding layer [90]. While the lower level of doping may help to reduce waveguide

losses it results in a more resistive path to the active region for injected holes through the p-side.

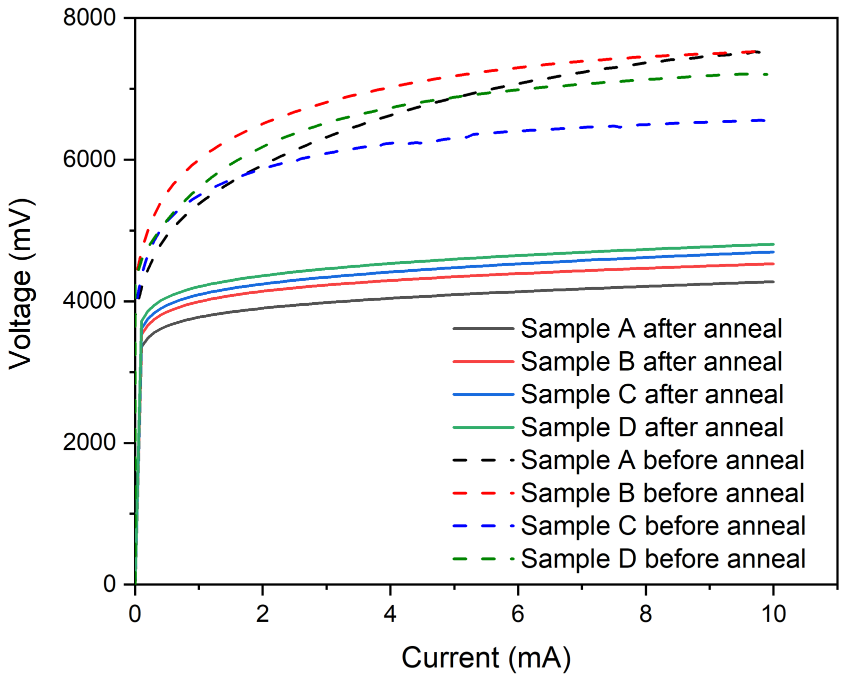

Figure 4.8: I-V characteristics of four 1 mm SLED samples before and after a 400°C anneal.

4.5.5 Pd hard mask etching

The ridge etch step in the GaN SLED fabrication process involves using the Pd contact metal as a hard mask. This simplifies the processing and improves accuracy as it is a self-aligned process. There is potential however for the ICP etching process to damage the Pd contact. The effects of the etch on the Pd contact were investigated by fabricating LED devices on a GaN on Si wafer. Both samples were cleaned identically and had the p-metal deposited in the same evaporation. One sample was then etched with Cl_2 to a depth of 500 nm to replicate the effects of the ridge etch. Both samples were then etched to a depth of 900nm to form the mesa and a Ti/Al/Ti/Au n-metal contact was deposited. The electrical characteristics of both sets of devices were measured and are compared in Figure 4.9.

The LEDs devices with contacts which were exposed to the ICP etch display a slower turn on at low current. At higher currents however the behaviour of

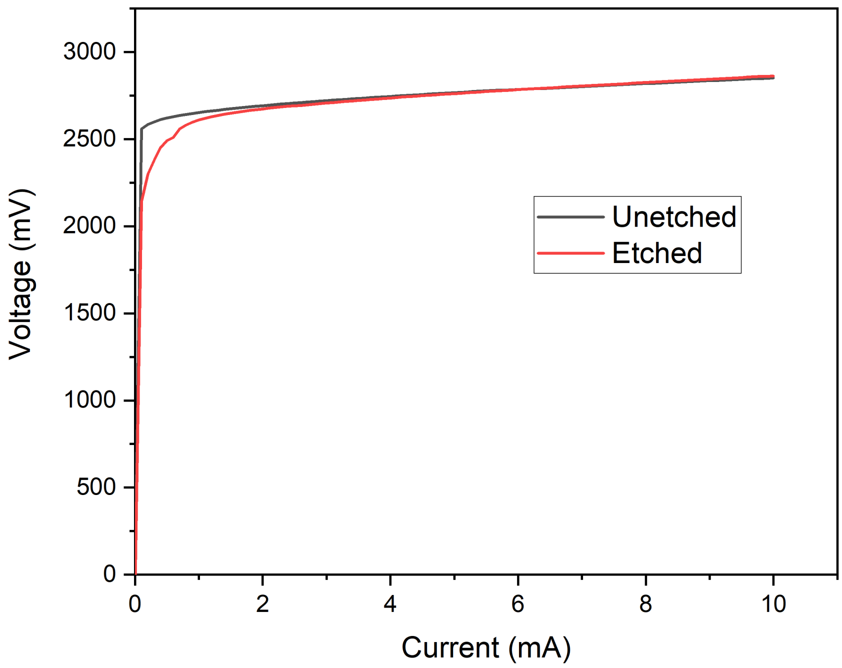

Figure 4.9: Comparison of I-V characteristics of LED samples with contacts etched by Cl_2 and samples with unetched contacts.

these devices is identical to the devices with contacts which were not etched by Cl_2. Log IV measurements were taken to compare the low current characteristics more closely. These results are shown in Figure 4.9.

An observation taken from SEM images after the Pd hard mask etch was the presence of some residue on the surface of the Pd which is shown in Figure 4.10.

This residue had a polymer-like appearance and could be easily removed using 1165 photoresist remover. It was suspected that this residue was $PdCl_2$, a polymer which can form at high temperatures. This did not have an impact on the contact resistivity however a cleaning step comprising a dip in the photoresist removal solvent 1165 was introduced to remove the residue to prevent any interference with later processing steps.

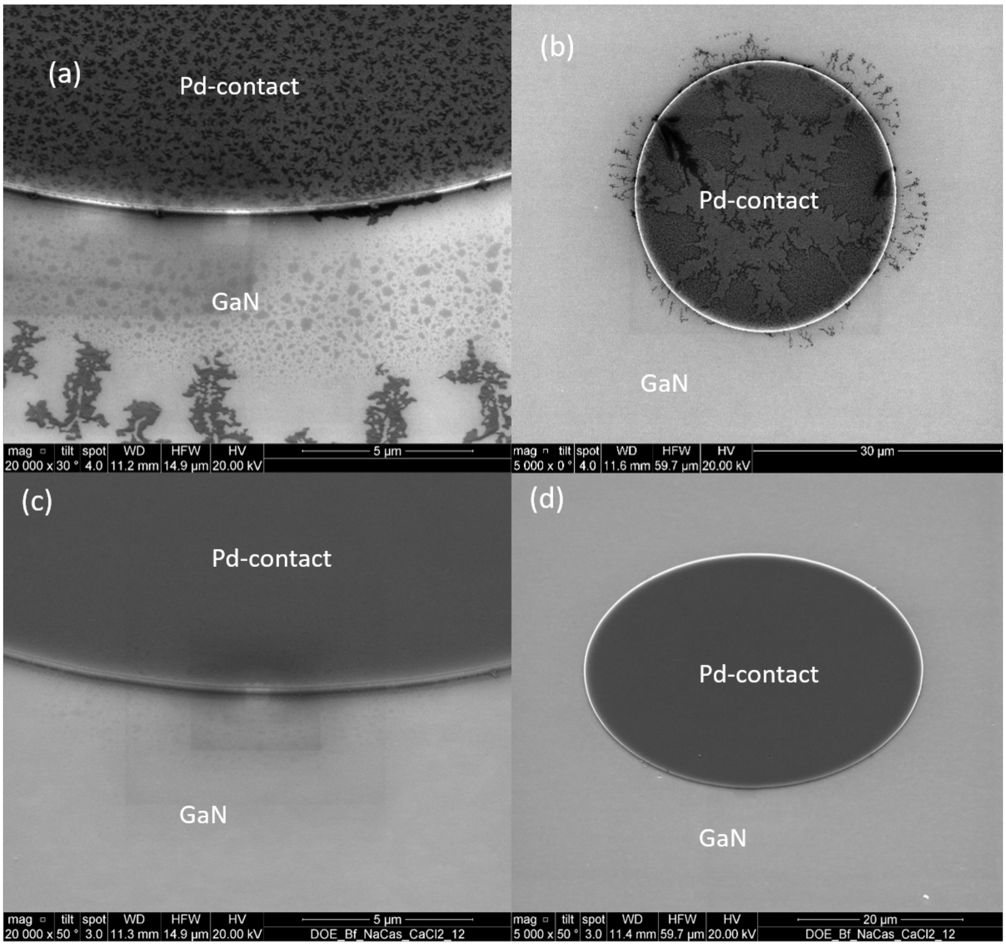

Figure 4.10: SEM images of Pd contacts on GaN after Pd hard mask ICP etch. The images (a) and (b) show the contacts with residue before the solvent clean. (c) and (d) show the contacts after the solvent clean which removed the residue.

4.6 Sloped mirror etch

The sloped mirror etch is an important step in the fabrication process of surface emitting SLEDs. A smooth sidewall is required to prevent scattering and preserve beam quality, while an angle close to 45° is desirable. Light incident at 45 ° will be reflected at the same angle, providing a 90 ° turn with the light travelling normal to the substrate. It is important that the light is incident on the back surface at an angle less than the critical angle for efficient extraction. The critical angle for a GaN/Air interface is 25°. Light striking the back surface at an angle greater than the critical angle will be reflected and trapped inside the chip.

4.6.1 Resist profile modelling

Resist reflow was the technique used to achieve a sloped profile for the mirror etch. This technique involves heating the photoresist above its melting point after patterning. When the resist enters the liquid phase, surface tension effects cause the rounding of sharp corners and sloping of vertical walls as the surface energy moves towards a minimum. This process is governed by Young's equation [91]

$$\sigma_{gs} = \sigma_{ls} + \sigma_{lg}Cos(\Theta) \tag{4.5}$$

and the Young-Dupre equation:

$$W_{asl} = \sigma_{lg}(Cos(\Theta) - 1) \tag{4.6}$$

Where $\sigma_{gs}, \sigma_{ls}, \sigma_{lg}$ are the gas-solid, liquid-solid and liquid-gas interfacial surface tensions respectively, Θ is the contact angle as illustrated in Figure 4.11 and W_{asl} is the wetting parameter, a measure of how well the liquid adheres to the solid surface. A higher degree of wetting will mean a larger interfacial surface area between liquid and solid.

Equations 4.5 and 4.6 describe how a liquid will interact with a solid at the interface. The surface of the liquid droplet itself is described by the Young-Laplace equation:

$$\Delta p = -\gamma(\frac{1}{R_1} + \frac{1}{R_2}) \tag{4.7}$$

Where Δp is the difference in outward and inward pressure at a across the interface of the droplet, γ is the surface tension and R_1 and R_2 are the principal radii of curvature of the droplet.

Thermally driven polymer reflow is a dynamic process dependent on the viscosity of the droplet. The energetic imbalances between at the interfaces between liquid solid and gas drive a creep process which eventually leads to the elimination of sharp corners and wetting of the substrate. Over time the liquid-solid interfacial surface area and surface area of the droplet itself will move toward the minimal energy state described by equations 4.5, 4.6 and 4.7.

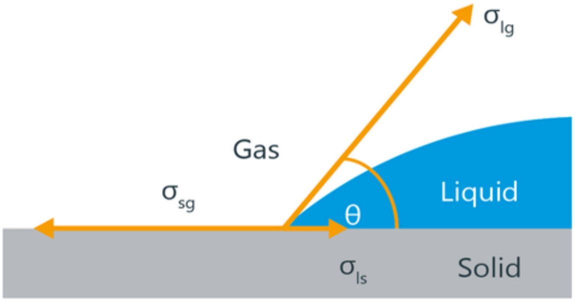

Figure 4.11: Schematic showing liquid droplet on solid surface.

ICP etching of GaN samples with Shipley 1828 resist showed 1:1 selectivity between the resist and GaN. This was achieved by tuning the platen power which influences the velocity at which the etching ions strike the semiconductor surface. This meant that the profile of the GaN would be wholly dependent on the profile of the photoresist. An example of this effect is shown in Figure 4.12 where the photoresist profile is transferred directly on the GaN sample. Figure 4.12 (b) shows that any lines or wrinkles in the resist pattern will also be transferred into the GaN sidewall. It was clear that controlling the resist profile would be crucial to achieving a smooth 45° etch.

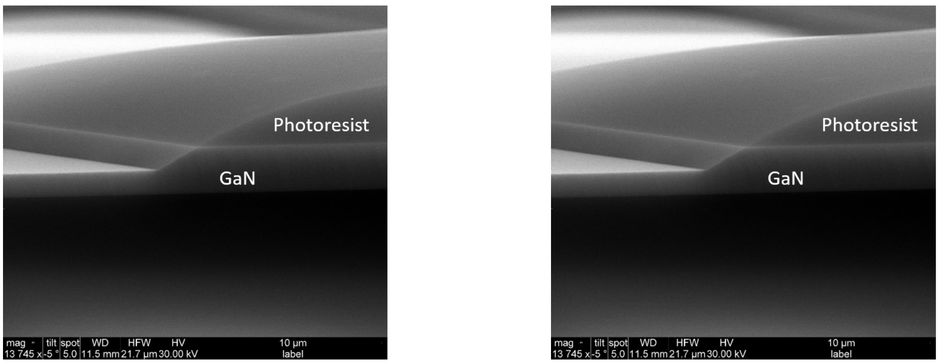

Figure 4.12: SEM images of 4.5μm thick Shipley 1828 photoresist on GaN surface after ICP etching in BCl_3 chemistry. (a) shows a cross section of a cleaved GaN samples with photoresist on top. The etched GaN sidewall follows the sloped profile provided by the photoresist. (b) shows an etched feature where a wrinkle in the resist has been transferred onto the GaN sidewall during the etch.

It was observed from previous fabrication trials that the sidewall angle on reflown resist was not constant across all patterns and surfaces. Smaller circular features such as μLEDs were observed to have steeper sidewall slopes than larger patterns. Patterns with sharp corners such as squares and rectangles had steeper sloped sidewalls near the corners. Also the same shaped pattern could provide a different sidewall angle depending on whether the pattern was a hole surrounded by resist or a small patterned piece of resist on an otherwise bare surface. With all of these metrics to consider it became difficult to predict the sidewall angle that would result from a given pattern.

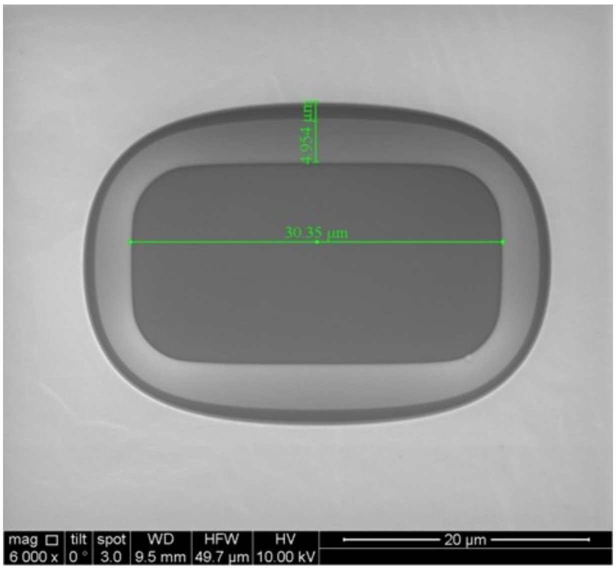

Figure 4.13: SEM top view image of rectangular mirror trench etched in GaN. The dark colour is the bottom of the trench while the lighter colour is the p-GaN surface. The depth of the etch is 4.6μm The sloped sidewalls are steeper at the corners and become more shallow further from the corner.

The Surface Evolver [92] software package was used to simulate the effects of surface tension on 3D objects. The soap-film model takes a given shape and allows for the calculation of the minimum energy shape of the initial object. Studies on photoresist reflow have previously been carried out using Surface Evolver for micro-lens pattern optimisation [93]. Here, the program is used to better anticipate the effect of photoresist reflow on the patterns used for SLED mirror etches.

The simulations were based on the mound example given in the Surface Evolver manual [94]. The surface energies of the photoresist and semiconductor surface and contact angle are used to calculate the interfacial energy between the liquid and solid. Over each iteration the energy of the shape is moved closer to the minimum until convergence is reached. The simulation was performed for substrate surface energies. The rest of this section will present the results of these simulations.

Several different photoresist patterns were used in these simulations to analyse the effects of reflow on patterns that could be used to fabricate μLEDs and SLED mirror trenches. The mesh was created using the Surface Evolver

Table 4.3: Surface energy values used in Surface Evolver simulations of resist reflow.

Material	Surface Energy (mJm^{-2})
GaN	2400 [95]
GaAs	860 [96]
SiO_2	38 [97]
Photoresist 1813	33 [93]
Photoresist AZ4562	50 [98]

and the surfaces were assigned surface energy values obtained from literature. These values are shown in Table 4.3.

The size of the mesh elements is important to consider, as larger mesh elements will be greatly changed after each iteration, while finer elements will converge to equilibrium more slowly. To simulate the 'creep' of photoresist, a relatively slow process, a fine mesh was used. The simulations were run until a converge condition was met whereby the overall surface energy changing by less than 0.01% between iterations ended the simulation.

(a) *(b)*

Figure 4.14: Surface Evolver models of disc shaped photoresist pattern sitting on GaN (a) before and (b) after thermal reflow. The initial thickness of the resist is 4μm with a diameter of 20μm

The first pattern analysed was a simple disc shape. This pattern could be used in the fabrication of micro-lenses or μLEDs to provide a parabolic profile. The slope was measured by using the Surface Evolver's clip feature which allows of a cross section of the pattern to be viewed. An example of the evolution of this pattern is shown in Figure 4.14. The shape of the pattern does not change after a number of iterations, indicating that after a certain amount of time the reflow stops as the resist has reached its minimum energy state. Increasing the temperature could allow for further reflow by decreasing the viscosity of the resist.

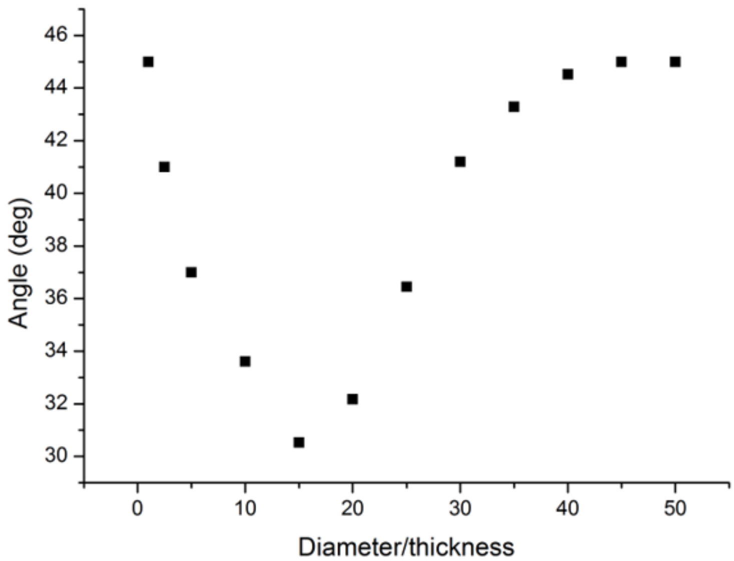

Figure 4.15: Sidewall angle of disc shaped pattern after reflow with changing ratio of photoresist thickness to feature size.

The results of the simulations show that the ratio of resist thickness to the size of the pattern is a key determinant in the sidewall slope. The slope is steep when the resist thickness is large relative to the feature size. As the feature size is increased or thickness is reduced, the slope begins to decrease. Increasing the feature size to thickness ratio further, the sidewall slope begins to increase again and eventually levels out. This is because for larger features the bulk of the resist is not significantly affected by surface tension effects as it is already at minimum energy. Only the sharp corners near the edge of shape are affected with the rest of the photoresist remaining relatively stationary throughout the reflow process. For the shapes with lower feature size to thickness ratios, the entire pattern is affected by the reflow process as the height of the initially vertical sidewall, which becomes parabolic during reflow, represents a greater percentage of the shape's surface area than it would on a larger feature.
Square shaped features were also studied as part of these simulations. It was noticed from experimental results that thermal reflow could have result in the rounding of sharp corners and bowing of straight lines. This effect did was not consistent across all shapes however, impacting smaller features more significantly than larger features. The relative change in surface area was used to measure how the reflow affected each pattern. Figure 4.16 shows how a

square shape with sharp corners is impacted by resist reflow. The relative change in pattern area is shown in Figure 4.17. It is clear that smaller features are more significantly affected by reflow and that this needs to be accounted for in the mask design.

Figure 4.16: Top view of original square mask pattern (red) superimposed on shape after reflow (grey).

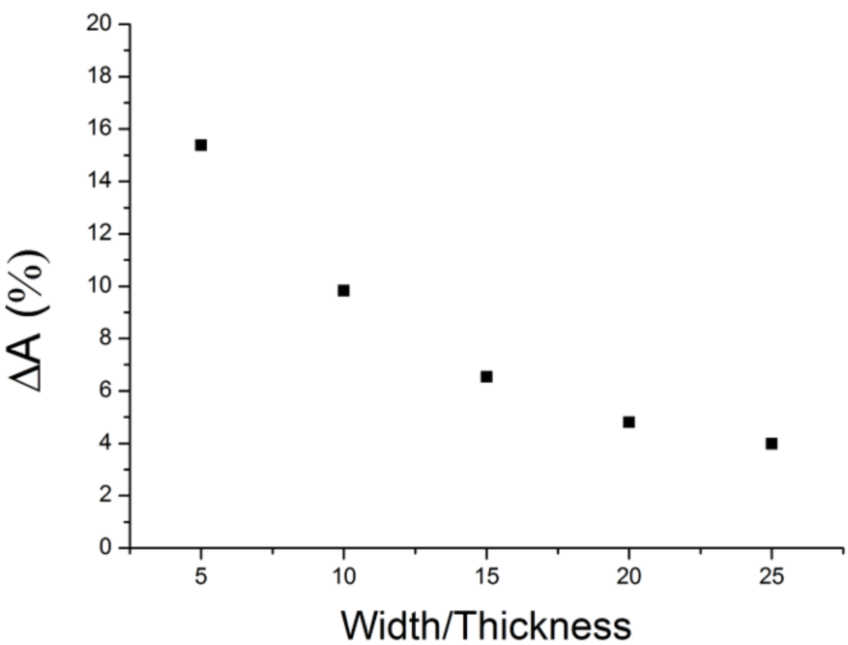

Figure 4.17: Percentage increase in photoresist pattern area on GaN surface after reflow versus feature size/thickness ratio.

Reflow also affects trenches or openings in bulk resist. As this is the type of feature required for the sloped mirror etch, these features were also modelled. The simulations showed that the steepest slope was at the corners of the rectangular trench while the angle was less steep along the sidewalls. The angle decreased with distance from the corner. This is can be seen in the SEM image of a trench in Figure 4.13. The length of the sloped sidewall is shorter closer to the corners of the feature, indicating a more vertical slope. Figure 4.18 shows a comparison of the simulation with an SEM image of a mirror etch. The change in angle with distance from the corner in the simulation shows good agreement with the SEM measurement. This is shown in Figure 4.18.

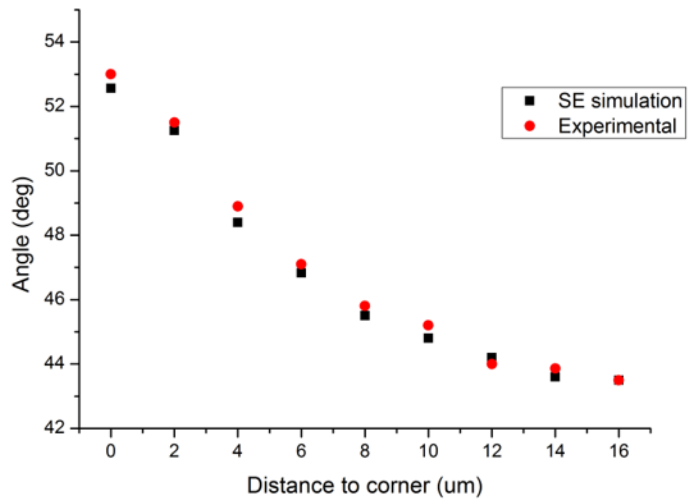

Figure 4.18: Comparison slope angle versus distance to corner of reflown resist in rectangular trench pattern for simulated reflow and experimental measurement.

As the angle becomes constant further from the corner, mirror trenches with long sidewalls were chosen in the final mask design. This improved the alignment tolerance and provided a long section of sidewall with a constant angle. This helped to improve the beam quality of the devices.
The choice of photoresist was another important consideration in the mirror etch process. The surface energy of the photoresist would partially determine the final shape of a feature after reflow. Surface Evolver simulations were used to simulate two resists: Shipley S1828 and MicroChem AZ4562. The simulations showed that after reflow the shipley resist produced a pattern closer to the original than the AZ series resist. The higher surface energy of the AZ series resulted in pronounced rounding at the corned of the rectangular trench. This result was observed experimentally and is shown in Figure 4.19.

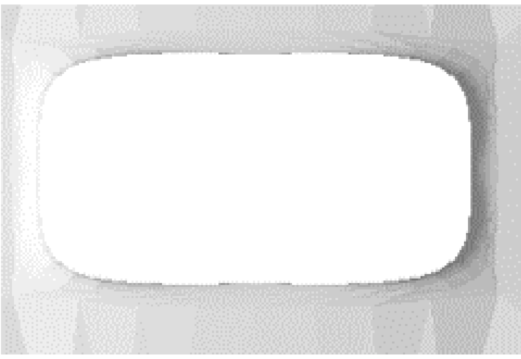

(a)

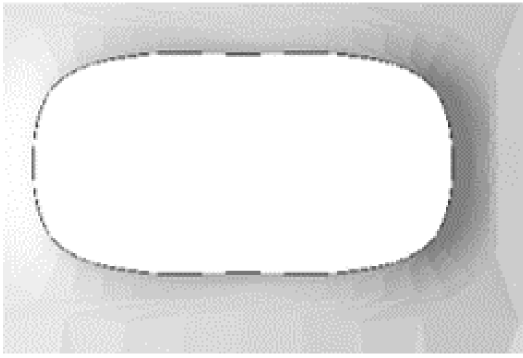

(b)

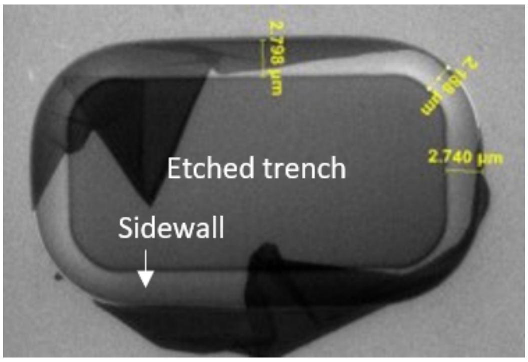

(c)

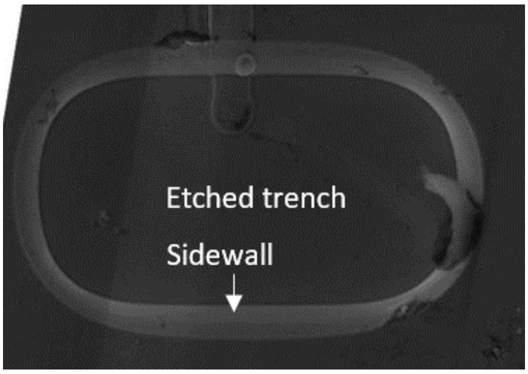

(d)

Figure 4.19: Results of Surface Evolver simulated reflow of rectangular trench opening in (a) Shipley 1828 and (b) AZ4562 photoresists and SEM images of rectangular trenches with sloped sidewalls etched using reflown (c) Shipley 1828 and (d) AZ4562 as the mask. The resist thickness in both cases was 4.5μm.

4.6.2 Sloped etch for GaN devices

Using the results from shown in the last section, the patterns for the etch trenches were designed. With the shape of the trench being determined by the photoresist the next step was to achieve a smooth GaN sidewall. A BCl_3 chemistry was chosen for the etch as it has been shown to provide smooth sidewall features in high temperature GaN ICP etches [99].

GaN test samples were loaded with different shapes patterned in photoresist on the surface. The platen power and coil power were varied to find the optimum etch. The combination of 800 W coil power with 100 W ICP power provided 1:1 selectivity between Shipley S1813 photoresist and the underlying GaN. As the reflown resist provided a 43.5° sidewall, this was transferred onto the material, giving a smooth sidewall with a 43.5° slope. Sidewall angles were measured using a profilometer and also by using SEM imaging. With the depth of the etch known, the slope could be calculated using lateral length of

the slope from a top view SEM image.
Figure 4.20 shows several features etched using the BCl_3 ICP etch. The reflown photoresist is seen on top of the GaN surface, providing the sloped sidewall profile. The pattern in Figure 4.20 (a) shows how the sidewall slope varies depending on the distance to the corner of a right angled feature. It also shows how the slope differs between concave and convex corners. The convex corners have a less steep slope as surface tension effects pull the photoresist at the corners back into the bulk of the resist in these areas. This effect does not occur at the concave corners as the forces pulling the resist back into the bulk are balanced by those pulling outward from the nearby sidewalls. Figure 4.20 (a) illustrates this phenomenon.

Figure 4.20 (b) shows the end of a rectangular trench. It shows that elongating the long side of the shape gives a consistent sidewall slope far from the corner. Figure 4.20 (c) shows features with different radii. As predicted by the resist modelling, the sidewall angle is different for different sized features. The effects on square features which were described in the previous section can also be seen in Figure 4.20 (d) where the smaller square feature has become rounded by reflow, now resembling a circle.
Increasing the RF power appeared to increase the etch rate without influencing the selectivity. This is because the RF power affects the velocity of the ions in the chamber, not the density of the plasma itself.
The ICP did have some impact on the selectivity, with higher density plasmas etching the GaN more preferentially.

4.7 Bondpad electroplating

With a very narrow p-contact on top of the ridge, bondpads are required to allow for probing and wire bonding of the devices. These bondpads serve as a larger area for bonding and probing, with an insulating oxide layer preventing them from forming a short circuit on the side of the ridge. The bondpads also improve the reliability of the devices by spreading the heat generated at the contact over a larger area. A schematic showing the configuration of the bondpads is shown in Figure 4.21.
The bondpads can be either be deposited by e-beam evaporation or by electroplating. The plating process involves the evaporation of a seed metal layer to provide a conductive surface for the electroplating. In this case Cr:Au

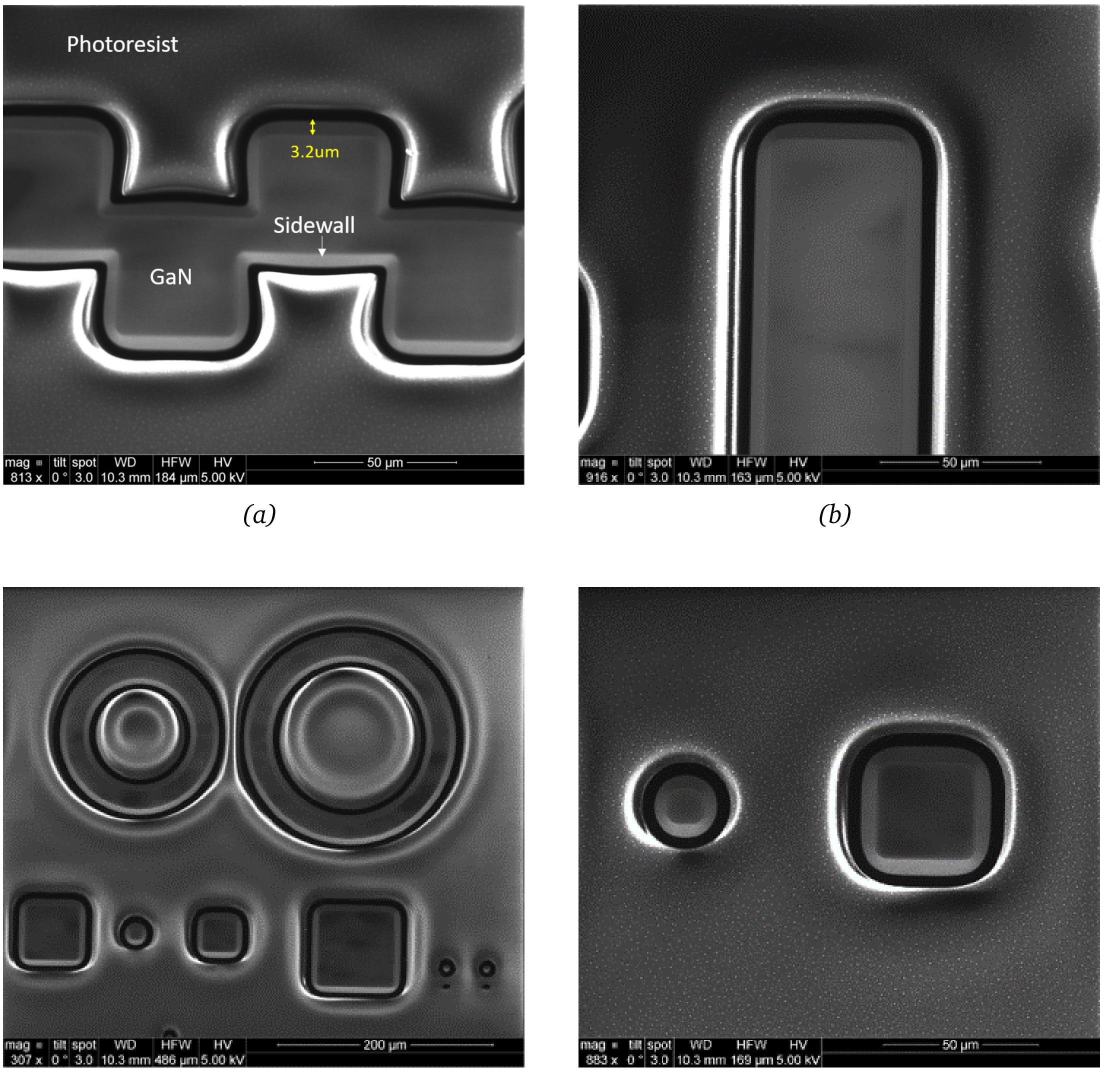

(a) *(b)* *(c)* *(d)*

Figure 4.20: SEM images of various patterns etched into GaN by ICP etch. Photoresist is visible on top of the GaN surface.

is chosen for good adhesion to SiO_2. The sample is then patterned with thick photoresist and placed in a solution containing Au ions. An electric field is applied between an anode and the sample, causing the ions to move onto the chip and building a thick Au coating in the resist openings. The seed metal is removed afterwards with commercial chemical etchants to isolate the devices. Testing of GaN based laser diodes with both plated and evaporated bondpads showed that the devices with plated bondpads were capable of withstanding much higher currents without failing. This is due to the thickness of the plated contacts. The plated bondpads were several microns thick while the evaporated bondpads were in the order of hundreds of nanometers thick. This extra thickness allowed for much better heat dissipation in the devices with

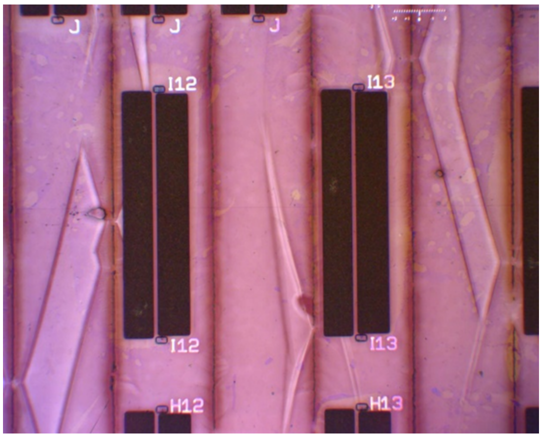

Figure 4.21: GaN SLEDs with gold plated bondpads.

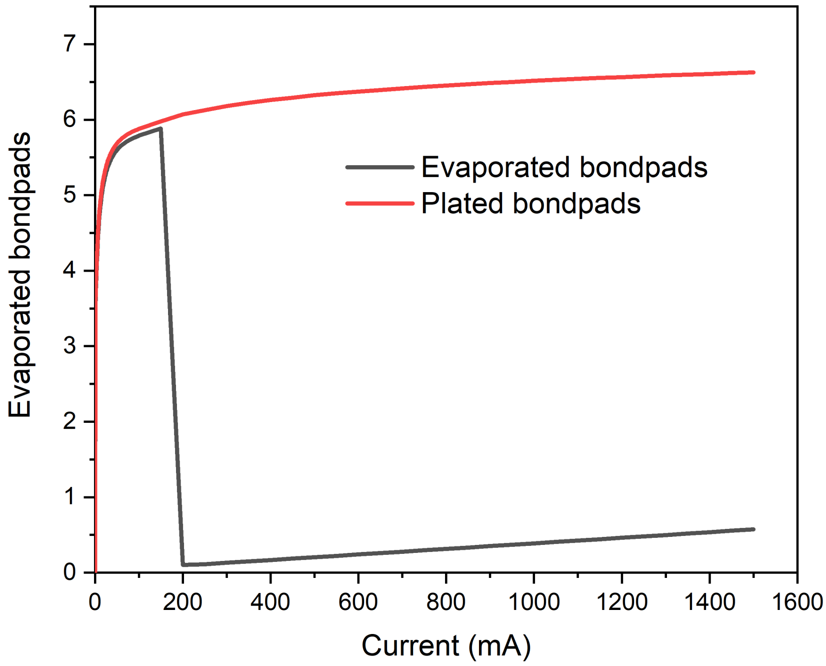

Figure 4.22: I-V characteristic of GaN laser diodes with evaporated and electroplated bondpads.

plated bondpads. Figure 4.22 shows the I-V characteristic of devices with plated bondpads and evaporated bondpads. The devices with evaporated bondpads fail and short circuit when a high current is applied while the devices with plated bondpads avoid failure due to better thermal management.

4.8 Summary

Surface emitting SLED devices were fabricated using a process similar to that of a ridge waveguide laser diode. A wafer cleaning process was developed which greatly improved the contact resistivity of the Pd p-contact. The removal of surface oxides from the p-GaN layers is shown to be an important step in the fabrication process. The impact of the cleaning process shows that surface contamination can have a significant impact on the electrical performance of a SLED or similar device. It is clear that a robust cleaning method is required as the HCl and BOE dips by themselves were not sufficient to allow an ohmic contact. As well as removing surface contaminants, the KOH clean may help to reduce the Ga/N ratio at the surface which improves the adhesion of the Pd contact [80].

The thermal annealing treatment of the Pd contact was also optimised. The thermal annealing step helped to improve contact stability and resistivity with a 400°C anneal providing an order of magnitude reduction. The impact of annealing shows that the contact is not stable as deposited. If the sample is not annealed during the process a change in contact resistivity and performance may occur during the operation of the device due to Joule heating and non-radiative recombination.

The Surface Evolver program was used to model the behaviour of photoresist during thermal reflow. The program accurately predicted the shape of the resist. With this tool the change in geometry from the shapes outlined on the mask could be predicted. The thickness of resist to feature size ratio emerged as a key parameter in determining the final reflow shape. This led to adjustments being made to the mask design to allow for easier alignment and more consistent mirror etch angles. The Surface Evolver has potential to be a very useful tool in the design and optimisation of small photoresist features.

An ICP mirror etch process was designed to provide a smooth, angled sidewall for the turning mirror. The BCl_3 based etch provided 1:1 selectivity between GaN and photoresist. It was noticed that GaN was etched slightly more preferentially when the ICP power was increased. This also increased the overall etch rate as the energy of the ions in the plasma was increased. The pattern transferred onto the semiconductor exactly matched the profile provided by the photoresist, underlining the importance of predicting and controlling the reflow.

Chapter 5

Characterisation of SLEDs

5.1 Introduction

In this chapter the results of characterising GaN based surface emitting SLEDs are presented. The characterisation was performed to measure the performance of the devices in the key areas of SLED performance: optical power, spectral quality, beam quality and efficiency.
Where not stated the results in this chapter pertain to a 1 mm long device with two outputs emitting in the same direction. The width of the waveguide for all devices unless stated otherwise was 3 μm. There was a 10μm passive absorbing region in front of one output in order to reduce the impact of optical feedback in the waveguide.The combination of 1 mm waveguide length and 3 μm width was chosen as it provided a suitably long gain medium to provide significant amplification while still requiring a relatively low current injection to reach the superluminescent threshold. The chip was thinned to a thickness of 250μm and featured a polished back surface with a SiO_2 anti-reflection coating applied. The performance of devices with different geometries and mirror structures as well as arrays of SLED ridges are also discussed. These measurements are compared with the theoretical results in Chapter 3. The measurements in this chapter also help to illustrate the impact of the fabrication process improvements made in Chapter 4.

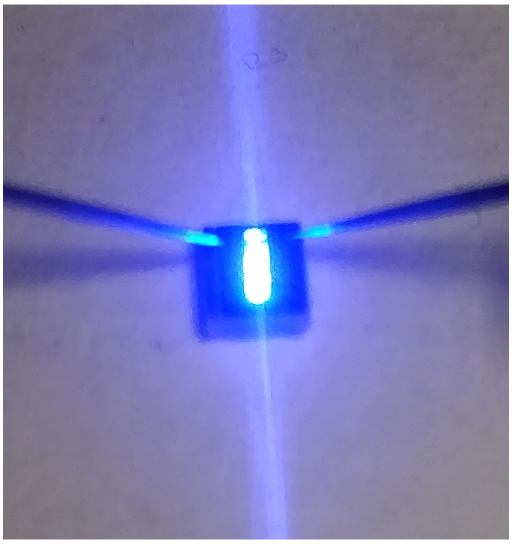

Figure 5.1: GaN surface emitting SLED on AlN mount under pulsed operation. The device is mounted substrate side up and is emitting from both facets.

5.2 Experimental set up

The light-current-voltage (LIV) characteristics of the GaN SLEDs were measured by probing the devices on wafer. The devices were placed on a glass microscope slide with a Thorlabs FDS1010 silicon photodetector positioned underneath. The detector was placed as close as possible to the bottom of the sample to ensure all of the light from both outputs was collected. The photocurrent was measured by a Keithley 2000 multimeter.
Bias was applied to the device using a coaxial probe to minimise electrical reflections in the cable. The voltage source was a HP 8114A pulse generator. The applied current was monitored using a inductive current clamp and Tektronix digital 5 GHz oscilloscope. A schematic of the experimental set up is shown in Figure 5.2.
The device was tested in pulsed operation to reduce the effects of Joule heating. The pulse length was 220 ns applied at 45.5 kHz giving a 1% duty cycle. The pulse length was chosen as it was the shortest pulse which the pulse generator could provide while maintaining a square pulse shape.
For higher current testing required to drive the arrayed devices into superluminescent mode a PICOLAS laser driver was used. This driver is capable of providing pulses with up to 20 A amplitude.
DC measurements were taken using a Keithley 2400 sourcemeter which was used as a current and voltage source.

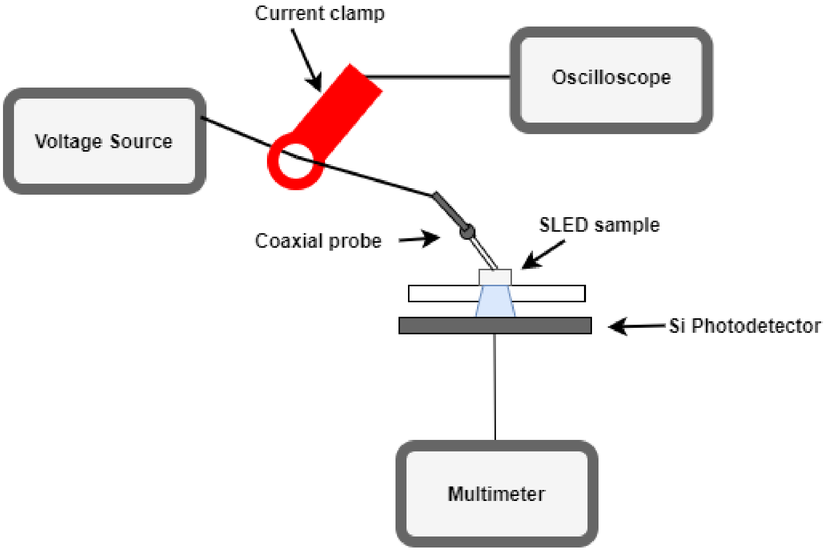

Figure 5.2: Schematic of experimental set up for measuring LIV characteristics of surface emitting SLEDs.

5.3 Electrical characteristics

5.3.1 DC measurements

The I-V characteristics of a 1 mm long GaN surface emitting SLED in DC mode up to 100 mA are shown in Figure 5.3. The device turns on at 3.5 V and the as the current is increased to 100 mA the voltage increases by 2 V. The current is not increased above 100 mA in DC mode to avoid destroying the device.

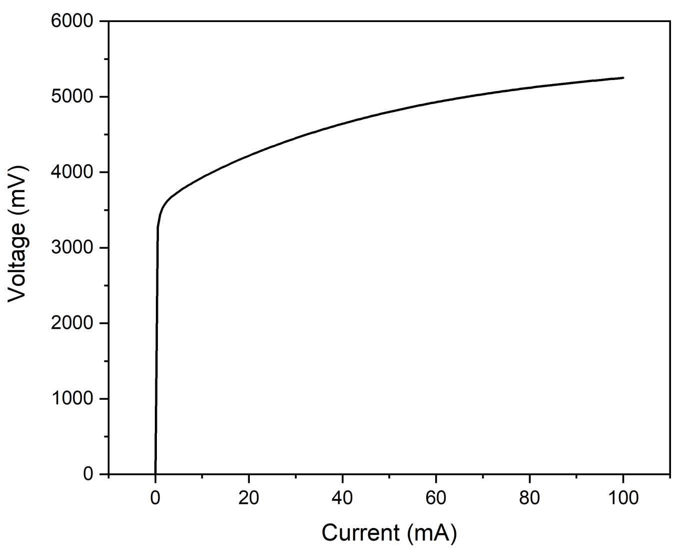

Figure 5.3: I-V curve of GaN SLED in DC mode.

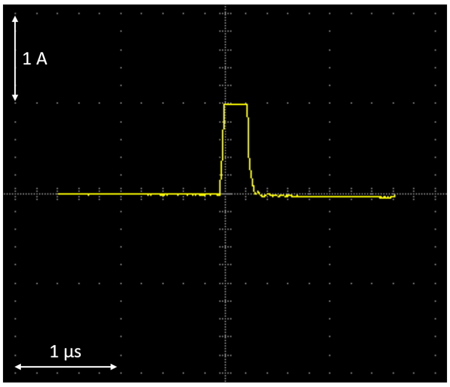

Figure 5.4: Square pulse of current 220 ns long delivered to SLED measured using 5 GHz oscilloscope. The rise time of the pulse is 5 ns and the fall time is 10 ns.

5.3.2 Pulsed characteristics

Figure 5.4 shows an electrical pulse measured on the oscilloscope. The pulse shows a square wave shape. The impedance mismatch between the 50 Ω pulser output channel and the device caused reflections in the cable initially, distorting the pulse shape. A 47 Ω resistor was introduced in series with the 3Ω device which improved the pulse shape resulting in a measurable square pulse. Packaging the devices and minimising cabling would help to improve this pulse further in future devices.

5.4 Optical power

The optical power measurements in pulsed mode were taken manually, increasing the current in increments of 100 mA and taking the power reading from the multimeter.
The L-I curve in Figure 5.5 shows that the devices enter the superluminescent regime when 300 mA of current is applied. The current density then required to induce superluminescence in the material was 10 $kAcm^{-2}$. After this point the optical power increase is superlinear with respect to applied current.

Under pulsed operation the SLEDs were stable up to 1.5 A of current which was the limitation of the equipment used. The maximum recorded optical peak power of 2.2 W was recorded at this current. This power was verified by using a thermopile.
The high optical power is a testament to the high crystalline quality of the material. The low defect density means there are fewer losses in the waveguide and allows for a high net gain to be achieved.

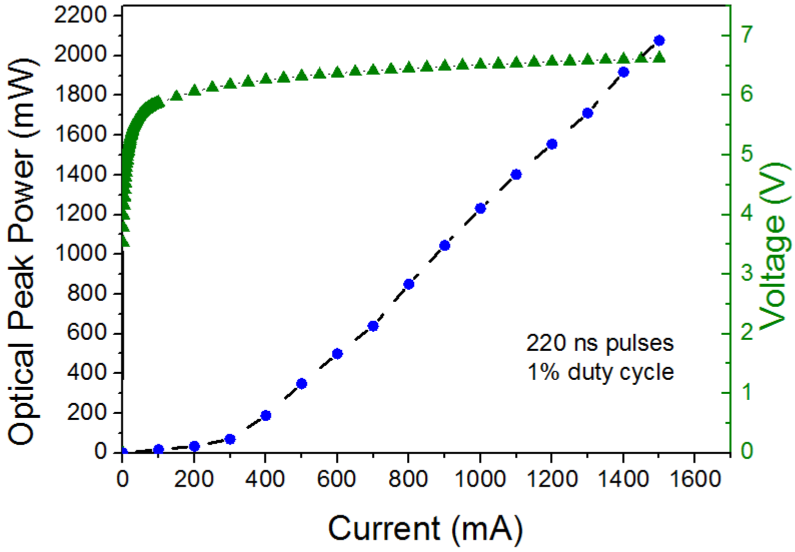

Figure 5.5: Light-current-voltage characteristics of GaN based surface emitting SLED.

Another factor is that a broad spectrum can be maintained even at these high output powers, through a combination of the turning mirrors and antireflection coating. The onset of parasitic lasing is a limiting factor of the optical power which can be obtained from edge-emitting SLEDs. The spectral measurements are discussed in more detail in section 5.6.

5.4.1 Efficiency

Figure 5.6 shows the external quantum efficiency curve of the device as current is increased. The efficiency of the device is constantly increasing with current in this range suggesting that greater efficiency could be realised if higher current pulses could be applied. The maximum EQE realised was 51% at 1.5 A. The slope efficiency of the device above transparency is 1.5 WA^{-1}.

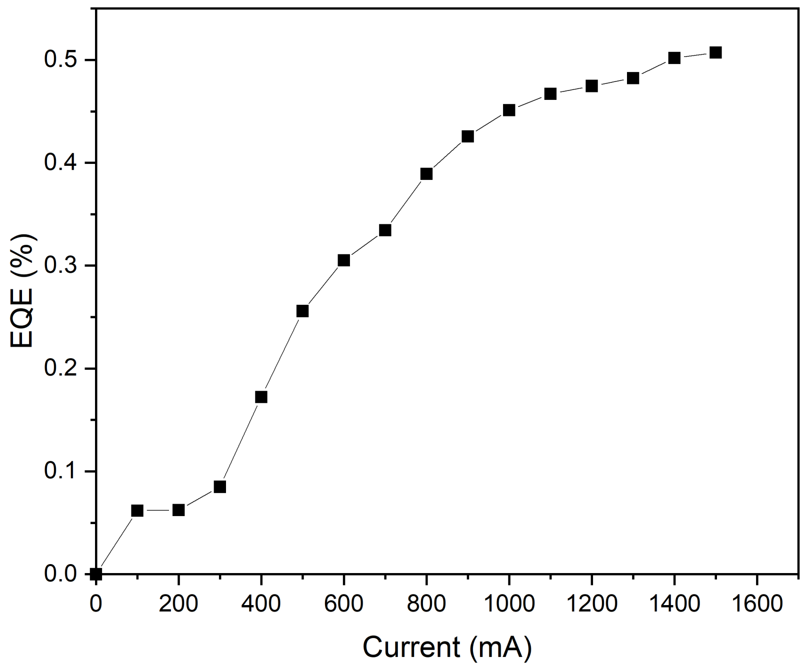

Figure 5.6: External quantum efficiency of blue SLED. The devices operates at maximum efficiency at high current.

The device reached maximum efficiency well above the transparency current. Finding ways to reduce the transparency current by changing the device geometry could also help to realise a more efficient device. The 2.2 W of peak optical power measured from these devices is the highest optical peak power recorded from a GaN SLED to date.

5.4.2 Pulse length

As some longer pulse lengths are desirable for some application, the effect of increasing the pulse length was investigated. While pulse lengths were increased the 1% duty cycle was kept constant throughout the measurements. The impact of increasing the pulse length is shown in Figure 5.7.

The ASE spectrum is redshifted with increasing pulse length and the optical power decreases. The peak ASE wavelength redshifts by 3 nm from 416 nm to 419 nm as the pulse length is increased from 200 ns to 1500 ns. The red shift is an indicator of significant heating in the device. Using the Varshni equation [100]:

$$E_g = E_g(0) - \alpha T^2/(\beta + T) \tag{5.1}$$

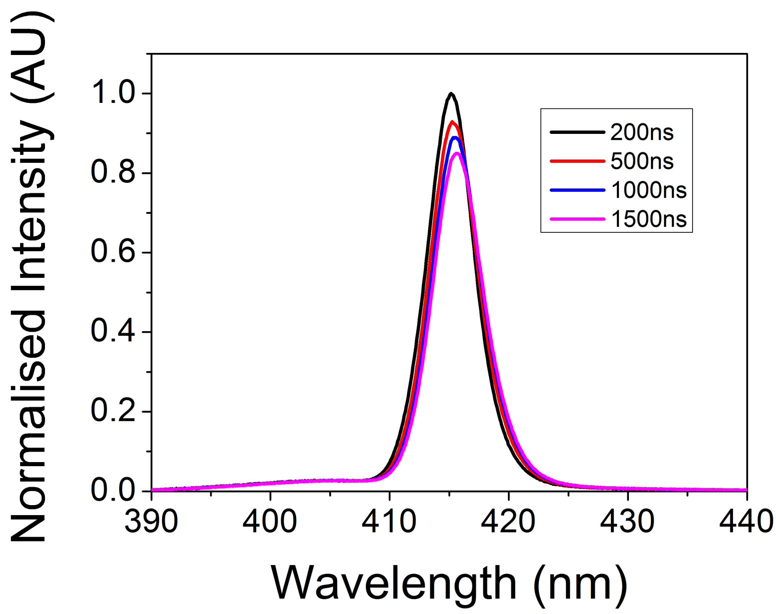

Figure 5.7: ASE spectra of GaN SLED at 1.5 A with different pulse lengths. The duty cycle is 1%.

with the material constants $\alpha = 1.29 \times 10^{-3} eVK^{-1}$ and $\beta = 1280K$ a temperature increase of 100°C is calculated at the junction as the pulse length is increased from 200 ns to 1500 ns.
The increase in pulse length also led to an irreversible loss of output power from the device. As the duty cycle was the same for each pulse length it is clear that the degradation occurred during the pulse and was not due to a buildup of heat over the course of multiple pulses. Decreasing the duty cycle or frequency then would not improve the device performance at longer pulse lengths. The requirement to improve longer pulse performance is for better thermal dissipation to remove heat from the junction quickly before any degradation can take place.

5.4.3 Mirror shape

The shape of the turning mirror trench had an influence on the optical power which could be collected from the device. This is attributed to the slope of the mirror sidewall being different depending on the curvature of the feature. As discussed in Section 4.6.1, the photoresist profile depends on the curvature of the pattern. The process was optimised to provide a 45° angle for a straight sidewall with no curvature. Other mirror shapes where included however with a curved sidewall in an attempt to better contain the light in the lateral direction. These shapes are shown in Fig 5.8.

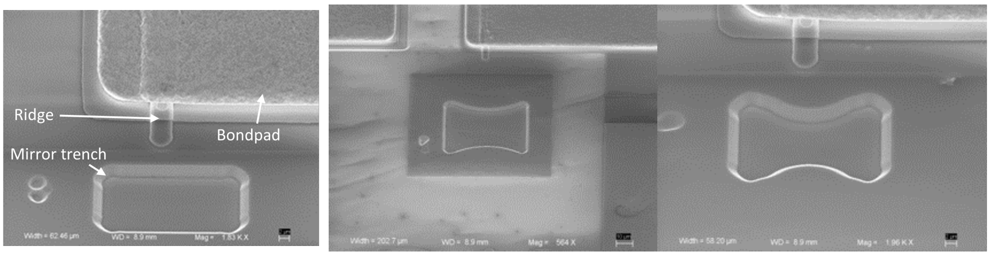

(a) (b) (c)

Figure 5.8: SEM images of different mirror trench shapes for GaN SLEDs.

The different resist profile meant that shallower angles were etched and less of the light was reflected inside the critical angle and was instead coupled into the chip. The angles for the mirrors with radii of curvature of 20 μm and 50μm were 39.3 $^\circ$ and 40.8 $^\circ$ respectively. The difference in L-I curves between the different mirror shapes is shown in Figure 5.9. In the future, the etch process should be optimised to provide a 45° angled sidewall for these curved mirror features. The lower power observed for the curved mirror shapes illustrates the importance of achieving a mirror etch close to 45°.

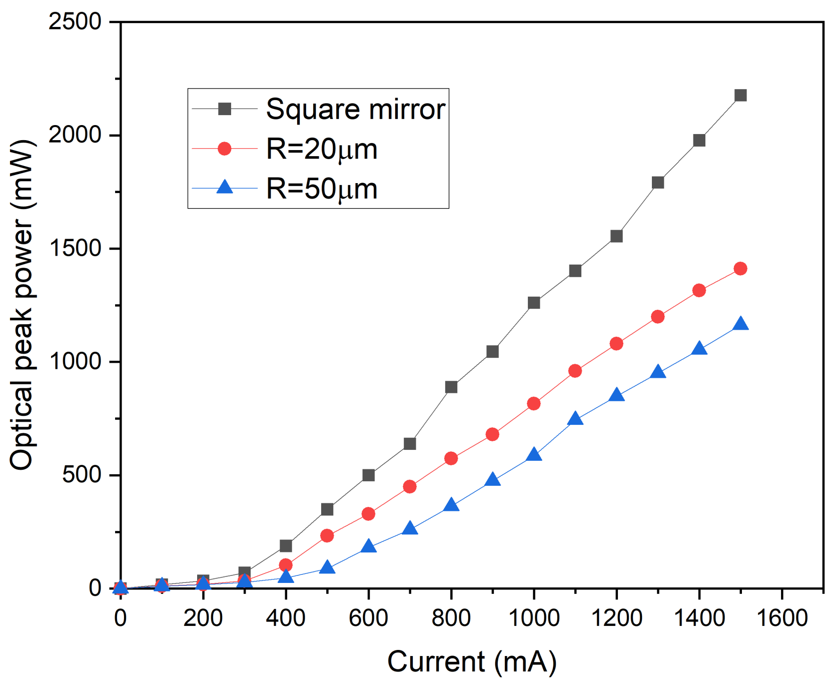

Figure 5.9: Light-current characteristic of blue SLEDs with different turning mirror shapes.

5.4.4 Device length

The length of the waveguide influences the output power and transparency current of a SLED. Figure 5.10 shows the L-I characteristic of 1 mm and 2 mm long SLED devices. As predicted by the model presented in chapter 3, the shorter device enters the superluminescent regime at a lower current than the longer devices. The greater contact area of the 2 mm device means a higher current is required to reach the transparency current density.

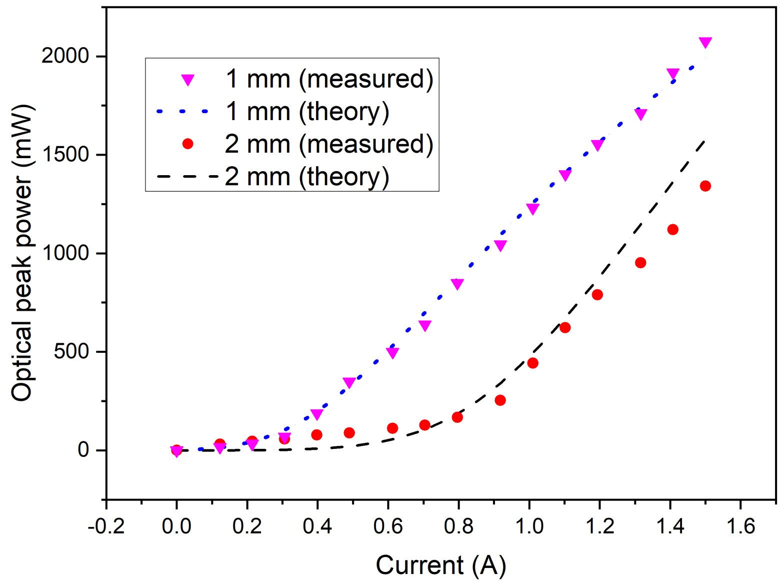

Figure 5.10: Light-current characteristics of 1 mm and 2 mm long GaN based surface emitting SLEDs compared with theoretical model.

Above transparency the 2 mm device shows good agreement with the theoretical model. Once the longer device is driven above transparency, the optical power increases more rapidly with current than the 1 mm device due to the longer gain medium. It would be expected that driving the devices to higher currents would result in the 2 mm device becoming relatively more efficient than the 1 mm device.
The fit was achieved by editing the linear gain coefficient a which is described in Chapter 3. This was tweaked until the 1 mm device from the simulation matched the experimental measurement. The 2 mm simulation was then run using the same a value to produce the result shown in Figure 5.10.

5.5 Spectra

The electroluminescence spectra of the GaN SLED were measured using a high resolution ANDO spectrometer. This spectrometer provided a resolution of 0.2 nm which was confirmed by measuring the spectrum from a laser diode with a peak wavelength at 420 nm The experimental setup was similar to that described in 5.2 with a lensed fibre optic cable in place of the silicon photodetector. The spectra were measured on the same device before and after the application of antireflection coating. No external polariser was used in these measurements.

For the measurements of spontaneous emission spectra, the fibre optic cable was used to collect light from the top side of the device to reduce the amount of ASE collected. An external polariser was also used to filter out any excess ASE which was being collected. The spontaneous emission spectra were measured using an Ocean Optics digital spectrometer with a resolution of 2 nm, as the high resolution was not required to detect peaks in this case.

5.5.1 Antireflection coating

Figure 5.11 shows the evolution of the emission spectrum of a GaN SLED without any AR coating applied to the back surface with current. The spectrum narrows significantly above 750 mA and continues to narrow with increasing current. This is evidence of parasitic lasing in the chip. After this observation a SiO_2 AR coating with a thickness of 43 nm was applied to the back surface.

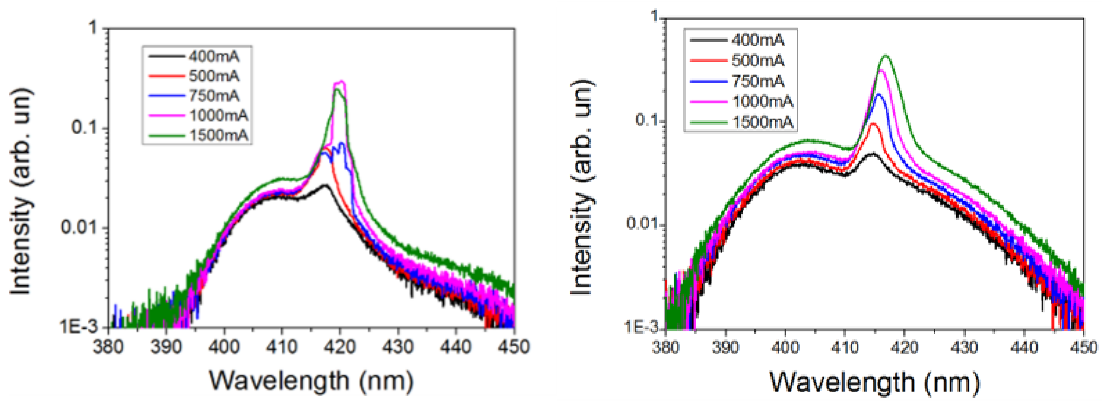

(a) (b)

Figure 5.11: Electroluminescence spectra of blue surface emitting SLED (a) before and (b) after the deposition of antireflection coating.

Figure 5.11 shows that the AR coating significantly reduced the effects of

parasitic lasing. The AR coated device maintains a broad smooth emission spectrum with a FWHM of 6 nm up to the maximum driving current of 1.5 A. This stability of the spectral quality is what allows the SLEDs to reach such high optical powers. The non-AR coated example above shows that parasitic lasing can cause extreme narrowing and roughening of the spectrum effectively limiting the power of the device while in SLED mode to what can be accomplished below 750 mA as once parastic lasing has begun the device can no longer be considered a SLED. The broad smooth spectrum which is maintained at these very high optical powers suggests that the combination of AR coating and turning mirrors are very effective in preventing feedback in the device. The AR coating also appears to boost the amount of spontaneous emission which is extracted due to less light being trapped in the chip by total internal reflection. The spontaneous emission continues to increase with current up to the highest applied current density of 100 $kAcm^{-1}$. This suggests that the carrier population is not yet saturated and that additional gain is possible if higher current densities can be applied.
Figure 5.12 shows the emission spectrum from the SLED at maximum power on a linear scale. The spectrum shows that the ASE is the dominant contribution to the total optical power. The peak wavelength is at 416 nm. This is red shifted with respect to the peak of the spontaneous emission spectrum. This is a result of the lower energy states being filled more quickly as carriers are injected and being amplified more readily. A red-shift is visible in the AR coated spectrum as current increases. This is due to heating in the device.

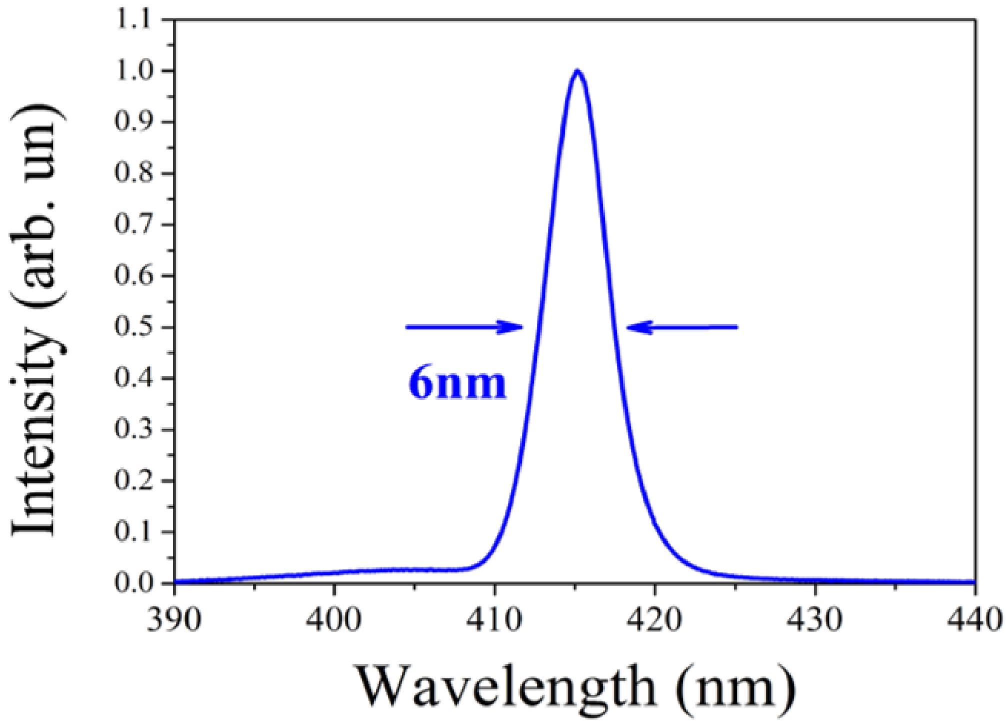

Figure 5.12: Electroluminescence spectrum of AR coated GaN SLED at 1.5 A.

5.6 Carrier population

5.6.1 Gain

The optical gain curve was extracted from the L-I curve in Figure 5.5 using Equation 2.21. From this the material loss at transparency (300 mA) could be calculated as 25 cm^{-1}. It is assumed, based on results from SILENSe simulations, that the material loss remains approximately constant regardless of the applied current density.

It is notable that the gain continues to increase well above transparency. This is indicative of an increasing carrier population in the QWs. It might then be expected that Auger recombination would begin to cause a droop in efficiency as the current density is increased. This however is not observed. A potential explanation for this is that stimulated recombination is dominant in this regime. The stimulated recombination rate is directly proportional to the photon density [66] which increases exponentially above transparency with carrier density. This means that once the devices enters the superluminescent regime the level of stimulated recombination will increase rapidly with increasing carrier density due to the higher number of photons in the waveguide available to induce recombination. The stimulated recombination

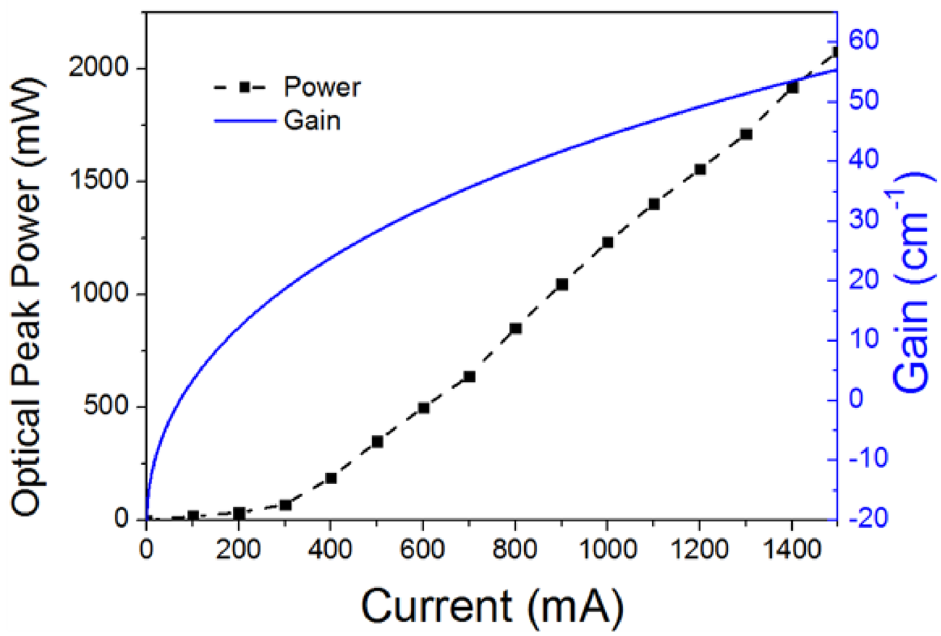

Figure 5.13: Extracted optical gain curve from SLED L-I measurement and theoretical gain curve for 2 InGaN QWs.

increases even more rapidly than the Auger recombination which goes with the carrier density cubed, meaning only a small portion of the injected carriers go to Auger recombination. This would agree with the predictions of the model presented in Chapter 3 as well as other recent models on GaN based SLEDs [62] and laser diodes [101].

5.6.2 Spontaneous emission spectra

The spontaneous emission from the device was measured from the top side of the device to reduce the collection of ASE which is emitted through the back side of the device. A polariser was used to filter out any ASE light which may have been scattered and collected by the detector. This works as the stimulated recombination produces photons with identical polarisation. If these photons are scattered into the detector they will still have the same polarisation as one another. Using a polariser then will eliminate the ASE while allowing for most of the randomly polarised spontaneous emission to be collected.
The evolution of the spontaneous emission with current is shown in Figure 5.14. It is evident that the spontaneous emission intensity is not saturated even at very high current density. This is an indication of increasing carrier density which is in agreement with the gain curve which suggests that although the gain is beginning to roll over it has not yet fully saturated at 1.5

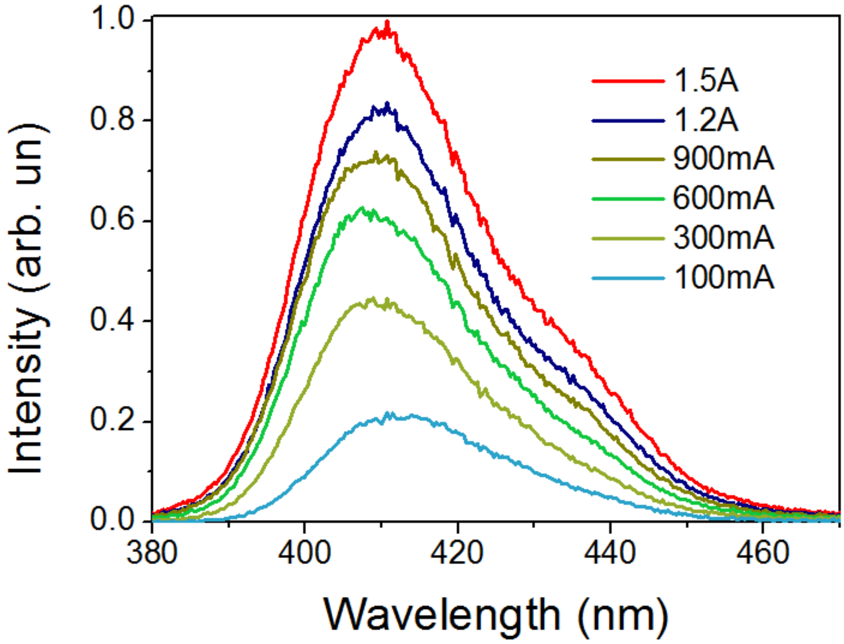

Figure 5.14: Electroluminescence spectrum of AR coated blue surface emitting SLED.

A. The inital blue shift of the spontaneous emission peak from 412 nm to 405 nm is attributed to the screening of the inbuilt piezoelectric field by carriers in the QWs, thereby reducing the effects of the quantum confined Stark effect. The ensuing redshift at higher currents from 405 nm to 410 nm is attributed to device heating.

The spontaneous emission spectra can be used not only to provide information on the carrier population in the QWs but also the temperature of the carriers. By taking the logarithmic slope of the high energy side of the spontaneous emission spectrum the carrier temperature can be extracted using the relation [102]:

$$\frac{dln(I)}{dh\nu} = -\frac{1}{kT_c} \tag{5.2}$$

Using the spontaneous emission spectra above it was calculated that the device temperature increases by 100°C between transparency and maximum power. Using the Varshni equation and to calculate the increase in temperature by measuring the redshift of the spontaneous emission peak also gives an increase of 100°C between these two driving currents.

Figure 5.15 shows the spontaneous emission intensity versus current. The spontaneous emission continues to increase above transparency up to the maximum driving current of 1.5 A. This is an indicator that the carrier population continues to increase above transparency. This shows that the carrier density dependent gain is not clamped at transparency. This is a result

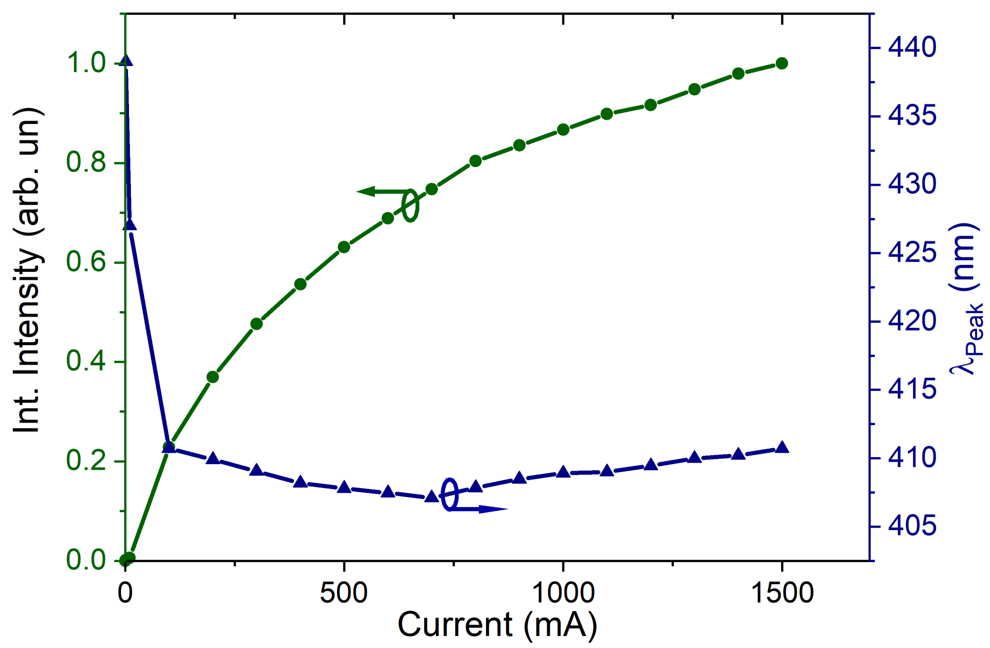

Figure 5.15: Integrated intensity and peak wavelength of the spontaneous emission spectrum versus current.

of the low reflectivity facets preventing photon roundtrips in the waveguide. Relatively low photon density in the middle of the waveguide allows for the carrier population to increase in this region with increasing current even if it is clamped near the ends of the waveguide.

5.7 Near and Far field characteristics

The beam quality of a SLED is a distinct advantage it has over conventional LEDs. Low divergence allows for efficient coupling of high power into fibre optic cables. This combined with the small etendue of a SLED mirror or facet can provide far superior fibre coupling than an LED.

5.7.1 Near field

Near field measurements were taken using the setup outlined in section 5.2 with a lens and CCD camera in place of the silicon photodetector. A test sample with circular patterns was placed above the CCD in place of a SLED sample backlit using a white light source. The camera was focussed on these

circular features to ensure the focal plane was correct for a near field image. The test sample was then replaced with a SLED device.
The device was switched on and snapshots were taken at different levels of driving current to record how the light output varied with current. Figure 5.16 shows the evolution of the SLED near field with current. The images show that initially when low current is applied and spontaneous emission is the dominant recombination factor, most of the light is coming from the ridge waveguide. As the intensity is increased closer to transparency, the turning mirrors become visible. Above transparency the light being reflected from the turning mirrors becomes the dominant light source as ASE becomes the dominant recombination process in the device. At maximum power the spontaneous emission from the ridge is negligible with respect to the amplified light from the turning mirrors. This is evidence that the device has a small etendue with most of the light coming from the turning mirror which has an emitting area of 80 μm^2.

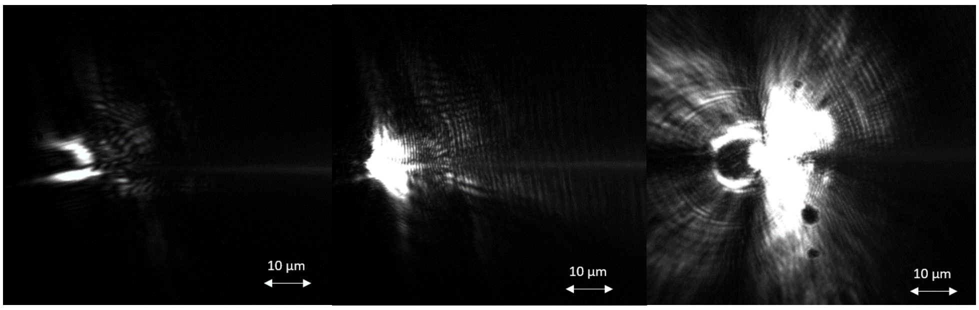

(a) (b) (c)

Figure 5.16: Near field images of the end of surface emitting SLED waveguide at (a) 300 mA, (b) 750 mA (c) 1200 mA.

Near field images were also used to investigate the carrier population effects described in Chapter 2. A decrease in spontaneous emission intensity would be an indication of decreased carrier density in a given region of the device. It was required for this measurement to measure the spontaneous emission only, and not the amplified light as the spatial distribution of ASE intensity would not be related to the carrier density distribution.
In order to avoid measuring any amplified light, a copper plate with a 1 mm wide slit in the centre was placed underneath the device with the ridge oriented perpendicular to the walls of the slit. The centre of the ridge was aligned with the centre of the slit so that both turning mirrors were blocked from the view of the camera by the copper plate. The images collected were then of the spontaneous emission from the ridge waveguide only.

Near field images of the ridge are shown in Figure 5.17. As the current is increased the spontaneous emission intensity increases. The intensity profiles show that as the current is increased while the spontaneous emission intensity increases it also becomes more non-uniform across the waveguide. At and below transparency the intensity profile is flate across the ridge while at high current the spontaneous emission intensity peaks in the centre of the waveguide with and decreases towards the end. This is evidence of high photon densities at the end of the waveguide due to ASE causing higher levels of stimulated recombination near the ends of the waveguide which leads to lower carrier density in these regions.

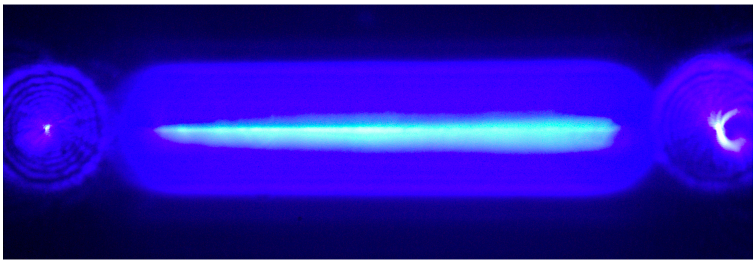

Figure 5.17: Near field image of blue SLED ridge at 1.5 A.

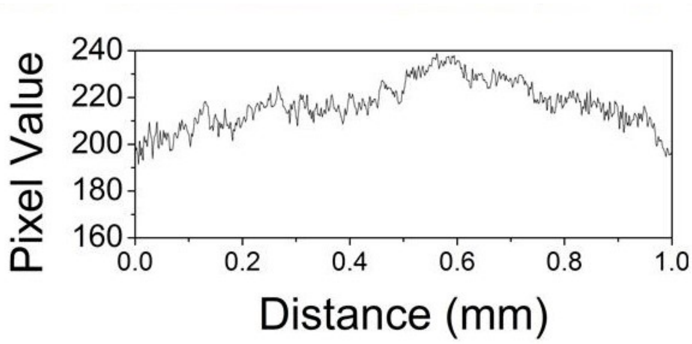

Figure 5.18: Intensity profile showing lower levels of spontaneous emission near ends of SLED waveguide.

5.7.2 Far field

The far field characteristices of the device were measured in a similar manner to the near field measurements. The circular test sample was focussed on using the lens and CCD camera. A scattering element then replaced the test sample, with the device positioned 10 cm above. Figure 5.19 shows the far field characteristic of the device at maximum power. The divergence from a single facet is $15^\circ \times 7^\circ$. The distance between the facets means the device behaves as two separate point sources. Ideally for efficient fibre coupling all of

the emission would be from a single facet to minimise the etendue.
The far field shows much higher intensity emission from one facet than the other. The facet on the right exhibits approximately three times higher light output than the left facet. This is due to a passive absorbing region before the left facet, which serves to reduce the impact of reflections in the waveguide. This asymmetry shows that higher powers could be achieved if this absorbing region is removed, however additional care would need to be taken in order to prevent reflections and the formation of a cavity.

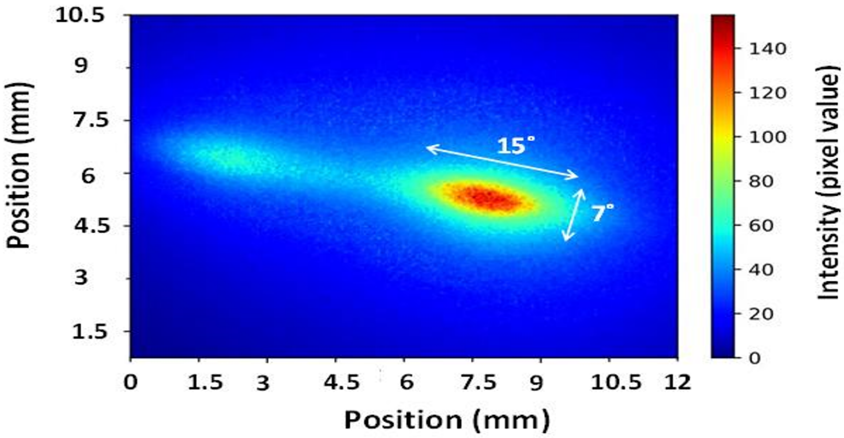

Figure 5.19: Far field emission characteristic of blue surface emitting SLED at 1.5 A.

5.8 SLED arrays

This section presents results obtained from surface emitting SLED arrays. These devices comprise of multiple ridge waveguides arrayed under a single bondpad with a shared turning mirror. The devices are driven simultaneously with the objective of attaining higher optical power than a single SLED device from a similarly small emitting area. The devices require higher currents to reach the superluminescent threshold as the active area of the device is larger. This required the use of a high power Picolas laser driver to deliver high amplitude pulses.

5.8.1 L-I-V Characteristics

Figure 5.20 shows the L-I characteristic of the two-ridge and three-ridge SLED arrays. The devices shows a much larger threshold than the single-ridge device as expected, with superluminescence being achieved at an injection currents of 750 mA and 1.3 A respectively. The increase in power above transparency is large with a slope efficiency of 0.8 WA^{-1} for the two ridge device. Maximum optical peak powers of 1.2 W for the 2 ridge array and 1.05 W for the three ridge array are measured at 3 A. The devices tended to break down at currents higher than this. This was most likely due to large amounts of power being converted to heat. At 3 A with an operating voltage of 9 V the applied power electrical is 27 W. With just over 1 W of optical power being detected this suggests that the remaining 26 W is converted to heat. This heat causes a failure of the p-contact resulting in a short circuit.

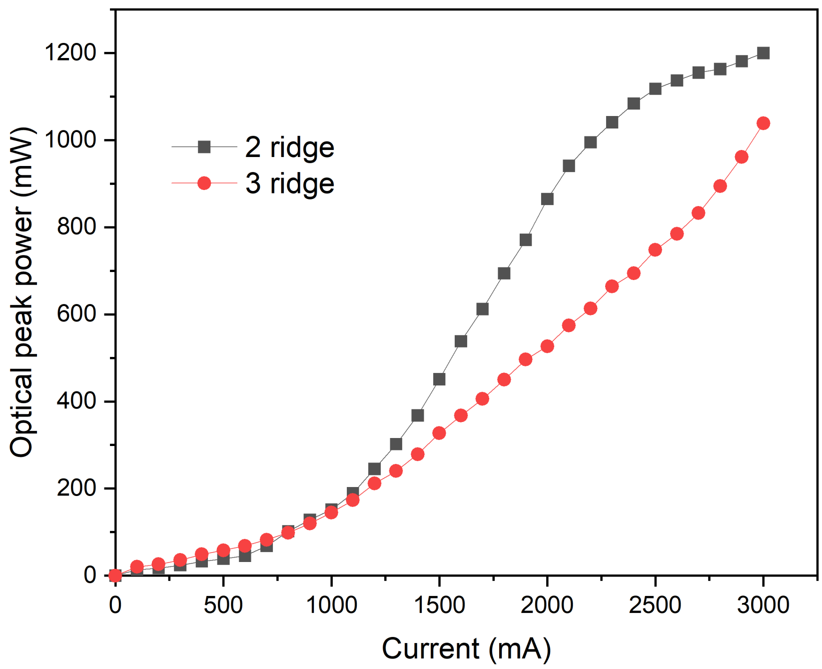

Figure 5.20: Light-current characteristic of multi-ridge SLED arrays.

5.8.2 Spectra

Figure 5.21 shows the spectrum from a three ridge SLED array in pulsed mode. The ASE peak can be seen to emerge at 1.1 A with a peak at 415 nm. The peak remains broad a smooth up to the maximum output power with a FWHM of 6 nm. At the maximum power, the ASE peak has redshifted to 418 nm due to heating in the chip. This is an indicator that the turning mirror is preventing feedback in the ridges and that reflections are not occurring between the ridges.

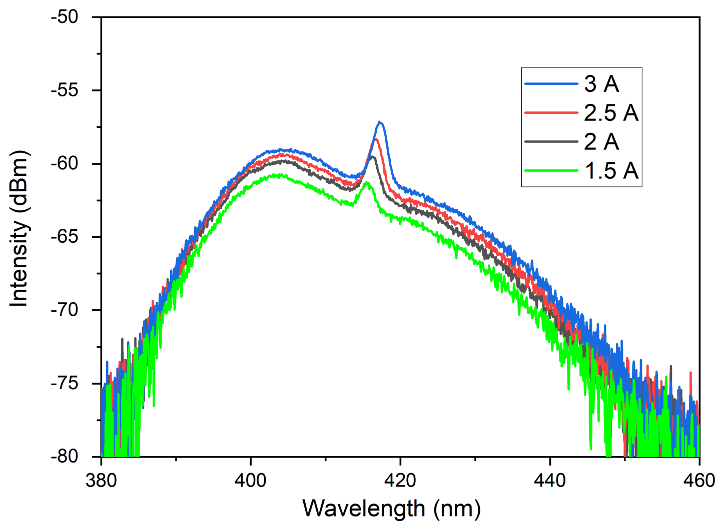

Figure 5.21: Evolution of electroluminescence spectrum of 3 ridge SLED array with current.

5.8.3 Near field

Figure 5.22 shows the evolution of the near field pattern of a two ridge SLED array under different injection currents. The turning mirror lights up when the device is driven above transparency at 700 mA. Similarly to the single ridge device, an interference pattern is visible due to the single slit diffraction effect from the light striking the turning mirror. The yellow luminescence which is visible is due to light being absorbed and down-converted in areas of the substrate with a high defect density.
Figure 5.23 shows the same evolution for an array with three ridges. The near field shows that the ridges are emitting approximately equal levels of light. Illumination is not observed between the ridges This shows that the current is not driving any ridge preferentially over the others, suggesting that the plated bondpad is making good uniform contact with each ridge and that the ridges are well isolated from one another by the SiO_2 layer. The even distribution of current across the three ridges is confirmed at transparency, where three distinct interference patterns are visible at the mirror. This shows that all three ridges have been driven above transparency simultaneously.

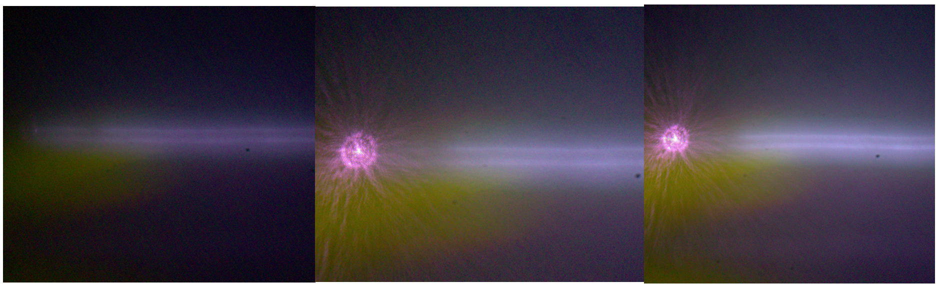

(a) (b) (c)

Figure 5.22: Near field images of two-ridge SLED arrays at (a) 400 mA, (b) 800 mA and (c) 1200 mA.

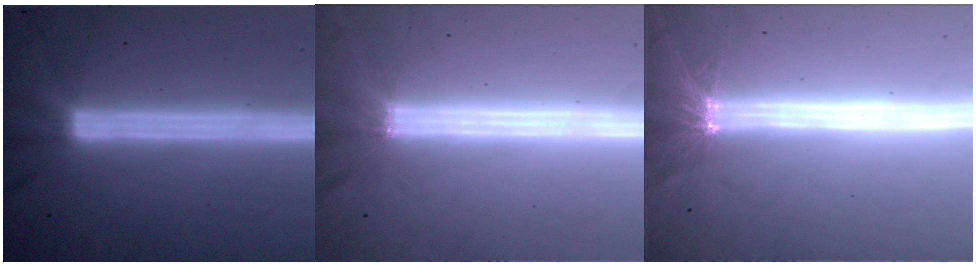

(a) (b) (c)

Figure 5.23: Near field images of three-ridge SLED arrays at (a) 500 mA, (b) 1000 mA and (c) 1500 mA.

5.9 Failure analysis

Over the course of this project, SLEDs were fabricated on different wafers. The results presented above represent the best devices fabricated on the wafer described in Chapter 4. Other devices fabricated on different wafers could not provide the same optical power, efficiency or reliability of these devices despite very similar or identical processing. The reasons for this are investigated in this section. The wafers which are examined are; Wafer 1 which was used to fabricate the best performing devices whose characteristics are presented above; and Wafer 2 which had very similar processing, but did not provide the same high optical power or reliability at high current density.
One of the characteristics of the poorer devices was to short circuit at high current density. This effect is shown in the I-V curves in Figure 5.24. After high current density had been applied with the pulser generator, the contact broke down creating a path for the current from p to n contact without passing through the junction.

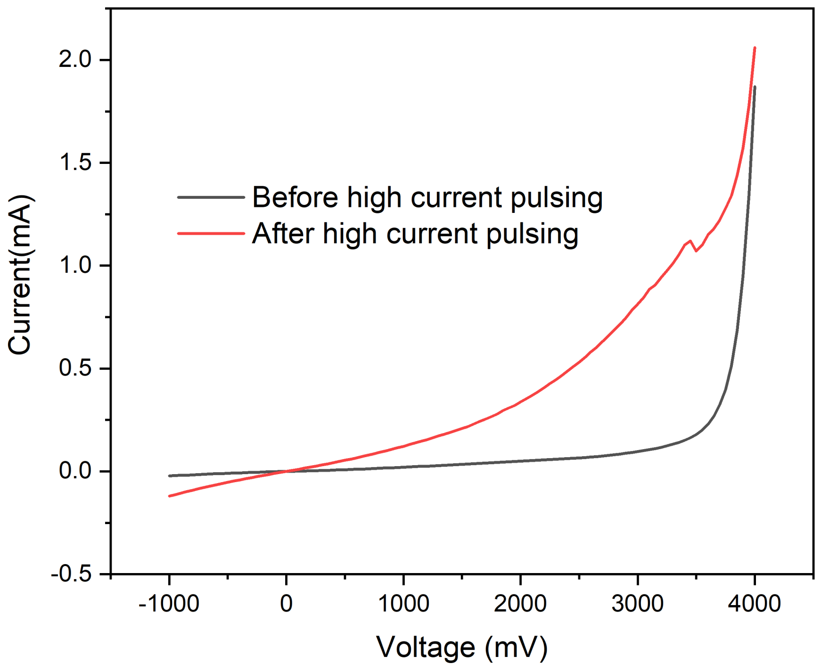

Figure 5.24: V-I curves of SLED devices before and after shorting due to high current application

The spontaneous emission spectra of the wafers used in these runs were also compared. The evolution of these spectra with current is shown in Figure 5.25.

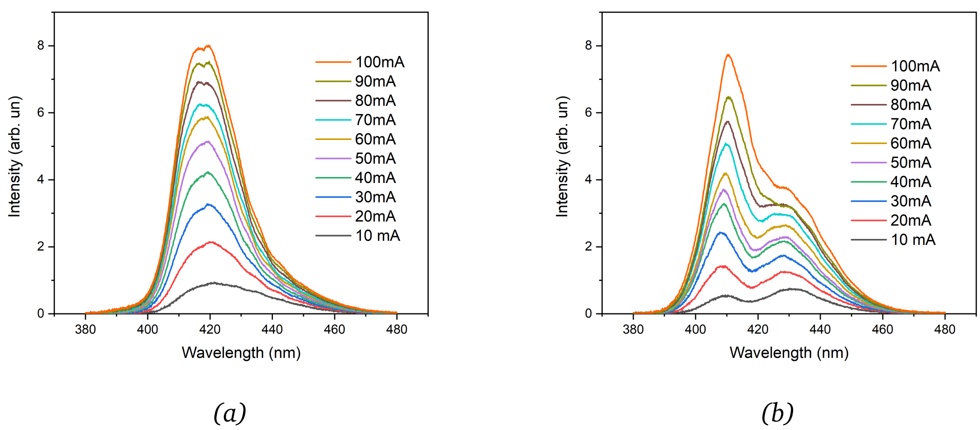

Figure 5.25: Spontaneous emission spectra of (a) wafer 1 and (b) wafer 2.

A clear double peak is seen in the wafer 2 spectra with the high energy peak at 405 nm becoming more prominent as current is increased. This is evidence of an imbalance in the carrier populations of each QW, possibly due to a difference in thickness. If one QW is dominating with a higher carrier population it will be the main contributor to the gain while the other QW is a source of losses in the waveguide. This decreases gain and increases the transparency current density.

Wafer 2 also provides a lower spontaneous emission intensity than Wafer 1. A lower level of radiative recombination means that more of the electrical power being applied is converted to thermal energy. This causes the device to heat up reducing reliability and causing local failure of the metal contact.

These results show the importance of high quality growth. As high levels of current density are required to provide gain, defects which result in non-radiative recombination can have a significant impact on the performance of a SLED.

The lower p-doping in the more recent wafers may also have prevented the devices from reaching the same levels of optical power as the best performing devices. The higher resistance on the p-side results in a higher bias required to drive the electrons into the active region. This extra bias means the difference between the injected electron energy and emitted photon energy is greater than in the sample with higher p-doping. This extra energy is released as heat. This extra heat may reduce the gain in the active region [103]. If this extra heating is more significant than the reduction in modal loss due to lower Mg doping, the device will be less efficient. Achieving the right level of p-doping for the optimum balance of low waveguide loss and high power conversion efficiency should clearly be a priority in the design of an epitaxial structure for SLED fabrication.

5.10 Summary

The results presented in this chapter indicate the potential of blue surface emitting SLEDs as a high-power, directional, low-coherence light source. Record optical peak powers for a SLED of 2.2 W are measured in pulsed operation at 1.5 A. The device shows external quantum efficiency close to 50%. A broad, smooth emission spectrum is maintained up to the maximum output power with a FWHM of 6 nm. This shows the effectiveness of the combination of the angled etched facet turning mirror and AR coating in preventing feedback in the device. This ability to prevent parasitic lasing allows for one of the principal barriers to Watt-class SLEDs to be overcome as spectral modulation and lasing often onset before device failure. The results indicate the high levels of optical gain which can be provided by InGaN QWs. While a high bias is required to drive the devices, the high separation of the quasi-Fermi levels means the excited carrier density will be high, generating high gain in the material.

The broad emission spectrum makes the GaN surface emitting SLED a potential source for pico-projection, BCEAS or OCT. With a central wavelength of 416 nm and a FWHM of 6 nm the temporal coherence length of the light from these devices is 12 μm. The use of a different active region based on quantum dots or quantum well intermixing could help to further broaden the spectrum and reduce the coherence length.

The near field and far field measurements show the high directionality of the devices. There is potential for efficient fibre coupling of the devices for use in integrated systems. In the future, the integration of micro-lenses onto the back side of the substrate could provide better beam quality for more efficient coupling or better beam quality for free-space applications. The integration of colour converting technology onto the back surface could also provide a directional light source for pico-projection and other display and solid state lighting applications.

Arrays of SLED ridges under a single bondpad are demonstrated for the first time. The arrayed devices are driven simultaneously with a shared turning mirror. The results show a device capable of supplying high optical peak powers in excess of 3 W in pulsed operation. SLED arrays present an alternative to lengthening device to increase the power output. The advantage of these devices over longer devices is the ability to obtain higher power without increasing the device footprint.

Chapter 6

Conclusion and future work

The aim of the research presented in this thesis was to study high power superliminescent light-emitting diodes both for their potential applications as a light source for the applications outlined in the introduction, and to further the understanding of the fundamental physical properties on which these devices are based.

It is demonstrated that surface emitting design can allow for high optical peak powers to be obtained from a SLED. The dual output nature of a surface emitting design combined with the excellent feedback suppression provided by the angled turning mirrors allow for high power without being impacted by parasitic lasing. Optical powers over four times greater than the previous record are reported for which the suppression of parasitic lasing and dual facet design is credited. The results in the modelling chapter of indicate the optimum device geometries and wafer structures for GaN based SLEDs. Recommendations are also made for the design of SLEDs using different materials such as GaAs and InP.

This thesis also presents the optimisation of processing steps which can be applied more generally to the fabrication of GaN based laser diodes.

The following chapter summarises the main results from chapters 3,4 and 5 before giving recommendations for future work in section 6.2.

6.1 Overview of the results presented

Chapter 3 focussed on the implementation of a numerical model to simulate the performance of SLEDs with different design parameters. The model used the dynamic interactions between the photon density and carrier density in the waveguide to find a steady state solution for the longitudinal distribution of carriers and photons. This was then used to calculate the average gain in the waveguide.

The model showed the importance of using numerical calculations to model SLEDs as it allowed for the non-uniformity of the longitudinal carrier density and photon density to be accounted for. Using a uniform carrier density model is shown to overestimate the potential optical power, particularly in longer devices where the discrepancies f orders of magnitude are observed.

The effects of device geometry were examined. The results showed that increasing the waveguide length can increase output power but suffers from lower efficiency when currents less than several amps are applied. Increasing the length is also shown to increase the level of modulations in the emission spectrum. Shorter cavity lengths are recommended for GaN devices to reduce the transparency current while longer cavity lengths are recommended for GaAs and InP devices to maximise the single pass gain.

Increasing the ridge width was shown to be a useful method of achieving higher power by increasing the emitting area. Once the confinement factor is close to the maximum however, increasing the ridge width further has few benefits as the transparency current will increase proportionally to ridge width. The effect of the number of QWs was simulated with fewer QWs appearing to be the best solution for GaN devices as they have a lower transparency current density. The effect of waveguide loss was also examined. It was shown that reducing the loss can allow for significant improvements in output power due to higher net gain.

Chapter 4 reported on the fabrication of surface emitting GaN SLEDs and the optimisation of the key process steps.

The optimisation of the Pd p-contact is described. A KOH cleaning step and thermal annealing helped to improve the stability and contact resistivity of the p-contact. It was also shown that using the Pd as a hard mask for the ICP ridge etch did not affect the contact resistivity.

The photoresist reflow effect was modelled in 3D using a soap film model. The results were used to design the mirror etch trenches for the SLEDs. The model also has other applications for micro-LED and micro-lens design. An ICP etch was developed to provide smooth angled sidewalls for the SLED turning mirror. The importance of bondpad plating for thermal dissipation is also discussed in Chapter 4.

Chapter 5 discusses the characterisation of surface emitting SLEDs based on freestanding GaN substrates. In this chapter record levels of optical peak power for a SLED are reported. The device produced 2.2 W of optical peak power under pulsed operation. The results also showed that the combination of turning mirror and antireflection coating are very effective in preventing the formation of Fabry-Perot modes. No evidence of parasitic lasing was seen in the emission spectrum up to the maximum power. The device also exhibited high spatial coherence. High levels of heating were noticed in the device by analysing the spontaneous emission spectra which illustrate the need for effective package to manage heat dissipation.

6.2 Recommendations for future work

This work has resulted in the demonstration of the first surface emitting SLED based on GaN. One of the advantages of the surface emitting nature is the potential to integrate other technologies onto the back surface of the chip. As the light emitted is high energy blue light, colour converting phosphors could be integrated to provide a white light or RGB source. This could be achieved using colour converting colloidal quantum dots which have been demonstrated in conjunction with SLEDs as a potential source for solid state lighting and displays [104, 105]. Remote pumping of YAG phosphors is another alternative which could make these devices a useful source for SSL applications [39]. The high power and directionality of the SLEDs makes them an ideal pump source for these colour converters and so this should be investigated further in the future.

Similarly the integration of micro-lenses onto the back surface should be considered. These optics could further improve the directionality of the SLEDs and help to provide efficient fibre coupling which is crucial for applications such as OCT.

The results presented in chapter 5 show the need for an effective packaging solution for the surface emitting GaN SLEDs. Heating at high currents prevented the devices from operating in CW mode or with longer pulse lengths and higher duty cycles. This limits the applications for which the device can be used as a light source. Future work should focus on developing a package which quickly moves heat away from the ridge, preventing failure of the contact. The package should also allow for easier operation of the devices as the current method of probing is not suitable outside of a research

environment.
Further work is also required on the optimisation of the p-contact. While improvements were made over the course of this PhD project, low resistivity will be required if the GaN SLEDs are to operate in CW mode above transparency. Rapid thermal annealing and use of a sacrificial Pd layer are two techniques which should be investigated to make progress in this area as they have shown promising results elsewhere [80, 106].
The work in Chapter 3 revealed the potential of different epitaxial structures and device geometries for GaN SLEDs. In the future a SQW structure should be examined as a means to reduce the transparency current density. As well as optimising the number of wells, the p-doping should be optimised. As observed in Chapter 5, wafers with a lower level of p-doping can result in lower power conversion efficiency due to high bias required to drive the device. Increasing the p-doping however can lead to increased losses in the waveguide due to modal overlap with the Mg dopants. Finding the best balance between low loss and high power conversion efficiency will be crucila to the further development of these devices. Some potential solutions to this issue include superlattice cladding layers [107], InGaN barrier layers between the QWs [108] and tunnel junction contacts [109].
Experimenting with different ridge geometries could allow for the realisation of higher optical powers, low transparency current densities and broader emission spectra. Further investigation into the effects of ridge geometry by device fabrication would allow for a deeper understanding of how SLEDs work and potentially provide suitable light sources for the myriad applications outlined in Chapter 1. For example shorter cavity lengths could be used to provide the broad spectrum required for imaging and OCT applications while longer ridge lengths could be used for applications where optical power takes precedence over spectral quality e.g. projection or BECAS.
The surface emitting SLED design should also be extended to other material systems. Using the recommendations from Chapter 3, GaAs and InP based SLEDs should be fabricated to produce high power, directional, broad spectrum sources in the red and IR parts of the spectrum. High power SLEDs emitting in this part of the spectrum could be highly beneficial for LIDAR systems [110, 111]. The ability to test these devices on wafer also provides the potential for cost savings over conventional edge emitting lasers which require cleaving and packaging prior to testing. This attribute could make surface emitting SLEDs a cost effective replacement for laser diodes in many areas.

Personal reflection

I would like to use this section to reflect on my experience of doing a PhD. This project has without doubt been the most challenging thing I have ever done. It has also, however, been the most fulfilling and satisfying. I have learned so much about physics, research, other people and myself over the past few years. I enjoyed working at something which is completely new. I had to become more independent and self-reliant in my work. Figuring out a problem, or lighting up a newly fabricated device gave me some moments of genuine euphoria. These moments were more than enough compensation for the more frustrating times.

I gained a new appreciation for the effort that goes into developing a new technology and discovering new knowledge. I realised that it is not a sudden eureka moment which brings us forward but more often several small steps. I had to learn to be more collaborative. I was lucky to be part of an excellent group who taught me much more than I could have ever learned alone. Most of all I learned never to stop questioning or trying to learn more.

I gained confidence in myself by interacting and debating with people who are leading in their field. I learned so much through discussions with my supervisors and others at UCC and beyond at conferences and workshops. The opportunities to speak publicly and defend my work allowed me to understand my work more clearly and develop my speaking skills.

I think the experience has changed me as a person, and not just as a scientist. I have learned to be more patient and diligent in all facets of my life. It has made me more open to new challenges and experiences. I am thoroughly glad to have had the chance to do this PhD and I feel like I am a better person for it.

References

[1] T. P. Lee, C. A. Burrus, and B. I. Miller, “A Stripe-Geometry Double Heterostructure Amplified-Spontaneous Emission (Superluminescent) Diode,” *IEEE Journal of Quantum Electronics*, vol. 9, no. 8, pp. 820–828, 1973.

[2] N. S. Kwong, K. Y. Lau, N. Bar-Chaim, I. Ury, and K. J. Lee, “High power, high efficiency window buried heterostructure GaAlAs superluminescent diode with an integrated absorber,” *Applied Physics Letters*, vol. 51, no. 23, pp. 1879–1881, 1987.

[3] G. A. Alphonse, D. B. Gilbert, M. G. Harvey, and M. Ettenberg, “High-Power Superluminescent Diodes,” *IEEE Journal of Quantum Electronics*, vol. 24, no. 12, pp. 2454–2457, 1988.

[4] T. R. Chen, Y. H. Zhuang, Y. J. Xu, A. Yariv, and N. S. Kwong, “1.5 μm InGaAsP/InP buried crescent superluminescent diode on a p-InP substrate,” *Applied Physics Letters*, vol. 56, no. 25, pp. 2502–2503, 1990.

[5] B. D. Patterson, J. E. Epler, B. Graf, H. W. Lehmann, and H. C. Sigg, “A Superluminescent Diode at 1.3 μm with Very Low Spectral Modulation,” *IEEE Journal of Quantum Electronics*, vol. 30, no. 3, pp. 703–712, 1994.

[6] Y. Noguchi, H. Yasaka, O. Mikami, and H. Nagai, “High-power, broad-band InGaAsP superluminescent diode emitting at 1.5 μm,” *Journal of Applied Physics*, vol. 67, no. 5, pp. 2665–2667, 1990.

[7] C. F. Lin and C. L. Tang, “Generation of ultrashort pulses from a superluminescent diode with a monolithically integrated absorber in a coupled-cavity configuration,” *Applied Physics Letters*, vol. 63, no. 19, pp. 2594–2596, 1993.

[8] C. F. Lin and C. S. Juang, "Superluminescent diodes with bent waveguide," *IEEE Photonics Technology Letters*, vol. 8, no. 2, pp. 206–208, 1996.

[9] T. Yamatoya, S. Mori, F. Koyama, and K. Iga, "High Power GalnAsP/InP Strained Quantum Well Superluminescent Diode with Tapered Active Region," *Japanese Journal of Applied Physics, Part 1: Regular Papers and Short Notes and Review Papers*, vol. 38, no. 9 A, pp. 5121–5122, 1999.

[10] J. H. Song, S. H. Cho, I. K. Han, Y. Hu, P. J. Heim, F. G. Johnson, D. R. Stone, and M. Dagenais, "High-power broad-band superluminescent diode with low spectral modulation at 1.5-μm wavelength," *IEEE Photonics Technology Letters*, vol. 12, no. 7, pp. 783–785, 2000.

[11] H. S. Djie, C. E. Dimas, and B. S. Ooi, "Semiconductor quantum-dot based wideband emitter for optical sensors," in *Proceedings of IEEE Sensors*, vol. 2005, pp. 932–934, 2005.

[12] Z. Y. Zhang, R. A. Hogg, P. Jin, T. L. Choi, B. Xu, and Z. G. Wang, "High-Power quantum-dot superluminescent LED with broadband drive current insensitive emission spectra using a tapered active region," *IEEE Photonics Technology Letters*, vol. 20, no. 10, pp. 782–784, 2008.

[13] S. Chen, W. Li, Z. Zhang, D. Childs, K. Zhou, J. Orchard, K. Kennedy, M. Hugues, E. Clarke, I. Ross, O. Wada, and R. Hogg, "GaAs-Based Superluminescent Light-Emitting Diodes with 290-nm Emission Bandwidth by Using Hybrid Quantum Well/Quantum Dot Structures," *Nanoscale Research Letters*, vol. 10, no. 1, p. 340, 2015.

[14] Z. Z. Sun, D. Ding, Q. Gong, W. Zhou, B. Xu, and Z. G. Wang, "Quantum-dot superluminescent diode: A proposal for an ultra-wide output spectrum," *Optical and Quantum Electronics*, vol. 31, no. 12, pp. 1235–1246, 1999.

[15] N. Krstajić, L. E. Smith, S. J. Matcher, D. T. Childs, M. Bonesi, P. D. L. Greenwood, M. Hugues, K. Kennedy, M. Hopkinson, K. M. Groom, S. MacNeil, R. A. Hogg, and R. Smallwood, "Quantum dot superluminescent diodes for optical coherence tomography: Skin imaging," *IEEE Journal on Selected Topics in Quantum Electronics*, vol. 16, no. 4, pp. 748–754, 2010.

[16] Z. Y. Zhang, Q. Jiang, I. J. Luxmoore, and R. A. Hogg, “A p-type-doped quantum dot superluminescent LED with broadband and flat-topped emission spectra obtained by post-growth intermixing under a GaAs proximity cap,” *Nanotechnology*, vol. 20, no. 5, p. 055204, 2009.

[17] L. Occhi, R. Rezzonico, C. Vélez, M. van Uffelen, and F. Berghmans, “Effects of gamma radiation on superluminescent light emitting diodes (SLEDs) for fibre optic gyroscope applications,” p. 54, 2017.

[18] A. T. Aho, J. Viheriälä, H. Virtanen, N. Zia, R. Isoaho, and M. Guina, “High power GaInNAs superluminescent diodes emitting over 400 mW in the 1.2 μ m wavelength range,” *Applied Physics Letters*, vol. 115, no. 8, p. 081104, 2019.

[19] R. Yao, C.-S. Lee, V. Podolskiy, and W. Guo, “Single-transverse-mode broadband InAs quantum dot superluminescent light emitting diodes by parity-time symmetry,” *Optics Express*, vol. 26, no. 23, p. 30588, 2018.

[20] N. Ozaki, S. Yamauchi, Y. Hayashi, E. Watanabe, H. Ohsato, N. Ikeda, Y. Sugimoto, K. Furuki, Y. Oikawa, K. Miyaji, D. T. Childs, and R. A. Hogg, “Development of a broadband superluminescent diode based on self-assembled InAs quantum dots and demonstration of high-axial-resolution optical coherence tomography imaging,” *Journal of Physics D: Applied Physics*, vol. 52, no. 22, p. 225105, 2019.

[21] B. Jentzsch, A. Gomez-Iglesias, A. Tonkikh, H. Zull, S. Kugler, and B. Witzigmann, “Surface-Emitting Micro-Mirror Superluminescent Diodes: Investigation of Tilt Accuracy Via Far-Field Analysis,” *Physica Status Solidi (B) Basic Research*, vol. 256, no. 8, p. 1800494, 2019.

[22] H. P. Maruska and J. J. Tietjen, “The preparation and properties of vapor-deposited single-crystal-line GaN,” *Applied Physics Letters*, vol. 15, pp. 327–329, nov 1969.

[23] J. I. Pankove, E. A. Miller, D. Richman, and J. E. Berkeyheiser, “Electroluminescence in GaN,” *Journal of Luminescence*, vol. 4, pp. 63–66, jul 1971.

[24] J. I. Pankove, E. A. Miller, and J. E. Berkeyheiser, “GaN blue light-emitting diodes,” *Journal of Luminescence*, vol. 5, no. 1, pp. 84–86, 1972.

[25] H. P. Maruska, D. A. Stevenson, and J. I. Pankove, "Violet luminescence of Mg-doped GaN," *Applied Physics Letters*, vol. 22, no. 6, pp. 303–305, 1973.

[26] S. Yoshida, S. Misawa, and S. Gonda, "Improvements on the electrical and luminescent properties of reactive molecular beam epitaxially grown GaN films by using AlN-coated sapphire substrates," *Applied Physics Letters*, vol. 42, no. 5, pp. 427–429, 1983.

[27] H. Amano, N. Sawaki, I. Akasaki, and Y. Toyoda, "Metalorganic vapor phase epitaxial growth of a high quality GaN film using an AlN buffer layer," *Applied Physics Letters*, vol. 48, no. 5, pp. 353–355, 1986.

[28] S. Nakamura, T. Mukai, M. Senoh, and N. Iwasa, "Thermal annealing effects on P-type Mg-doped GaN films," *Japanese Journal of Applied Physics*, vol. 31, no. 2, pp. 139–142, 1992.

[29] S. Nakamura, M. Senoh, S. ichi Nagahama, N. Iwasa, T. Yamada, T. Matsushita, H. Kiyoku, and Y. Sugimoto, "InGaN-based multi-quantum-well-structure laser diodes," *Japanese Journal of Applied Physics, Part 2: Letters*, vol. 35, no. 1 B, p. L74, 1996.

[30] K. Motoki, "Development of gallium nitride substrates," *SEI Technical Review*, no. 70, pp. 28–35, 2010.

[31] H. Geng, H. Sunakawa, N. Sumi, K. Yamamoto, A. Atsushi Yamaguchi, and A. Usui, "Growth and strain characterization of high quality GaN crystal by HVPE," in *Journal of Crystal Growth*, vol. 350, pp. 44–49, 2012.

[32] K. Fujito, S. Kubo, and I. Fujimura, "Development of bulk GaN crystals and nonpolar/semipolar substrates by HVPE," *MRS Bulletin*, vol. 34, no. 5, pp. 313–317, 2009.

[33] H. König, M. Ali, W. Bergbauer, J. Brückner, G. Bruederl, C. Eichler, S. Gerhard, U. Heine, A. Lell, L. Nähle, M. Peter, J. Ristic, G. Rossbach, A. Somers, B. Stojetz, S. Tautz, J. Wagner, T. Wurm, U. Strauss, M. Baumann, A. Balck, and V. Krause, "Visible GaN laser diodes: from lowest thresholds to highest power levels," p. 11, 2019.

[34] E. Feltin, A. Castiglia, G. Cosendey, L. Sulmoni, J. F. Carlin, N. Grandjean, M. Rossetti, J. Dorsaz, V. Laino, M. Duelk, and C. Velez,

"Broadband blue superluminescent light-emitting diodes based on GaN," *Applied Physics Letters*, vol. 95, no. 8, p. 081107, 2009.

[35] M. T. Hardy, K. M. Kelchner, Y. D. Lin, P. S. Hsu, K. Fujito, H. Ohta, J. S. Speck, S. Nakamura, and S. P. DenBaars, "m-plane GaN-based blue superluminescent diodes fabricated using selective chemical wet etching," *Applied Physics Express*, vol. 2, no. 12, p. 121004, 2009.

[36] H. Ohno, K. Orita, M. Kawaguchi, K. Yamanaka, and S. Takigawa, "200mW GaN-based superluminescent diode with a novel waveguide structure," in *IEEE Photonic Society 24th Annual Meeting, PHO 2011*, pp. 505–506, 2011.

[37] A. Kafar, S. Stańczyk, S. Grzanka, R. Czernecki, M. Leszczyński, T. Suski, and P. Perlin, "Cavity suppression in nitride based superluminescent diodes," *Journal of Applied Physics*, vol. 111, no. 8, p. 083106, 2012.

[38] F. Kopp, T. Lermer, C. Eichler, and U. Strauss, "Cyan superluminescent light-emitting diode based on InGaN quantum wells," *Applied Physics Express*, vol. 5, no. 8, p. 082105, 2012.

[39] C. Shen, T. K. Ng, J. T. Leonard, A. Pourhashemi, S. Nakamura, S. P. DenBaars, J. S. Speck, A. Y. Alyamani, M. M. El-desouki, and B. S. Ooi, "High-brightness semipolar (2021¯) blue InGaN/GaN superluminescent diodes for droop-free solid-state lighting and visible-light communications," *Optics Letters*, vol. 41, no. 11, p. 2608, 2016.

[40] M. Rossetti, J. Napierala, N. Matuschek, U. Achatz, M. Duelk, C. Vélez, A. Castiglia, N. Grandjean, J. Dorsaz, and E. Feltin, "Superluminescent light emitting diodes: the best out of two worlds," in *MOEMS and Miniaturized Systems XI*, vol. 8252, p. 825208, 2012.

[41] F. Kopp, C. Eichler, A. Lell, S. Tautz, J. Ristić, B. Stojetz, C. Hö, T. Weig, U. T. Schwarz, and U. Strauss, "Blue superluminescent light-emitting diodes with output power above 100mW for picoprojection," *Japanese Journal of Applied Physics*, vol. 52, no. 8 PART 2, p. 08JH07, 2013.

[42] E. F. Schubert and J. K. Kim, "Solid-state light sources getting smart," 2005.

[43] B. S. Ooi, "Visible laser and superluminescent diode based free space and underwater communications," in *2016 IEEE Photonics Conference, IPC 2016*, pp. 811–812, 2017.

[44] G. R. Goldberg, A. Boldin, S. M. Andersson, P. Ivanov, N. Ozaki, R. J. Taylor, D. T. Childs, K. M. Groom, K. L. Kennedy, and R. A. Hogg, "Gallium Nitride Superluminescent Light Emitting Diodes for Optical Coherence Tomography Applications," *IEEE Journal of Selected Topics in Quantum Electronics*, vol. 23, no. 6, pp. 1–11, 2017.

[45] C. De Santi, M. Meneghini, M. La Grassa, N. Trivellin, B. Galler, R. Zeisel, B. Hahn, M. Goano, S. Dominici, M. Mandurrino, F. Bertazzi, G. Meneghesso, and E. Zanoni, "Thermal droop in InGaN-based LEDs: physical origin and dependence on material properties," in *Light-Emitting Diodes: Materials, Devices, and Applications for Solid State Lighting XX*, vol. 9768, p. 97680D, 2016.

[46] A. A. Alatawi, J. A. Holguin-Lerma, C. H. Kang, C. Shen, R. C. Subedi, A. M. Albadri, A. Y. Alyamani, T. K. Ng, and B. S. Ooi, "High-power blue superluminescent diode for high CRI lighting and high-speed visible light communication," *Optics Express*, vol. 26, no. 20, p. 26355, 2018.

[47] A. A. Alatawi, J. A. Holguin-Lerma, C. Shen, M. K. Shakfa, A. A. Alhamoud, A. M. Albadri, A. Y. Alyamani, T. K. Ng, and B. S. Ooi, "High Power GaN-Based Blue Superluminescent Diode Exceeding 450 mW," in *Conference Digest - IEEE International Semiconductor Laser Conference*, vol. 2018-Septe, pp. 129–130, 2018.

[48] A. A. Alatawi, J. A. Holguin-Lerma, C. H. Kang, C. Shen, A. M. Albadri, A. Y. Alyamani, T. K. Ng, and B. S. Ooi, "Blue superluminescent diode on c-plane gan beyond gigahertz modulation bandwidth for visible light communication," in *2019 Conference on Lasers and Electro-Optics Europe and European Quantum Electronics Conference, CLEO/Europe-EQEC 2019*, 2019.

[49] N. Primerov, J. Dahdah, S. Gloor, T. von Niederhäusern, N. Matuschek, A. Castiglia, M. Malinverni, C. Mounir, M. Rossetti, M. Duelk, and C. Vélez, "A compact red-green-blue superluminescent diode module: A novel light source for AR microdisplays," p. 13, 2019.

[50] H. Zhang, C.-W. Shih, D. Martin, A. Caut, J.-F. Carlin, R. Butté, and

N. Grandjean, "Broadened Bandwidth Amplified Spontaneous Emission from Blue GaN-Based Short-Cavity Superluminescent Light-Emitting Diodes," *ECS Journal of Solid State Science and Technology*, vol. 9, no. 1, p. 015019, 2020.

[51] G. R. Goldberg, D. H. Kim, R. J. Taylor, D. T. Childs, P. Ivanov, N. Ozaki, K. L. Kennedy, K. M. Groom, Y. Harada, and R. A. Hogg, "Bandwidth enhancement in an InGaN/GaN three-section superluminescent diode for optical coherence tomography," *Applied Physics Letters*, vol. 117, p. 61106, aug 2020.

[52] R. Cahill, P. P. Maaskant, M. Akhter, and B. Corbett, "High power surface emitting InGaN superluminescent light-emitting diodes," *Applied Physics Letters*, vol. 115, no. 17, p. 171102, 2019.

[53] E. Feltin, A. Castiglia, G. Cosendey, L. Sulmoni, J. F. Carlin, N. Grandjean, M. Rossetti, J. Dorsaz, V. Laino, M. Duelk, and C. Velez, "Broadband blue superluminescent light-emitting diodes based on GaN," *Applied Physics Letters*, vol. 95, no. 8, p. 081107, 2009.

[54] B. Jentzsch, A. Gomez-Iglesias, A. Tonkikh, and B. Witzigmann, "Surface-emitting superluminescent diode arrays," in *2019 Conference on Lasers and Electro-Optics Europe and European Quantum Electronics Conference, CLEO/Europe-EQEC 2019*, 2019.

[55] A. A. Alatawi, J. A. Holguin-Lerma, C. H. Kang, C. Shen, I. Dursun, L. Sinatra, A. M. Albadri, A. Y. Alyamani, T. K. Ng, O. M. Bakr, and B. S. Ooi, "Blue Superluminescent Diodes with GHz Bandwidth Exciting Perovskite Nanocrystals for High CRI White Lighting and High-Speed VLC," in *2019 Conference on Lasers and Electro-Optics, CLEO 2019 - Proceedings*, 2019.

[56] EXALOS, "EXALOS SLED Modules," dec 2020.

[57] V. F. Mymrin, K. A. Bulashevich, N. I. Podolskaya, I. A. Zhmakin, S. Y. Karpov, and Y. N. Makarov, "Modelling study of MQW LED operation," in *Physica Status Solidi C: Conferences*, vol. 2, pp. 2928–2931, 2005.

[58] J. J. Huang, H. C. Kuo, and S. C. Shen, *Nitride Semiconductor Light-Emitting Diodes (LEDs): Materials, Technologies, and Applications: Second Edition*. 2017.

[59] T. A. Welton, “Some observable effects of the quantum-mechanical fluctuations of the electromagnetic field,” *Physical Review*, vol. 74, no. 9, pp. 1157–1167, 1948.

[60] J. S. Im, A. Moritz, F. Steuber, V. Härle, F. Scholz, and A. Hangleiter, “Radiative carrier lifetime, momentum matrix element, and hole effective mass in GaN,” *Applied Physics Letters*, vol. 70, no. 5, pp. 631–633, 1997.

[61] D. J. Griffiths and D. F. Schroeter, *Introduction to Quantum Mechanics*. 2018.

[62] J. Piprek, “Energy Efficiency Analysis of GaN-Based Blue Light Emitters,” *ECS Journal of Solid State Science and Technology*, vol. 9, no. 1, p. 015008, 2020.

[63] N. F. Gardner, G. O. Müller, Y. C. Shen, G. Chen, S. Watanabe, W. Götz, and M. R. Krames, “Blue-emitting InGaN-GaN double-heterostructure light-emitting diodes reaching maximum quantum efficiency above 200 A cm2,” *Applied Physics Letters*, vol. 91, no. 24, p. 243506, 2007.

[64] J. Iveland, L. Martinelli, J. Peretti, J. S. Speck, and C. Weisbuch, “Direct measurement of auger electrons emitted from a semiconductor light-emitting diode under electrical injection: Identification of the dominant mechanism for efficiency droop,” *Physical Review Letters*, vol. 110, no. 17, p. 177406, 2013.

[65] T. Sadi, P. Kivisaari, J. Oksanen, and J. Tulkki, “On the correlation of the Auger generated hot electron emission and efficiency droop in III-N light-emitting diodes,” *Applied Physics Letters*, vol. 105, no. 9, p. 091106, 2014.

[66] J. Piprek, *Nitride Semiconductor Devices: Principles and Simulation*. 2007.

[67] J. Piprek, “What limits the efficiency of GaN-based superluminescent light-emitting diodes (SLEDs)?,” *Optical and Quantum Electronics*, vol. 51, no. 12, pp. 1–9, 2019.

[68] Y. Deng and D. Chu, “Coherence properties of different light sources and their effect on the image sharpness and speckle of holographic displays,” *Scientific Reports*, vol. 7, no. 1, pp. 1–2, 2017.

[69] C. Akcay, P. Parrein, and J. P. Rolland, "Estimation of longitudinal resolution in optical coherence imaging," *Applied Optics*, vol. 41, no. 25, p. 5256, 2002.

[70] B. Frieden, "Laser speckle and related phenomena," *IEEE Journal of Quantum Electronics*, vol. 20, no. 12, pp. 1533–1533, 2004.

[71] V. Shidlovski, "Superluminescent Diodes. Short overview of device operation principles and performance parameters," *SuperlumDiodes Ltd.*, pp. 1–9, 2004.

[72] Y. Zhao, W. Han, J. Song, X. Li, Y. Liu, D. Gao, G. Du, H. Cao, and R. P. Chang, "Spontaneous emission factor for semiconductor superluminescent diodes," *Journal of Applied Physics*, vol. 85, no. 8 I, pp. 3945–3948, 1999.

[73] P. Brosson, "Analytical Model of a Semiconductor Optical Amplifier," *Journal of Lightwave Technology*, vol. 12, no. 1, pp. 49–54, 1994.

[74] W. Fang and S. L. Chuang, "Theoretical prediction of GaN lasing and temperature sensitivity," *Applied Physics Letters*, vol. 67, p. 751, 1995.

[75] S. Kamiyama, K. Ohnaka, M. Suzuki, and T. Uenoyama, "Optical gain calculation of wurtzite gan/algan quantum well laser," *Japanese Journal of Applied Physics*, vol. 34, no. 7, pp. L821–L823, 1995.

[76] T. Swietlik, G. Franssen, R. Czernecki, M. Leszczynski, C. Skierbiszewski, I. Grzegory, T. Suski, P. Perlin, C. Lauterbach, and U. T. Schwarz, "Mode dynamics of high power (InAl) GaN based laser diodes grown on bulk GaN substrate," in *Journal of Applied Physics*, vol. 101, p. 083109, 2007.

[77] J. Jeschke, U. Zeimer, L. Redaelli, S. Einfeldt, M. Kneissl, and M. Weyers, "Effect of quantum well non-uniformities on lasing threshold, linewidth, and lateral near field filamentation in violet (Al,In)GaN laser diodes," *Applied Physics Letters*, vol. 105, no. 17, p. 173501, 2014.

[78] D. W. Kim, J. C. Bae, W. J. Kim, H. K. Baik, J. M. Myoung, and S. M. Lee, "The improvement of electrical properties of Pd-based contact to p-GaN by surface treatment," *Journal of Electronic Materials*, vol. 30, no. 3, pp. 183–187, 2001.

[79] V. S. Nirwal, K. R. Peta, V. R. Reddy, and M. D. Kim, "Influence of rapid thermal annealing on electrical and structural properties of Pd/Au Schottky contact to Ga-polarity GaN grown on Si (111) substrate," *Journal of Alloys and Compounds*, vol. 705, pp. 782–787, 2017.

[80] M. Norman-Reiner, E. Freier, A. Mogilatenko, I. Ostermay, V. Hoffmann, R. Szukiewicz, O. Krüger, D. Hommel, S. Einfeldt, M. Weyers, and G. Tränkle, "Structural and electrical properties of Pd/p-GaN contacts for GaN-based laser diodes," *Journal of Vacuum Science & Technology B*, vol. 38, no. 3, p. 032211, 2020.

[81] J. O. Song, J. S. Ha, and T. Y. Seong, "Ohmic-contact technology for GaN-based light-emitting diodes: Role of p-type contact," *IEEE Transactions on Electron Devices*, vol. 57, no. 1, pp. 42–59, 2010.

[82] D. K. Schroder and L. G. Rubin, *Semiconductor Material and Device Characterization* , vol. 44. John Wiley & Sons, 1991.

[83] J. H. Klootwijk and C. E. Timmering, "Merits and limitations of circular TLM structures for contact resistance determination for novel III-V HBTs," in *IEEE International Conference on Microelectronic Test Structures*, pp. 247–252, 2004.

[84] L. L. Smith, S. W. King, R. J. Nemanich, and R. F. Davis, "Cleaning of GaN surfaces," *Journal of Electronic Materials*, vol. 25, no. 5, pp. 805–810, 1996.

[85] M. Diale, F. D. Auret, N. G. Van Der Berg, R. Q. Odendaal, and W. D. Roos, "Analysis of GaN cleaning procedures," *Applied Surface Science*, vol. 246, no. 1-3, pp. 279–289, 2005.

[86] L. Lewis, B. Corbett, D. O Mahony, and P. P. Maaskant, "Low-resistance Ni-based Schottky diodes on freestanding n-GaN," *Applied Physics Letters*, vol. 91, no. 16, p. 162103, 2007.

[87] M. Diale, F. D. Auret, N. G. Van Der Berg, R. Q. Odendaal, and W. D. Roos, "Analysis of GaN cleaning procedures," *Applied Surface Science*, vol. 246, no. 1-3, pp. 279–289, 2005.

[88] C. C. Kim, J. H. Je, D. W. Kim, H. K. Baik, S. M. Lee, and P. Ruterana, "Annealing behavior of Pd/GaN (0001) microstructure," *Materials Science and Engineering B: Solid-State Materials for Advanced Technology*, vol. 82, no. 1-3, pp. 105–107, 2001.

[89] Y. Bai, J. Liu, H. J. Shen, P. Ma, X. Y. Liu, and L. W. Guo, "Effect of annealing on the characteristics of Pd/Au contacts to p-type GaN/Al0.45Ga0.55N," *Journal of Electronic Materials*, vol. 41, no. 11, pp. 3021–3026, 2012.

[90] J. Piprek, H. Wenzel, and M. Kneissl, "Analysis of wavelength-dependent performance variations of GaN-based ultraviolet lasers," in *Optoelectronic Devices: Physics, Fabrication, and Application IV*, vol. 6766, p. 67660H, 2007.

[91] T. S. Chow, "Wetting of rough surfaces," *Journal of Physics Condensed Matter*, vol. 10, no. 27, p. L445, 1998.

[92] K. A. Brakke, "The surface evolver," *Experimental Mathematics*, vol. 1, no. 2, pp. 141–165, 1992.

[93] R. Kirchner, A. Schleunitz, and H. Schift, "Energy-based thermal reflow simulation for 3D polymer shape prediction using Surface Evolver," *Journal of Micromechanics and Microengineering*, vol. 24, no. 5, p. 055010, 2014.

[94] M. Emmer and K. A. Brakke, "Surface EvolverComputing Soap Films and Crystals," 1992.

[95] C. E. Dreyer, A. Janotti, and C. G. Van De Walle, "Absolute surface energies of polar and nonpolar planes of GaN," *Physical Review B - Condensed Matter and Materials Physics*, vol. 89, no. 8, p. 081305, 2014.

[96] C. Messmer and J. C. Bilello, "The surface energy of Si, GaAs, and GaP," *Journal of Applied Physics*, vol. 52, no. 7, pp. 4623–4629, 1981.

[97] A. Shivamurthy, P. S, P. G. R, R. N. M, and S. R. J, "Study of surface energy of SiO2 and TiO2 on charge carrier mobility of rubrene organic field effect transistor," in *Proceedings of the 3rd International Conference on Theoretical and Applied Nanoscience and Nanotechnology (TANN'19)*, 2019.

[98] J. Bauer, "Surface tension, adhesion and wetting of materials for photolithographic process," *Journal of Vacuum Science & Technology B: Microelectronics and Nanometer Structures*, vol. 14, no. 4, p. 2485, 1996.

[99] A. Tanide, S. Nakamura, A. Horikoshi, S. Takatsuji, M. Kohno, K. Kinose, S. Nadahara, K. Ishikawa, M. Sekine, and M. Hori, " Effects

of BCl 3 addition to Cl 2 gas on etching characteristics of GaN at high temperature ," *Journal of Vacuum Science & Technology B*, vol. 37, no. 2, p. 021209, 2019.

[100] Y. P. Varshni, "Temperature dependence of the energy gap in semiconductors," *Physica*, vol. 34, no. 1, pp. 149–154, 1967.

[101] M. X. Feng, Q. Sun, J. P. Liu, Z. C. Li, Y. Zhou, H. W. Gao, S. M. Zhang, and H. Yang, "A study of efficiency droop phenomenon in GaN-based laser diodes before lasing," *Materials*, vol. 10, no. 5, p. 482, 2017.

[102] E. F. Schubert, "Junction and carrier temperatures," in *Light-Emitting Diodes*, pp. 101–112, Cambridge: Cambridge University Press, 2010.

[103] J. Piprek, J. Kenton White, and A. J. SpringThorpe, "What limits the maximum output power of long-wavelength AlGaInAs/InP laser diodes?," *IEEE Journal of Quantum Electronics*, vol. 38, no. 9, pp. 1253–1259, 2002.

[104] N. Laurand, B. Guilhabert, J. McKendry, A. E. Kelly, B. Rae, D. Massoubre, Z. Gong, E. Gu, R. Henderson, and M. D. Dawson, "Colloidal quantum dot nanocomposites for visible wavelength conversion of modulated optical signals," *Optical Materials Express*, vol. 2, no. 3, p. 250, 2012.

[105] B. G. Kumar, S. Sadeghi, R. Melikov, M. M. Aria, H. B. Jalali, C. W. Ow-Yang, and S. Nizamoglu, "Structural control of InP/ZnS core/shell quantum dots enables high-quality white LEDs," *Nanotechnology*, vol. 29, no. 34, p. 345605, 2018.

[106] L. W. Chi, K. T. Lam, Y. K. Kao, F.-S. Juang, Y. S. Tasi, Y.-K. Su, S.-J. Chang, C. C. Chen, and J. K. Sheu, "<title>Ohmic contacts to GaN with rapid thermal annealing</title>," in *Light-Emitting Diodes: Research, Manufacturing, and Applications IV*, vol. 3938, pp. 224–233, 2000.

[107] M. Martens, C. Kuhn, E. Ziffer, T. Simoneit, V. Kueller, A. Knauer, J. Rass, T. Wernicke, S. Einfeldt, M. Weyers, and M. Kneissl, "Low absorption loss p-AlGaN superlattice cladding layer for current-injection deep ultraviolet laser diodes," *Applied Physics Letters*, vol. 108, no. 15, p. 151108, 2016.

[108] C. Y. Huang, Y. D. Lin, A. Tyagi, A. Chakraborty, H. Ohta, J. S. Speck, S. P. Denbaars, and S. Nakamura, "Optical waveguide simulations for

the optimization of InGaN-based green laser diodes," *Journal of Applied Physics*, vol. 107, no. 2, p. 023101, 2010.

[109] M. X. Feng, J. P. Liu, S. M. Zhang, D. S. Jiang, Z. C. Li, K. Zhou, D. Y. Li, L. Q. Zhang, F. Wang, H. Wang, P. Chen, Z. S. Liu, D. G. Zhao, Q. Sun, and H. Yang, "High efficient GaN-based laser diodes with tunnel junction," *Applied Physics Letters*, vol. 103, no. 4, p. 043508, 2013.

[110] W. S. Heaps, "Broadband lidar technique for precision CO," pp. 711102–711102–9, 2008.

[111] B. Redding, P. Ahmadi, and C. A. Hui, "An alternative to LEDs for full-field imaging," *Photonics Spectra*, vol. 50, no. 5, pp. 46–49, 2016.

Appendix A

MATLAB script for SLED simulation

```
N0=1.5*10^18; %equal to tau/q*d, reduced by a factor of 10^8 to
   allow for computations
Ntr= 7*10^18; %transparency carrier density
gam = (1-(1/(1+(3*w/1.4)^2.25)));%optical confinement factor
R1=0.0001;%front facet reflectivity
R2=0.0001;%back facet reflectivity
neff = 2.4; %refractive index
a = 1.5*10^(-16); %gain coefficient, increased by a factor of 10^8
   to compensate for reduction in carrier density
p = 1.125*10^(-16); %normalising factor equal to c*a*tau
dL = 0.000001; %segment length
L = 1000; %device length in microns
b = 2500; %loss
B = 10^(-11); %bimolecular recombination coefficient
beta = 0.01; %spontaneous emission coupling factor
c = 3*10^8;%speed of light
pow = 4.2*10^(-15); %converts photon density to power in Watts

    kcount=0;

    N=ones(1,L)*N0;
    S=zeros(1,L);
    S_sat = 0.015;
```

```
for q = 1:1:50 %this loop sweeps the current density from 1 to 50
    kcount=q; %kcount sets the current density in A cm^-2
    G(1)=a*N0/L; %initalises gain array
    Pout(1)=0; %initialises output power array
    diff = 1;%initialise tolerence for convergence loop
    i=2; %initialise counts for convergence loop
while diff>0.01 && i<1000 %this convergence loop gets the steady
   state photon and carrier densities and average gain
    Car(1) = N0;

for j=1:L
                N(j)=(N0*(kcount/(1+kcount/30))/(1+((p*S(j)))));%
                   carrier density distribution
                G(kcount)=gam*a*mean(N);%average modal gain
                S(j)= ((beta*B*(N(j)^2))/(G(kcount)))*(exp((G(
                   kcount)-b)*j*dL)+exp((G(kcount)-b)*(L-j)*dL))/c;
                   %photon density distriubtion
                Car(i) = mean(N); %initialises average carrier
                   density
                diff = (abs(1-(Car(i)/Car(i-1))));%assigns new
                   value to difference between carrier density in
                   last loop and latest loop
                i = i+1;%increments i for next loop
end
end
% G(kcount+1)=100*(D+(C-D)/(1+((sum(N)/L)/(x0*L/1000)))^p);
Gsp(q)=exp((G(q)-b)*L*dL);
Pmax(q)=(((kcount/(1+((kcount)/30)))/(G(q)-b)))*(Gsp(q)-1)*((1-R1)
   *(R2*Gsp(q)+1)/(1+(R1*R2*Gsp(q))^2-2*R1*R2*Gsp(q)));
Pmin(q)=(((kcount/(1+((kcount)/30)))/(G(q)-b)))*(Gsp(q)-1)*((1-R1)
   *(R2*Gsp(q)+1)/(1+(R1*R2*Gsp(q))^2));
Dmod(q)= 1-Pmin(q)/Pmax(q);
G(kcount+1)=a*mean(N)/(1+(mean(S)/S_sat));
Pout(kcount)=pow*S(L);

end
```